December 2020

Lattice and Charge Order in Layered Bi-Based Topological Insulators

Yanan Li
University of Wisconsin-Milwaukee

LATTICE AND CHARGE ORDER IN LAYERED BI-BASED TOPOLOGICAL INSULATORS

by

Yanan Li

A Dissertation Submitted in
Partial Fulfillment of the
Requirements for the Degree of

Doctor of Philosophy

in Physics

at

The University of Wisconsin-Milwaukee

December 2020

ABSTRACT

LATTICE AND CHARGE ORDER IN LAYERED BI-BASED TOPOLOGICAL INSULATORS

by

Yanan Li

The University of Wisconsin-Milwaukee, 2020
Under the Supervision of Professor Prasenjit Guptasarma

Bi_2X_3 (X=Se/Te) is a topological insulator, as well as a layered dichalcogenide. The topological properties of Bi_2Se_3 have gained a lot of interest over the past decade. However, as a layered chalcogenide, much of its uniqueness has not been fully discovered, e.g. hosting Charge Density Wave as reported in most other chalcogenides. With intercalation of Nb, Cu and Sr, Bi_2Se_3 becomes an unconventional superconductor. Together with its topological properties, A-Bi_2X_3 (A=Nb, Cu and Sr) have been proposed to be potential Topological superconductors. However, the mechanism of the unconventional SC in these compounds is still under discussion.

For my PhD research, I discovered charge density wave (CDW) order in self-doped Bi_2Se_3 and metal intercalated Bi_2X_3 together with superconducting transitions. Together with collaborators, I identified these phase transitions through studying and analyzing their crystal structures, electronic structures, and local nuclear environment. I further found that certain growth conditions (annealing and quenching temperatures) can help maintain the intercalation/defect phase and play as an important factor for observations of the intertwined electronic ground states. With intercalation or self-doped defects, the layered nature of Bi_2X_3 can easily be driven with a periodic lattice distortion. This lattice disorder can further lead to a local charge density distortion, with

concomitant changes in the electronic structure. Depending on the relationship between the periodicity of the charge density and the underlying lattice constant, it can lead to I-CDW or CDW. In Cu doped Bi_2Te_2Se, I studied lattice and charge order due to different concentration of Cu into Bi_2Te_2Se. In self-doped Bi_2Se_3, I found CDW order with energy gap of 10meV. With Nb doped Bi_2Se_3, both superconductivity (SC) and CDW were found in this material. Both SC and CDW are broken symmetries at the ground state. The underlying relationship between these two states has long been under debate. Based on recent reports and my experimental observations, the fermiology seems play an important role for the electronic properties in A-Bi_2X_3. It is possible in doped Bi_2X_3 that both SC and CDW originate from the intercalation effect where the change of lattice structure symmetry leads to electronic symmetry broken. This work examines how lattice order leads to charge order in doped Bi_2X_3. It also discusses possible origins for the underlying electronic intertwined states and how they are all related to each other.

I dedicate this thesis to my mother.

Her love, support and understanding encourage me to achieve my dreams.

TABLE OF CONTENTS

LIST OF FIGURES

LIST OF TABLES

LIST OF ABBREVIATIONS

CDW	Charge Density Wave
I-CDW	Incommensurate Charge Density Wave
PLD	Periodic Lattice Distortion
SC	Superconductivity
TI	Topological Insulator
NMR	Nuclear Magnetic Resonance
RF	Resonance Frequency
FID	Free Induction Decay
TEM	Transmission Electron Microscopy
HRTEM	High Resolution Transmission Electron Microscopy
SAED	Selected Area Electron Diffraction
XPS	X-ray Photoelectron Spectroscopy

ACKNOWLEDGEMENTS

There are many people who helped me along the long way of this journey. I want to thank you all for the help: my advisor, my graduation committee, mentors, collaborators, lab mates, my friends, and my family.

First and foremost, I want to thank my advisor Dr. Prasenjit Guptasarma in guiding me into research and helping me in finding the joy of exploring material science. His open mindedness about new ideas gave me opportunities to explore new projects, which helped me to become an independent researcher. He trained me to think critically to interpret the outcomes of my research and encouraged me to think from outside of the box. I am grateful to him for his mentorship that made me grow as a scientist and become stronger as a person.

From the bottom of my heart, I want to thank my committee members (Dr. Paul Lyman, Dr. Michael Weinert, Dr. Daniel Agterberg and Dr. Carol Hirschmugl). Dr. Paul Lyman provided me with great guidance for my prelim exam preparation and led me to think critically about my experimental results. I thank him for being a great teacher and a friend. Dr. Michael Weinert is a life-long teacher to me; his wise research suggestions led me to think more as a scientist and to work with a kind attitude. Dr. Daniel Agterberg is also so knowledgeable and humble, and it has always been so enjoyable to discuss my research results with him and to hear his valuable suggestions. Dr. Carol Hirschmugl is a great role model to me, as a successful female scientist; her wide experiences and interests in research opened my eyes in seeing the various possibilities in science.

I want to give my special thank you to my research mentors. I am deeply grateful to Dr. Arneil Reyes at the National High Magnetic Field Laboratory for providing me opportunities to

come to his lab to do research on NMR. It was a great research experience and one of my most valuable memories. Dr. Arneil Reyes is a knowledgeable mentor and a great friend. I thank him in training me in NMR from scratch and guiding me throughout my projects. His humility and kindness created a model for me, to become a scientist just like him working towards discovering new science and pursuing a career path for benefiting more people. I also want to thank another great mentor for my growth as a scientist, Dr. Marvin Schofield. I am thankful for his patience and thoughtfulness in training me in TEM techniques and for his suggestions during my paper writing. Thank you to Dr. Nathaniel Smith in training me in crystal growth and for his suggestions in my project, thanks to Dr. Steven Hardcastle for his kind suggestions and help with Raman and X-ray measurements. Thank you to Dr. Ryan Baumbach for his great suggestions in my experimental measurements. Also, many thanks to my lab mates and other collaborators, Christian, Bill, Anand, Sanath and Lucas for contributing to my projects and making this research possible.

Last but not the least, I want to thank my dear friends and family! I want to thank my dear friend, Jonathan Holm. He supported me all the way during my dissertation writing. Thank you for his kind help in proofreading my dissertation from chapter 1 to the end of my dissertation. Thank you to Sanath, for helping me in finding housing when I came to MagLab and for giving me countless rides while I was there. Most importantly, I want to thank my family: my parents, my grandma and grandpa, and especially my mom, for always believing in me and for providing me with endless support, love, and encouragement. Her love and kindness encourage me to get through every step on the way of pursuing my dreams.

Chapter 1: Introduction

1.1 Charge Density Wave (CDW)

A Charge Density Wave (CDW) is a type of broken symmetry at the electronic ground state for most metals. For one-dimensional CDW, it is usually accompanied by a Periodic Lattice Distortion (PLD) and opening of an energy gap. The leading factors for CDW usually are Fermi Nesting and strong electron-phonon interaction. In the formation of a CDW, the electronic energy of the solid is lowered due the lattice distortion with which the associated strain energy is less than the electronic energy reduction [1-5]. In some unconventional cases, the CDW can also be introduced by electron-electron correlation, such as in the heavy fermion based unconventional superconductors [6, 7]. The theory for CDW was first established by Peierls in 1955 from one-dimensional conductors [8], while the experimental observation was found in 1973 by using X-ray diffuse scattering on 1D $K_2Pt(CN)_4Br_{0.3}\cdot 3H_2O$ [9]. There are other kinds of electronic symmetry broken at the ground state, such as superconductivity. Since superconductivity can also be introduced by electron-phonon interaction, the coexistence and competition of CDW and superconductivity remains of extreme interest until the present time [10-15].

1.1.1 The Peierls Theory

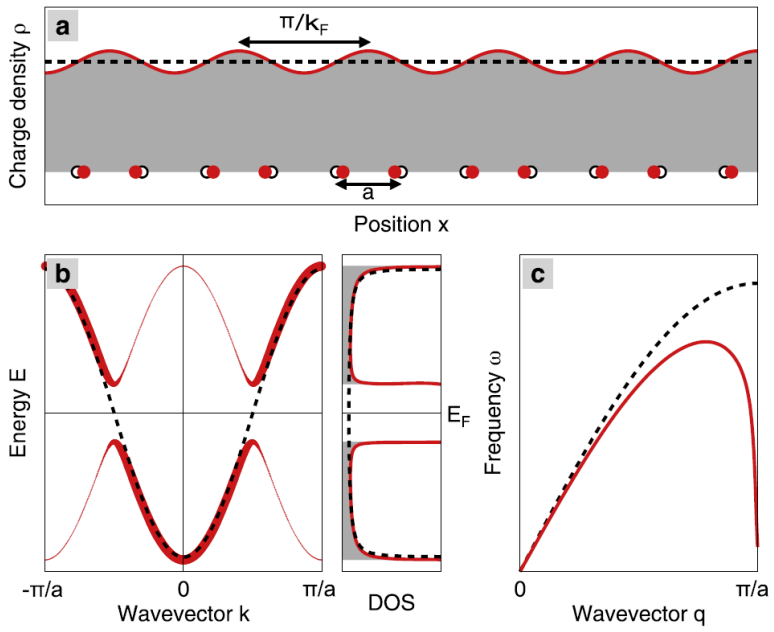

Figure 1.1 Peierls distortion of a 1D metal with a half-filled band. (a) Peierls distortion on a 1D atoms chain. (b) Electronic band dispersion and energy dependence of the density of states near Fermi level. (c) Acoustic phonon dispersion (Adapted from Ref. [4])

Let us start with the 1D case of CDW, as explained by Peierls theory [1-4, 8-9]: supposing a one-dimensional linear atoms chain has a distance of "a" between two neighboring atoms. If there is no perturbation (such as electron-electron and electron-phonon interactions), at the base temperature, its electronic density is ρ_0. As temperature is increased, a perturbation may be introduced due to the interaction of electron and lattice and lead to a modulation of local electron density $\rho(r)$:

$$\rho(r) = \rho_0 + \rho_1 cos(q \cdot r + \varphi), \quad (1.1)$$

where, ρ_1 is the amplitude of the modulation, q is the wave vector and φ is the phase of charge density wave [1, 2]. With the new periodicity of the wavelength, the ions in the 1D metal will also

see a different potential and then move to new equilibrium positions [4]. As a result, a Periodic Lattice Distortion (PLD) will be generated as follows:

$$u_n = u_0 \sin(n|\mathbf{q}_0|a + \varphi), \quad (1.2)$$

where the integer n defines the position of the ions, q_0 is the wavevector and u_0 is the amplitude which is generally smaller compared to the lattice constant a [2, 4]. Once the electrons placed by this new potential, the electron density modulation will also be created by the equation (1.1). Thus, the PLD and CDW usually come together. Accompanied with this distortion, an energy gap will open near the Fermi level, as shown in Figure 1. In the 1D metal case, the amplitude of the energy gap is proportional to the amplitude of periodic lattice distortion u [2, 4]. With the development of an energy gap, the energy of the occupied electron states will be lowered and the energy of the empty states will be raised. When the net electronic state of energy gain overcoming the Coulomb and elastic energy cost, the CDW/PLD will take place [4].

In the case of time-independent potential, the introduced charge modulation can also be written as [1, 2]:

$$\rho^{ind}(q)=X(q)\Phi_{tot}(q), \quad (1.3)$$

where, X(q) is the Lindhard response function and $\Phi_{tot}(r)$ is the time-independent potential. The Lindhard response function represents the degenerate Fermi surface [1, 2, 4]:

$$X(q)=\int \frac{dk}{(2\pi)^d}\frac{f_k-f_{k+q}}{E_k-E_{k+q}}, \quad (1.4)$$

f_k is the Fermi-Dirac function and E_k is the energy near the Fermi surface. Thus, materials with highly anisotropic band structures typically form CDW [2].

A Peierls transition can be considered as a metal to insulator transition for low dimensional materials, and it is driven by strong electron-phonon interactions which cause the energy instability near the Fermi level and lead to the formation of an energy gap. The transition temperature is defined as T_P or T_{CDW} (for my measurement results all CDW transitions were assigned as T_{CDW}), where at temperature above T_{CDW} the material behaves like a metal, while below T_{CDW} behaves like a semiconductor [1]. This Peierls transition can be described by a mean-field theory of a 1D electron-phonon Frohlich Hamiltonian as [1-3]:

$$\mathcal{H}_{tot} = \mathcal{H}_{el} + \mathcal{H}_{ph} + \mathcal{H}_{el-ph} = \sum_k \epsilon_k a_k^+ a_k + \sum_q \hbar\omega_q b_q^+ b_q + \sum_{k,q} g_q a_{k+q}^+ a_k (b_{-q}^+ + b_q), \quad (1.5)$$

$$\mathcal{H}_{el} = \sum_k \epsilon_k a_k^+ a_k,$$

$$\mathcal{H}_{ph} = \sum_q \hbar\omega_q b_q^+ b_q,$$

$$\mathcal{H}_{el-ph} = \sum_{k,q} g_q a_{k+q}^+ a_k (b_{-q}^+ + b_q);\ g_q = i\left(\frac{\hbar}{2M\omega_q}\right)^{1/2} |q| V_q,$$

where $\mathcal{H}_{el}$, $\mathcal{H}_{ph}$ and $\mathcal{H}_{el-ph}$ are the Hamiltonians for free electron gas, lattice vibration and electron-phonon interactions a_k^+ and a_k are the creation and annihilation operators for the electron states with energy $\epsilon_k = \hbar^2 k^2/2m$; b_q^+ and b_q are the creation and annihilation operators for the phonons with wavevector q, normal mode frequency; ω_q; g_q is the electron-phonon coupling constant, with M representing ionic mass, and V_q is the potential at q.

In the 1D case, the coupled electron-phonon system is unstable, where. The linear dispersion relationship near electron band ϵ_F can be described as $\epsilon_k = \hbar v_F(|k| - k_F), with\ v_F\ and\ k_F$ the Fermi velocity and Fermi vector [1-2]. This instability of energy near ϵ_F can lead to fundamental consequences for both lattice and electronic states [1]:

1.1.1.1 The effect on Lattice vibration

With electron-phonon interaction, the equation of motion for a small amplitude displacement can be described as such [1]:

$$\ddot{Q}_q = -\omega_q^2 Q_q - g\left(\frac{2\omega_q}{M\hbar}\right)^{1/2}\rho_q, \quad (1.6)$$

in which g is assumed independent of q, Q_q is a normal coordinate, and ρ_q is the q^{th} component of the electronic density, with $\rho_q = \sum_k a_{k+q}^{+} a_k$. The introduced ionic potential is proportional to the lattice displacement Q_q, giving

$$\Phi(q) = g\left(\frac{2M\omega_q}{\hbar}\right)^{1/2} Q_q, \quad (1.7)$$

With Eq. (1.1), the introduced charge modulation becomes

$$\rho_q = \chi(q,T) g\left(\frac{2M\omega_q}{\hbar}\right)^{1/2} Q_q, \quad (1.8)$$

Thus, the Eq. (5) for $\ddot{Q}_q$ can be written as:

$$\ddot{Q}_q = -\left[\omega_q^2 + \frac{2g^2\omega_q}{\hbar}\chi(q,T)\right] Q_q, \quad (1.9)$$

This equation above gives renormalized phonon frequency, at $q=2k_F$

$$\omega_{ren,2k_F}^2 = \omega_{k_F}^2 - \frac{2g^2 n(\varepsilon_F)\omega_{2k_F}}{\hbar}\ln\left(\frac{1.14\varepsilon_0}{k_B T}\right), \quad (1.10)$$

With decreasing temperature, $\omega_{ren,2k_F}$ drops to 0 at a finite temperature T_0, shown in Figure 1(c). T_0 is defined as T_{CDW}^{MF} as per the mean-field theory [1, 2]. This complete phonon mode softening represents the phase transition to a frozen-in lattice distortion, with a wavelength $\lambda_0 = 2\pi/|\mathbf{q}| = \pi/\mathbf{k}_F$. Since $\boldsymbol{k}_F$ is determined by the electron filling of the band structure in **k** space, a CDW/PLD superstructure in general will be incommensurate with the underlying crystal lattice [2, 4]. Also,

$$k_B T_{CDW}^{MF} = 1.14\varepsilon_0 e^{-1/\lambda} \quad (1.11)$$

where λ is the dimensionless electron-phonon coupling constant. As this approaches T_{CDW}, the phonon dispersion relationship can be shown as such [1]:

$$\omega_{ren,2k_F} = \omega_{2k_F}\left(\frac{T-T_{CDW}^{MF}}{T_{CDW}^{MF}}\right)^{\frac{1}{2}} \quad (1.12)$$

1.1.1.2 The effect on the electronic states

Conventionally, the energy gap of CDW follows the BCS gap equation (both of which are driven by strong electron-phonon coupling), with the gap function at T=0 having [1]:

$$\Delta=2D*\exp(-1/\lambda), \quad (1.13)$$

where D is the energy cutoff, and λ is the electron-phonon coupling constant. Just as in the BCS theory, with temperature dependence, Δ will vanish at the transition temperature $T_{CDW}=\Delta(T=0)/1.76k_B$. The charge carrier concentration in the condensate $n_c(T)$, which is related to Δ(T), can be written as,

$$n_c(T)=n_c(T=0)*\pi*\Delta(T)/4k_BT_P, \quad (1.14)$$

where, $n_c(T=0)$ is the number of electrons in the metallic state. At T=0, the related electron density can be also evaluated as

$$\rho(r)= \rho_0+ \rho_1\frac{\Delta\rho_0}{\lambda r v_F k_F}\cos(2k_f\cdot r+\varphi) \quad (1.15)$$

$$= \rho_0+ \rho_1\cos(q\cdot r+\varphi),$$

as was previously discussed in equation (1).

1.1.2 I-CDW and CDW

"Incommensurate" and "Commensurate" [1, 2, 4, 16] point to the relationship between the periodicity of charge density modulation λ_0 and the underlying lattice constant (supposing a 1D

chain with lattice constant *a*) of the concerned material. With λ_0=n*a,* where n is an integer, it leads to a commensurate CDW; if n is rational number, then it gives rise to an Incommensurate CDW. Usually, I-CDW is the precursor of CDW [17-21]. Since I-CDW may not correspond to the lowest possible energy state, the charge order may cause further distortions, bringing the electron density and underlying lattice into an ordered-state CDW. Thus, CDW is also referred as a "locked-in" state [22]. It commonly takes two phase transitions in order to lock into CDW state in the crystal. The first phase is a Normal State-to-Incommensurate CDW transition [23]. The second phase is an Incommensurate-to-Commensurate CDW transition [24]. In the conventional CDW, a Normal-to-Incommensurate transition is a second order transition, and Incommensurate-to-Commensurate is a first-order transition [23]. According to conventional thermodynamic classification (Ehrenfest 1933) [25], first order phase transitions refer to transitions in which the first derivative of the free energy is discontinuous. Second order phase transitions refer to situations in which the first derivative is continuous, although the second derivative could be discontinuous. In the unconventional CDW, sometimes Incommensurate-to-Commensurate transitions can also be observed as second-order [26]. Another kind of CDW, between Commensurate CDW and Incommensurate CDW, was introduced in 1976 by Mcmillan, called Discommensurate CDW [27]. Discommensurate is like a defect transition, whereas a commensurate CDW is separated by phase-split regions.

A variety of experiments have been conducted to study CDW order. Since CDW and I-CDW are associated with a lattice distortion, they can be observed through Diffraction techniques (X-ray, electron and neutron), where superlattice structure or satellite reflections related to the charge order formation can be observed [17]. For CDW, the spacing of superlattice will be a constant integer

multiple of the reciprocal lattice spacing; whereas, in the case of I-CDW, either the spacing relationship is a rational number, or if not in Selected Area Electron Diffraction diffused diffraction in between the Bragg reflection spots as observed [28, 29]. In most cases, the CDW transition is also accompanied by an opening of energy gap near the Fermi level [1, 2, 4]. Therefore, transport measurements can also be used to study the phase transitions with observation of metal-to-insulator like transition. Conventionally, a thermal hysteresis can be seen in a first-order phase transition (I-CDW to CDW) and no thermal hysteresis in the second order phase transition (Normal-ICDW) [30]. Nevertheless, in some unconventional cases, such as our example using Bi_2Se_3, no thermal hysteresis was observed under the expected first-order transition, shown as Figure 3.3. Local probes such as Nuclear Magnetic Resonance (NMR) measurement can also be applied to examine the local structure changes originating from the structural phase transitions [31]. One of the clearest pieces of evidence of CDW presented here is line shape changing in NMR spectrum, where I-CDW phase can be observed with asymmetric broadening, CDW phase can be observed with splitting lines or "wings" of distribution, and Discommensurate CDW can be observed with phase slip [32]. The experimental NMR observation for CDW will be discussed in detail in chapter 4. Besides the above, other techniques can also study the CDW state, such as Scanning Tunneling Microscope, which is another technique to discover the wave length of the charge modulation as well as the electronic transition, the Raman Spectroscopy to study the CDW developed phonons under the transition temperature, high-resolution ARPES data to estimate the strength of Electron-Phonon coupling in a CDW system, and so on.

1.1.3 CDW in Different Dimensions

1.1.3.1 Classification of CDW

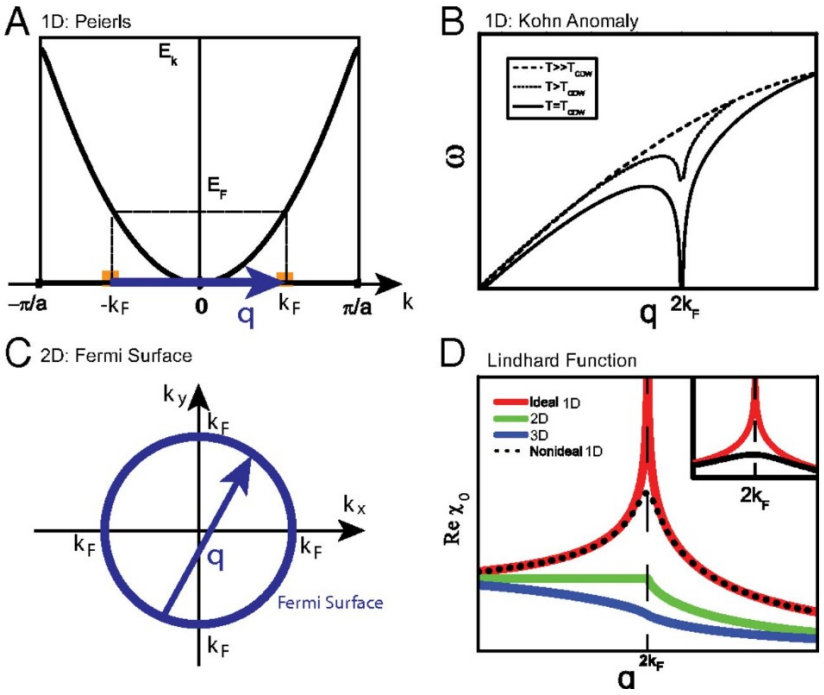

Figure 1.2 CDW in different dimensions (a) and (b) Energy and phonon dispersion in 1D CDW (c) Fermi surface for 2D CDW (d) Lindhard dispersion in different dimensions (Adapted from ref. [33]).

The classification of CDW is also very dependent on dimensions [33, 34]. Here, in this section, I will start with the Lindhard susceptibility function to distinguish CDW at different dimensions from the aspect of Fermi surface topology. Considering a Fermi gas in one, two and three dimensions, the derivation of Lindhard function has been reviewed in Ref [35]. For a system of fermions, with an external potential $\Phi_{ext}(r, \omega)$ which forms from an interaction of an electrostatic field, the total electrostatic potential $\Phi_{tot}(r, \omega)$ can be given as [34, 35]:

$$\Phi_{tot}(r, \omega) = \Phi_{ext}(r, \omega) + \Phi_{ind}(r, \omega), \quad (1.16)$$

where $\Phi_{ind}(r, \omega)$ is the potential contributed from the induced charge distribution. The same behavior can be observed for the total electric charge $\rho_{tot}(r, \omega)$:

$$\rho_{tot}(r, \omega) = \rho(r, \omega) + \rho_{ind}(r, \omega), \quad (1.17)$$

where $\rho(r, \omega)$ is the superposition of the charge distribution of the noninteracting target, and $\rho_{ind}(r, \omega)$ is the introduced charge distribution. They obey Poisson equations:

$$-\nabla^2\Phi = 4\pi\rho. \quad (1.18)$$

In a linear response theory, the induced charge density related to the total potential by a response function has been displayed in equation (3). For a non-interacting Fermi Gas model, without considering electron–electron correlations, the response function can be calculated by Lindhard approximation shown in section 1.1.1 equation (1.4). The Lindhard functions as a function of dimensionality has been displayed in Ref. [34] equation (6) to (8), shown as Figure 1.2(d) here.

1.1.3.2 CDW in Layered Chalcogenides with different Dimensions

Since this dissertation focuses on intercalated Bi_2Se_3, which belongs to the family of layered chalcogenides [36], the following is a brief overview of CDW, as well as associated superconducting state in this material family:

CDW favors low dimensional systems, especially layered chalcogenides, (M) MX_2 and MX_3 chalcogenides (M, represents transition metal from group IV, V or VI, and X represents chalcogen from S, Se or Te. Eg: MoS_2, TiS_2, TaS_2, WS_2, ZrS_2, WSe_2, Sb_2Se_3, $NbSe_2$, and Bi_2Te_3) [17-19, 37]. Regarding cases with Qusi-2D, their structures have strong in-plane bonding but weak out-of-plane interaction (van der Waals Force) [38-41]. By applying pressure or doping, SC in dichalcogenides can be induced/enhanced [41-46]. The mechanism of CDW in these materials are usually related to electron density modulation near the Fermi surface which generates an opening of the energy gap (although in some cases no energy gap opening can be observed—such as 2H-$NbSe_2$ [47, 48]) and causes increased resistivity. Another instability near FS—Superconductivity

(SC), in contrast, results in a zero resistance. Thus, it is generally considered that there is competition between CDW and SC orders [43-45], as shown in Table 1. For example, $ZrTe_3$ has a qusi-2D structure. Pure $ZrTe_3$ has a CDW order at 63K. Under pressure the CDW state is suppressed and enhances the SC state [43]. During intercalation, Cu_x/Ni_xZrTe_3 [44, 45], coexisting CDW and SC were observed in this compound, though this required a slight suppression of CDW order and increased SC. When substituting for Te site, $ZrTe_{3-x}Se_x$ also shows a suppression of CDW order with enhanced SC [46]. With increasing Se content x, the CDW order detected by a-axis resistivity anomaly is suppressed, vanishing around $x = 0.03$. SC T_c gradually increases up to the maximum $T_c = 4.4$ K around $x = 0.04$. Similarly, when Pd substitution and intercalation (Pd_xIrTe_2 and $Pd_yIr_{1-y}Te_2$) into $IrTe_2$ (with strong spin-orbital coupling), both conditions result in suppressed CDW order and enhanced SC [49]. These observations can be simply explained as such: for metal intercalation, more electron carriers are available to change the FS related to SC, and these carriers also partially filled the CDW energy gap; if using a substitute, the in-plane disorder will suppress the CDW(sensitive to disorder), in another way: the number of carriers available for SC pairing will increase, and thus T_c will rise accordingly. However, the underlying correlation between CDW and SC can be more complicated, and it is sample dependent. Depending on doping level, atoms spacings, experimental conditions and sample thickness, the degree of competition between the two states can be minor or large, and in some cases the CDW can also boost SC [44, 45, 50-53].

Table 1.1 Dimensions dependence of SC and CDW ordering in chalcogenides

Material	Dimension	T_{CDW}(K)	T_c (K)/ condition	Relation: Tc and T_{CDW}	Mechanism for CDW
$NbSe_3$[54]	Quasi-1D	145K, 59K	Pressure introduced SC	compete	Fermi Nesting (FN) from chain interaction
$HfTe_3$[55]	Qusi-1D	82K	No need pressure 1.4K	coexist	FN from chain interaction
1H-$NbSe_2$[47,48]	Qusi-2D	7.1K	32K	coexist, while compete under hydrostatic pressure	Electron-phonon coupling
2H-$TaSe_2$[37,40]	Qusi-2D	120(ICDW)-90 K (CDW)	0.14K	compete	FN: An electron instability in the bands nested away from the Fermi surface
2H-TaS_2[39]	Qusi-2D	70K	No pressure 0.8K	compete	FN: a polar charge and orbital order
Na_xTaS_2[41]	Qusi-2D	2.5 to 4.4K	No SC(x=0.1and 0.05) or T_{CDW}=65K,T_c =2.5K with x<0.05	intercalation enhance SC but suppress CDW	FN: anisotropy along c axis
$TaSe_{2-x}S_x$[53]	Qusi-2D	2.5K to 4.1K	15K to 20K	substitution for Se enhance SC but suppress CDW	FN: Suppressed by crystallographic disorder
$ZrTe_3$[43,56]	Qusi-2D crystal	2K	63K	Coexist	FN from Chain interaction driven by the nesting of parallel planar sections of the FS
Cu_xZrTe_3[44]	Qusi-2D	3.8K	57K	Intercalation enhance SC but suppress CDW(at Tc still coexist)	FN Intercalation has minor effect on FS part for CDW but some level suppress it
Ni_xZrTe_3[45]	Qusi-2D	3.1K	41K	Intercalation enhance SC but suppress CDW(at Tc still coexist)	FN Intercalation has minor effect on FS part for CDW but some level suppress it
$ZrTe_{3-x}Se_x$[46]	Qusi-2D	2K-4.4K	0-63K	Substitution for Te enhance SC but suppress CDW	FN from chain Interaction
$IrTe_2$[57]	Qusi-2D	2.4K	280K	coexist	FN

Pd_xIrTe_2[49]	Qusi-2D	1.8K-3K	70-190K	Intercalation enhance SC but suppress CDW	FN
$Pd_yIr_{1-y}Te_2$[49]	Qusi-2D	2K-3K	130-180K	Intercalation enhance SC but suppress CDW	FN

1.2 Topological Materials

1.2.1 Topological Insulator

Topological Insulator (TI) [58-61] is a new state of quantum matter. It is insulating in the bulk state while conducting on the edge(2D) or the surface state(3D). Strong Spin Orbit Coupling (SOC) plays an important role in the topological property of TI. Due to the SOC interaction, the spin and momentum locked to each other give rise to a non-trivial berry phase and suppress the back scatterings under time reversal symmetry protection, leading to potential applications in Quantum computing and spintronics devices. Also, Z_2 invariant determination can be used to distinguish between the trivial insulator and the non-trivial topological insulator.

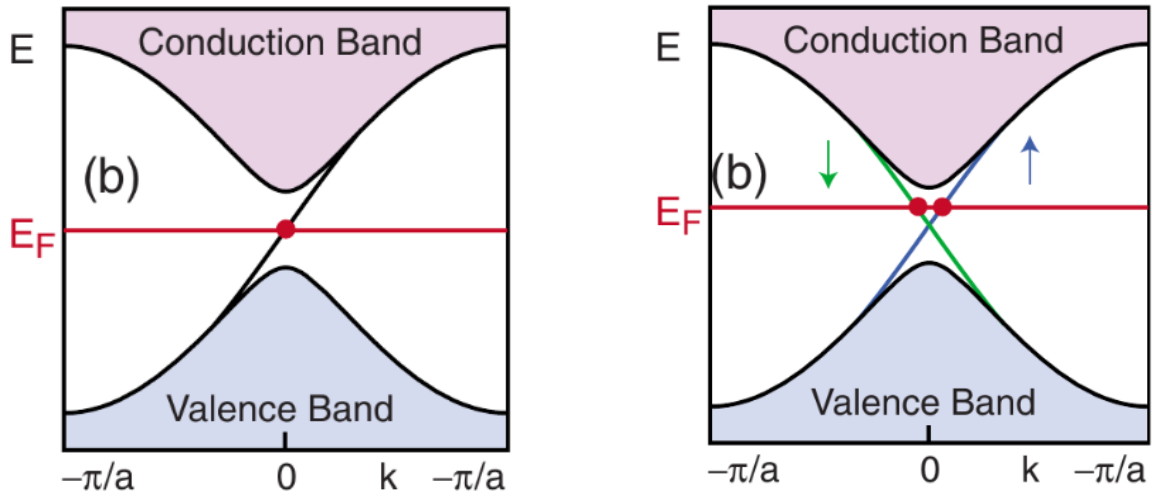

Figure 1.3 Energy state vs moment for (a) Quantum hall and (b) Quantum spin hall (Ref. [61]).

The Integer Quantum Hall (IQH) effect [60] is the foundation for determining topology order. Under low temperature, high outer magnetic field, 2D electrons gas in the semiconductor will do cyclotron motion in the bulk state and act as insulators. However, when placed near the outside, electrons cyclotron motion will bounce outwards towards the edges and make a continue 1D conducting loop which overcomes any backscattering. The hall conductivity is quantized under the magnetic field. The longitudinal conductivity has value on the field transition point, but its value drops to 0 under constant field, with the bulk gap closing at the transition and opening again at the constant field. The band structure IQH is quantized by the Landau levels. Like an insulator, an energy gap separates the occupied Landau level to the unoccupied Landau level, and the E_f level lies in between the gap.

The Quantum Spin Hall Effect [60][61] is the topological insulator in 2D. A big breakthrough to IQH is QSH, which can happen at room temperature with interior magnetic field. This is the motion produced from the up spin and down spin. On the edge of QSH insulator, there are two channels for the electrons: one from the up spin and one from down spin. If an electron moves under an applied electric field, the up and down spins will have opposite flowing currents, and hall conductivity is 0, though it does have quantized spin hall conductivity. Also, due to the two spin channels, it will have double quantum hall effects which lead to a gapless edge state. When the electron moves around a nonmagnetic impurity, the paths of two spin rotations are different by 2π, thus the two backscattering is destructive interference, and so QSH is protected by the time reversal symmetry. Also, the Z_2 quantum number odd or even effect is the central role to characterize the topological insulator nature of QSH.

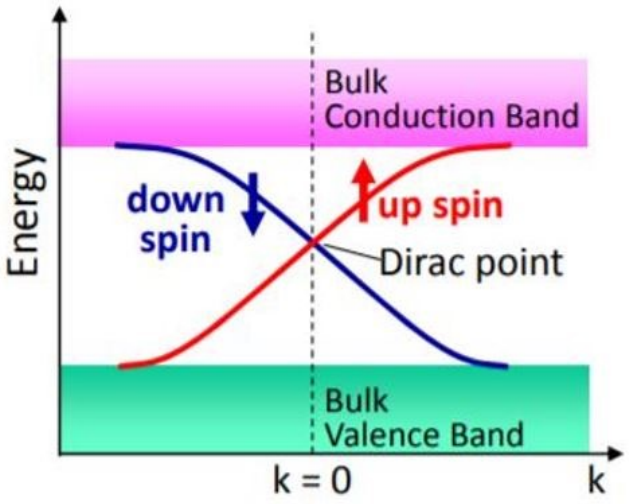

Figure 1. 4 Schematic k-space picture of the 2D helical surface state of a 3D TI (Adapted from Ref. [61]).

The first discovered 2D TI is HgTe/CdTe quantum well [61], in which HgTe is sandwiched in between the CdTe layers. With the changing thickness of HgTe, the strong spin orbit coupling interaction leads to a s and p orbits inversion in HgTe. Since the s and p states carry opposite Parity, the bands cross each other at certain critical thickness, introducing a gapless edge state and correspondingly leading to a trivial insulator to QSH transition.

3D TIs can be characterized by four Z_2 invariants (γ_0; γ_1 γ_2 γ_3) [61]. If one of the invariants is non-zero, then it will follow topological protection of states. A weak topological insulator with $\gamma_0=0$ is layered by 2D quantum spin hall insulators in which the connected edge states form the conducting surface state. And a strong topological insulator is when $\gamma_0=1$, forming a single Dirac Cone at the surface state.

The first experimental discovery of a 3D TI was in $Bi_{1-x}Sb_x$ [61]. A single Dirac Cone is found at the interface of conduction band and valance band of the surface state by the Angle-Resolved Photoemission Spectroscopy (ARPES). When the observed surface band crosses the Fermi surface an odd number of times, the surface state is under topological protection or "topologically protected." After the discovery of this material, the second generation of TIs were found from variations of, and intercalations into, Bi_2Se_3, Bi_2Te_3 and Sb_2Te_3. In this work, we will focus on the Bi based-topological insulator by substituting and intercalating different metals.

1.2.2 Crystal Structure of Bi_2X_3

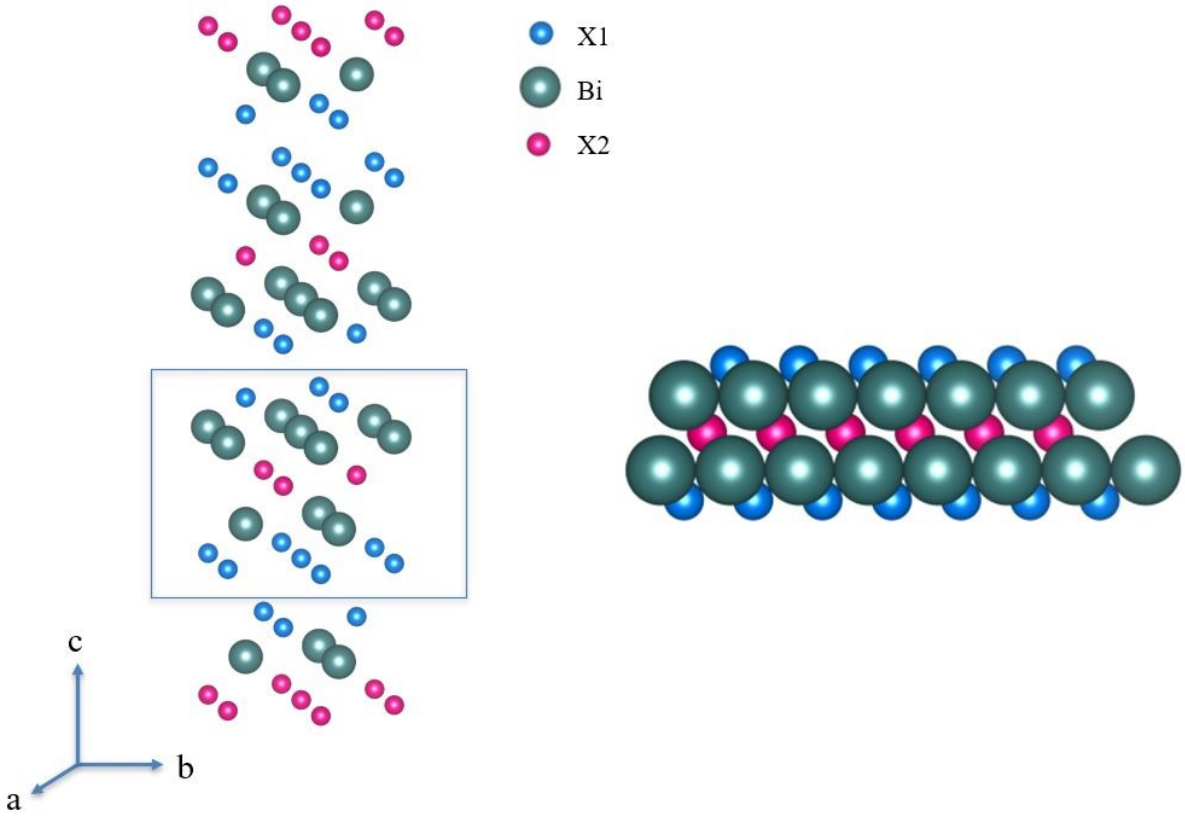

Figure 1.5 Crystal structure of Bi_2X_3 (a) and its ABC stacking order along c-axis. (b) Blue solid ball represents outer layer X1 for Se/Te; Green solid ball represents Bi and pink solid ball represents the inner layer X2 for Se/Te.

The bulk crystal of Bi_2X_3 (X=Se, Te) belongs to D^5_{3d}, R$\bar{3}$m space group [62]. Its primitive unit cell is Rhombohedral structure, with 5 atoms in each unit cell. As shown in Figure 1.5, the 5 atoms inside the primitive unit cell of Bi_2X_3 are arranged as X(1)-Bi-X(2)-Bi-X(1), where the two X(1) are equivalent while X(2) is a different type and assumes the role of inversion center [62]. Under inversion, Bi mapped with Bi and X(1) mapped with X(1), such as Se(1)-Bi-Se(2)-Bi-Se(1) for Bi_2Se_3 and Te(1)-Bi-Se(2)-Bi-Te(1) for Bi_2Te_2Se. The stacking sequence for Bi_2Se_3 is [63]: –[Se1-Bi-Se2-Bi-Se1]$_0$–[Se1-Bi-Se2-Bi-Se1]$_{1/3}$–[Se1-Bi-Se2-Bi-Se1]$_{2/3}$–. The crystal lattice constants are a=b=4.14 Å, c=28.66 Å (see chapter 3); Bi position 6c (0,0,0.3985); Se(1) position 3a (0,0,0); Se(2) position 6c (0,0,0.2115). Bi_2Te_2Se has the isostructural as Bi_2Se_3 and Bi_2Te_3, although it is considered the most ordered structure out of these three [64], which overcomes the commonly observed vacancy defects in Bi_2Se_3 [65] and anti-site defects in Bi_2Te_3 [66]. The stacking sequence for Bi_2Te_2Se is: –[Te-Bi-Se-Bi-Te]$_0$–[Te-Bi-Se-Bi-Te]$_{1/3}$–[Te-Bi-Se-Bi-Te]$_{2/3}$–. The crystal lattice parameters of Bi_2Te_2Se are: a =b= 4.3 Å, c = 29.94 Å (See chapter 5); Bi position 6c (0,0,0.3968); Se position 3a (0,0,0); Te position 6c (0,0,0.2116).

The supercell of Bi_2X_3 has a hexagonal structure with quintuple layers (QL) of atoms stacked along the trigonal axis, in which each atomic layer has three possible positions stacked in A-B-C-A-B-C….arranged in ABC order [62], as shown in Figure 1.5 (b). In the hexagonal basis, each unit cell contains 3 QLs and thus 15 atoms. The coupling between each two atoms planes within a QL is a strong covalent bond, while between the QLs are weak van der Waals interactions, which allows the crystal to be easily cleaved along inner QL plane. In the point group, the three important symmetry axes for these crystals are: the trigonal axis (c-axis) representing the three-fold rotation

symmetry, binary axis (a-axis) representing two-fold rotation symmetry and the bisectix axis (b-axis) in the reflection plane [67].

1.2.3 Common Defects in Bi_2X_3

Native defects in Bi_2X_3 play an important role in changing the topological properties as well as electronic state properties [68-74]. Some common native defects have been found in Bi_2X_3, including vacancy defects, antisite defects, point defects and interstitial defects. Bi_2Se_3 naturally has Se vacancy defects, which is the reason for most experiments which show n type conduction [71, 72]. Recent studies, as well as our own measurements, also found Bi_{Se1} antisite and partial Bi_2-layer intercalation defects, which also can change the conducting properties [70, 73]. Figure 1.6 displays an APRES measurement on naturally electron doped Bi_2Se_3 with hexagonal Fermi deformation, where parallel components on the hexagon can lead to a density wave order [68]. Bi_2Te_3 most commonly found Bi_{Te} antisite defects showing (p-type) or Te_{Bi} antisite defects showing (n-type) [69]. Bi_2Te_2Se was considered to be the most ordered compound; however, native defects were also found in this material [75, 76].

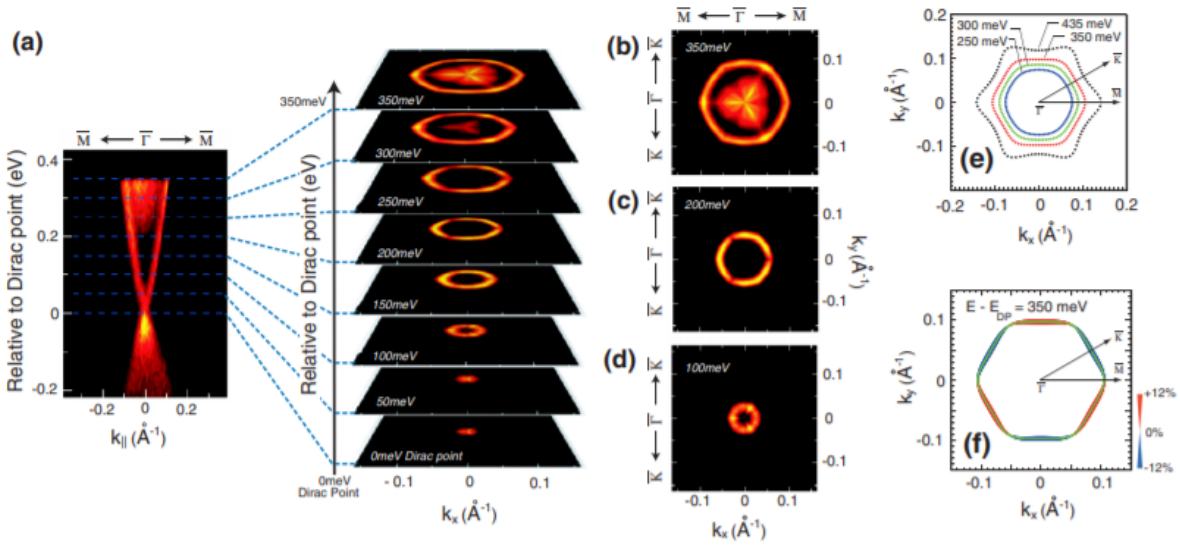

Figure 1.6 Fermi surface deformation in self-doped Bi_2Se_3 from APRES measurement ((a)-(f) were taken from Ref. [68]).

1.2.4 Topological Superconductors

1.2.4.1 Conventional Superconductivity

Superconductivity [77] was first observed by Kamerlingh Onnes in 1911. When he performed the transport measurement for Mercury, he found that at a critical temperature T_c, the electrical resistance of the sample undergoes a phase transition from normal state to superconducting state with zero resistance observed. Conventional Superconductivity is usually described by the BCS(Bardeen–Cooper–Schrieffer) theory [78], which considers from the microscopic quantum state that the one particle orbitals are occupied by pairs of electrons, also called Cooper pairs. The Cooper pairs (particle pairs for k↑ and -k↓) originate from the attractive interaction of electron-electron pair through the mediation of phonons. A simple depiction of this model can be thought of as a situation in which one electron state interacts with the lattice and leads to a deformation, whereas a second electron "sees" this deformation and uses it to pair with the other electron state

lower its own energy. This can be thought of as the second electron interacting with the first electron through the lattice and forming an electron-lattice-electron interaction, or an electron-electron Cooper pair [79]. This formation of these paired electrons due to Fermi energy instability can further cause a ground state to separate from its lowest excited states by an energy gap E_g, which can be observed from thermal properties, local nuclear properties, and most of the electromagnetic properties.

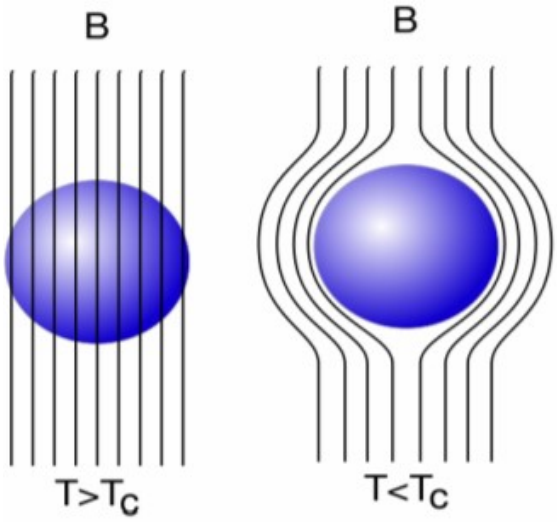

Figure 1. 7 Meissner Effect at $T>T_c$ and $T<T_c$

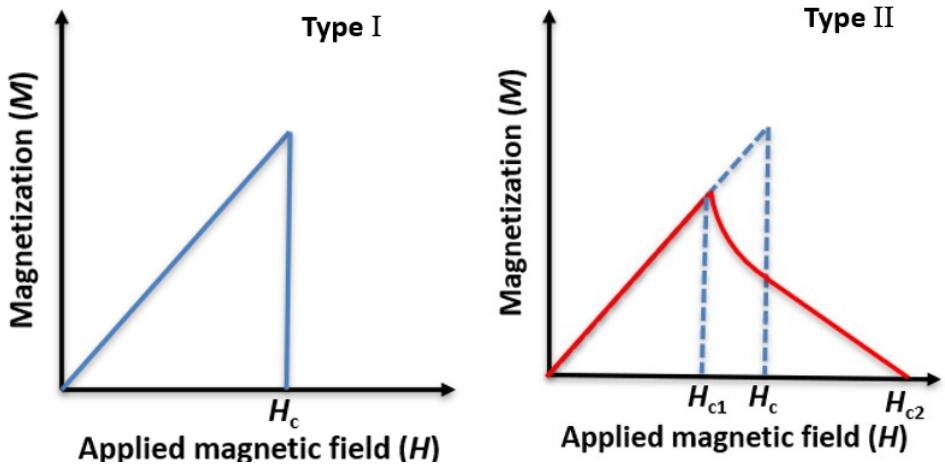

Figure 1.8 Magnetization as a function of magnetic field for a type I superconductor and a type II superconductor.

The Meissner Effect is the most important observation to consider when a material is in the superconductor state [80]. As displayed in Figure 1.7, Meissner effect indicates a perfect diamagnetism for superconductor. When the superconducting sample is placed in a certain magnetic field, with cooling to the superconducting transition temperature T_c, the magnetic flux originally present inside of the sample will be ejected. When increasing the magnetic field to above a critical field $H_c(T)$, the superconducting state will be destroyed by the strong magnetic field and go back to the normal state. Based on the magnetic behavior, superconductors can be categorized as type I or type II superconductors [90], as seen in Figure 1.8. A type I superconductor has no intermediate state, keeping out the whole magnetic field until reaching the critical field $H_c(T)$. After $H_c(T)$, the magnetic field will fully penetrate the material. In type II superconductors, there is an intermediate state called vortex state, which appears before reaching the normal state. At low magnetic field, a type II superconductor will behave like a type I superconductor, expelling the entire magnetic field out until a first critical field $H_{c1}(T)$ is reached. Note that, whether the entire magnetic flux is expelled depends upon the shape of the superconductor and the direction of the applied magnetic field. Above Hc_1, the superconductor gets into the vortex state, where the magnetic field partially penetrates the material until reaching the second critical field $H_{c2}(T)$. H_{c2} is usually considerably larger than H_c, which is why type II superconductors are typically used for superconducting magnets. Another important difference between the two types of superconductors is the relationship between coherence length ξ (a length within which the superconducting electron concentration does not change drastically in a spatially-varying magnetic field) *vs* the penetration depth λ (the depth of penetration of the magnetic field into the superconductor). If $\lambda/\xi<1$, it is type I superconductor; if $\lambda/\xi>1$, it is type II superconductor.

1.2.4.2 Topological Superconductivity

Compared to conventional superconductivity, where Cooper pairs are bound via an electron-phonon interaction, the term "unconventional superconductivity" refers to other types of interaction mechanisms, or additional broken symmetries [81]. The Topological Superconductors (TSCs) involves the interplay of topologically-ordered phases and broken-symmetry states, which has an unconventional order parameter with an orbital component containing a chiral $p_x + ip_y$ wave term [82]. The nontrivial topology of the bulk state in TSCs can lead to the emergence of Majorana bound states (MBSs) within the bulk superconducting gap [83]. A Majorana fermion is a hypothetical particle which is its own antiparticle. In TSCs, electrons (at energy state E, above the Fermi level) and holes (at energy state -E, below Fermi level) play the role of particle and antiparticle, where the 2e charge differences can be absorbed as a Cooper pair in the superconducting condensate. At the Fermi level, located in the middle of the superconducting gap, the eigenstates are charge neutral superpositions of electrons and holes. The excitations at the Fermi level in between the superconducting gap are Majorana fermions states which follow electron-hole symmetry. Specifically, at the Fermi level, it is followed by $\gamma(0) \equiv \gamma = \gamma^{\dagger}$, where $\gamma^{\dagger}(E)$, $\gamma(E)$, $\gamma(0)$ are the creation and annihilation operators, and a single zero mode , thus particle and antiparticle coincide [83]. Majorana fermions in superconductors can lead to well-defined two-level systems—qubits, and potentially can be applied to designed quantum information systems and quantum computers [84, 85].

In order to make Majorana fermions a reality in superconductors, one option available is to remove its degeneracies through breaking its spin-rotation and time-reversal symmetries [83]. Many superconductors have recently been indicated to host topological superconductivity in bulk [86].

Among these TSC candidates, intercalated Bi_2Se_3 superconductors have been the subject of much attention and speculation [87-90]. Theoretically, intercalated Bi_2Se_3 has been proposed to hold nematic superconductivity as well as non-trivial topological SC gap [91]. With an increasing number of experimental observations of nematic order in these compounds [90, 93, 94], more and more light is being shined on the observation of potential topological superconductivity. A more detailed discussions as follow:

(a) Intercalated Bi_2Se_3 superconductors:

Bi_2Se_3 as a topological insulator has been discussed in section 1.2.2. With its unique layered structure and van der Waals gap in between the QLs, when Bi_2Se_3 is intercalated with a metal atom, the metal atom tends to go to its weak van der Waals gap.In principle, this intercalation can further change the electronic band structure and lead to superconductivity. Even though the underlying mechanism for superconductivity in topological insulators is still under debate, most groups agree that intercalation seems to play a key role in the underlying electric properties [95, 96]. Hor el at. [95] was the first group showing that Cu intercalation can lead this compound to show superconductivity, with T_c=3.8K. After that different groups have studied Cu-, Nb-, Sr-intercalated into Bi_2Se_3, all of which show superconductivity [87-90].

(b) Observation of Nematic Order

Most interestingly, nuclear magnetic resonance, magnetic torque, upper critical field, magnetization, and STM spectra show that Cu-, Sr-, and Nb- intercalated Bi_2Se_3 superconductors also host nematic orders which can potentially lead to bulk TSCs [93, 97-99]. Here, nematic order refers to the in-plane three-fold rotational symmetry in intercalated Bi_2Se_3 superconductors. This nematic order is spontaneously broken into a two-fold rotational symmetry below the superconducting transition temperatures, which further indicates that rotational-symmetry is

broken in the superconducting gap amplitude and superconducting spin degree of freedom. When the superconducting phase is in the nematic state consistent with Eu symmetry, it can lead to broken rotational symmetry. Furthermore, in the Eu representation, another topological superconducting phase--a nodal Weyl superconductor that supports Majorana arcs on the surfaces can spontaneously break the time-reversal symmetry. For these and other reasons, the intercalated Bi_2Se_3 is widely considered be a potential topological superconductor [90].

1.2.4.3 Phonon mediated unconventional superconductivity

Even though there are different theories for the origins of unconventional superconductivities in intercalated Bi_2Se_3 [91, 100], to relate my observations of CDW in these compounds, I emphasize on the phonon mediated mechanism. The phonon mediated unconventional superconductivity in intercalated Bi_2Se_3 was first proposed by Wan & Sergey [101]. Unlike most unconventional superconductors where electron-electron correlations lead to unconventional behavior, Bi_2Se_3 has weakly correlated *sp* electrons, which is another leading factor needs to be examined in order to explain this unique superconductivity. From first principles linear response calculation, they found the superconductivity in doped Bi_2Se_3 was driven by an unusual electron-phonon interaction due to strong Fermi nesting at long wavelengths along the Γ-Z direction. Furthermore, the anisotropic electron-phonon coupling and strong Fermi Nesting has been confirmed from Neutron scattering measurements in Sr- Bi_2Se_3 [102] as well as in previous APPRES measurement for Cu interacted Bi_2Se_3 with an observation of an open-cylinder-like electron point pocket along the Γ-Z direction near zone center [103]. This will be discussed in greater detail in chapters 3 and 4.

Chapter 2: Special Techniques

2.1 Nuclear Magnetic Resonance Measurements

2.1.1 Basic Principles

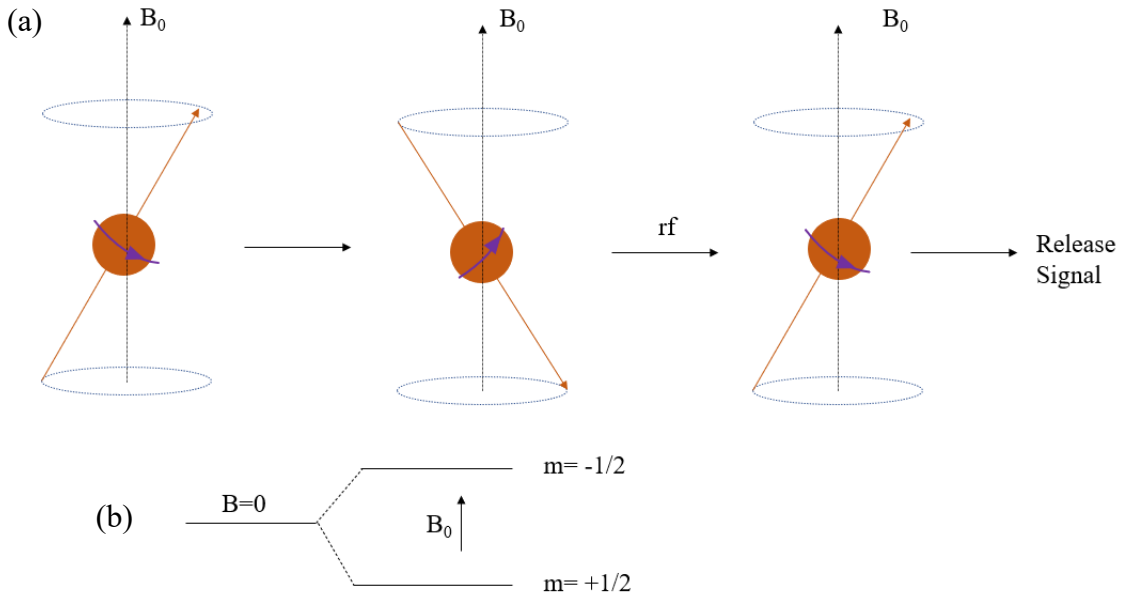

Figure 2.1 NMR mechanism. (a) RF irradiation to a ½ nuclear spin, with static field in the z-axis direction. (b) Zeeman splitting.

NMR is a technique used to study the immediate local surroundings of an atom's nucleus in a compound [104, 105]. Like electrons, nuclei also have degenerate quantum energy levels designated as up spins and down spins. When there is no external magnetic field applied, all the spins remain at the ground state energy. When external magnetic field is applied, nuclear Zeeman splitting will happen ($\mathcal{H}=\mu*B_0*\cos(\theta)$, $\mu=\gamma J$ and $J=\hbar I$, *(in this section, assuming all the applied static field in the z direction*), causing degeneracy to be lifted. The energy differences between an up spin and a down spin (assuming it is a ½ spin) is proportional to the applied magnetic field, and is given by $2\mu B_0=\gamma\hbar B_0$, Figure 2.1 (b). If we add pulses of electromagnetic waves $B_1(t)$ along the

perpendicular axis of the static field (static field at z direction), when the photon energy from the applied pulse is just equal to the energy gap from the two spin states, then nuclear magnetic resonance will occur, shown in Figure 2.1. The up spin will jump to a higher energy level. As it falls back to the lower energy level (back to thermal equilibrium), it will release a signal that we can study by NMR, as displayed in Figure 2.1(a). With $\gamma\hbar B_0=\Delta E=\omega\hbar$, the resonant frequency in NMR is $\omega_0=B_0\gamma$, where B_0 is the applied static magnetic field and γ is the gyromagnetic ratio which depends on the specific nuclei. For different elements, such degeneracy is lifted for different combinations of magnetic field and frequency. The specific frequency of resonance, ω_0 is also called Larmor frequency and is specific to each NMR active nucleus.

2.1.2 NMR Spectrum and line shape

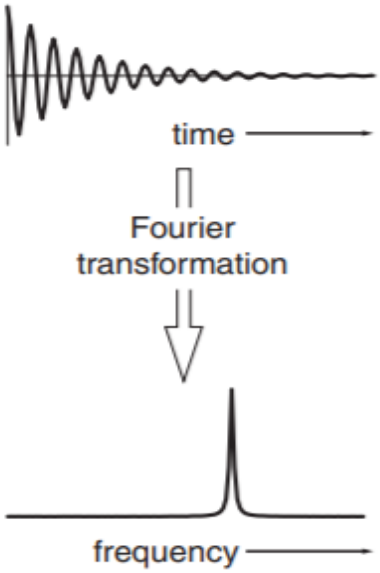

Figure 2.2 An example of Free Induction Decay (FID) and its fast Fourier Transformation (FFT) for a ½ spin.

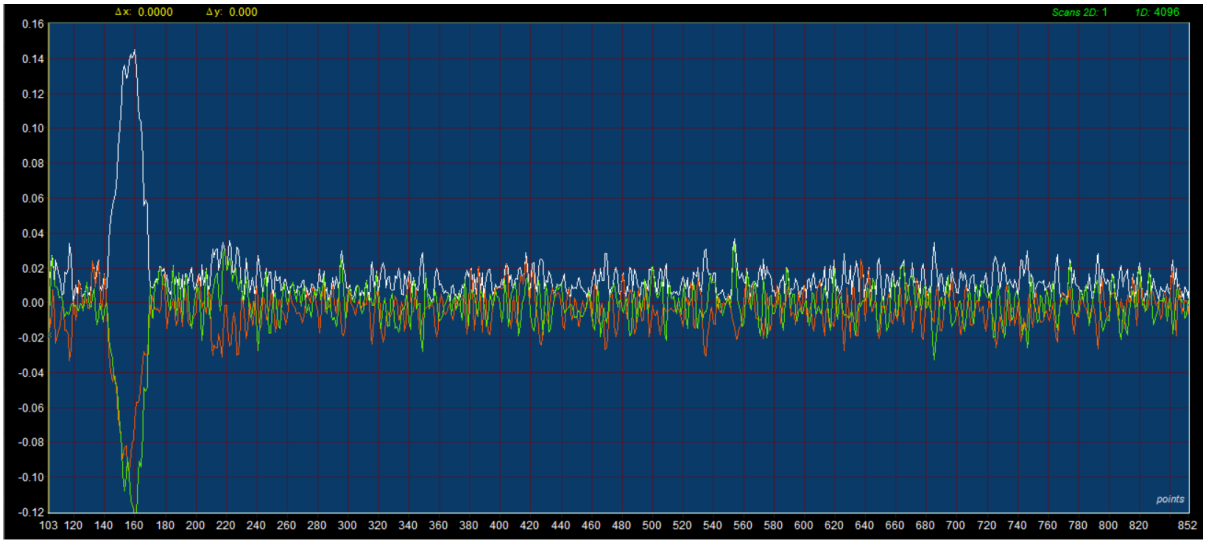

Figure 2.3 Spin-Echo for ^{209}Bi FID in $Nb_{0.05}Bi_2Se_3$ (x- and y-axis are Intensity vs Time).

Figure 2.4 FFT of Figure 2.3--NMR spectrum with 9 peaks from 9/2 spins of ^{209}Bi. x- and y-axis are Intensity vs Frequency.

When it is applied with a static magnetic field, the magnetic moment of the nuclei will try to align with the magnetic field axis. In a solid state, bulk magnetization originated from all the individual

nuclei are joined together, with $\mathbf{M}=\sum \boldsymbol{\mu}_i$ (μ_i *is the magnetic moment of nuclei* i). With applying radiation along the perpendicular axis of the static magnetic field, the net magnetization will tilt to one side or the other. As it spirals back to thermal equilibrium, a decaying electrical signal in the time domain will be introduced, which is called Free Induction Decay (FID) [105]. The NMR spectrum is obtained from Fourier transformation of FID from time domain to frequency domain, as displayed in Figure 2.2, which is a plot of the nuclear population resonating at a particular frequency. A simple Fourier transformation from time domain to frequency domain can be expressed as:

$$S(\omega) = \int_{-\infty}^{\infty} S(t) e^{-i\omega t}\, dt, \tag{2.1}$$

The set of RF pulses applied to a sample to produce the NMR spectrum is called a pulse sequence. Normally, the pulse sequence setup has 90-FID pulse sequence and Spin-Echo sequence (a back-to-back FID), such as Figure 2.3. In the 90-FID pulse sequence, net magnetization is rotated down into the x'-y' plane in the laboratory frame with a 90° pulse [106]. The magnitude of magnetization will decay over time. Spin-Echo sequence immediately follows the first 90° pulse, and a 180° pulse is applied to realign the magnetization and produce an echo signal.

After the rf radiation, as the magnetization tries to return to equilibrium, the nuclei spin will also interact with lattice and other degrees of freedom. Thus, phase transitions in the material can be represented by linewidth change and knight shift of the NMR Spectrum. Such as in the case of CDW phase transition, a broadening of the linewidth at temperature below the T_{CDW} can be observed as an increased Full width at half maximum (FWHM) [106, 107]. More specifically, contributions to NMR line shape have homogenous and inhomogeneous factors, where

homogenous line shape usually found in solids and single crystals can be fitted with Gaussian, while the inhomogeneous line shape has separate parts that originated from separate contributions [107]. The line broadening can either be due to inhomogeneous line shape or to a wide range of homogenous factors such as phase transitions. In the case of CDW, below the transition, the periodic modulation of the charge density can lead to periodic modulation of the electric-field-gradient tensor. This leads to further changes in the frequency associated with the transitions between the nuclear levels, which can be shown as a line broadening [2]. The symmetry effects are particularly spectacular on the electric field gradient since the NMR quadrupolar interaction magnitudes are in general large, where even very small local distortions can be detected [108-111].

2.1.3 Knight Shift and Hamiltonian

The internal crystal field in the material causes a relative shift compared to the expected resonant NMR frequency. This is called the Knight shift [105-107]. The Knight shift can usually written as: K= $\frac{\omega_{ref}-\omega}{\omega_{ref}} \times 100\%$ or for the field sweep spectra (where the RF signal is held constant and the magnetic field is swept): K= $\frac{H_{ref}-H}{H_{ref}} \times 100\%$.

The Nuclear Spin Hamiltonian is very complicated. With considering the external and internal interactions, it can be written as [105]:

$$\mathcal{H} = \mathcal{H}_{ext}+\mathcal{H}_{int}, \quad (2.2)$$

$\mathcal{H}_{ext}$ -terms from interaction with external magnetic field, including contributions from applied static field $\mathcal{H}_{\mathrm{Z}}$ and Rf field $\mathcal{H}_{\mathrm{RF}}$; $\mathcal{H}_{int}$ -terms from interactions with conduction electrons, including contributions from Fermi Contact Term (interaction between the resonating nucleus and the s-electrons) $\mathcal{H}_{\mathrm{CSA}}$, dipolar coupling (The magnetic dipolar interaction) $\mathcal{H}_{\mathrm{D}}$, Orbital coupling

(between spin and electron orbital) $\mathcal{H}_J$ and quadrupole coupling $\mathcal{H}_Q$. Thus, the total Hamiltonian $\mathcal{H}$ can be written as:

$$\mathcal{H} = \mathcal{H}_Z + \mathcal{H}_{RF} + \mathcal{H}_{CSA} + \mathcal{H}_D + \mathcal{H}_J + \mathcal{H}_Q. \quad (2.3)$$

2.1.4 Spin-Lattice Relaxation and Spin-Spin Relaxation

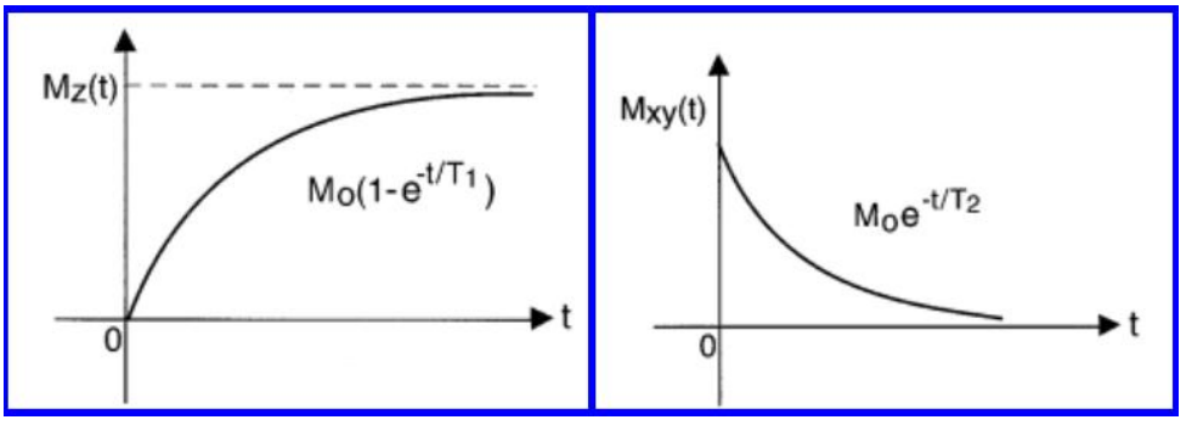

Figure 2.5 Spin Lattice Relaxation T_1 (left figure: longitudinal magnetization recovery $M_z(t)$ vs time t) and Spin-Spin Relaxation T_2 recovery (right figure: transverse magnetization decay $M_{x,y}(t)$ vs time t).

Spin-Lattice Relaxation (T_1) [105] refers to the recovery time for longitudinal magnetization (M_z). In this process, the nuclear spins will exchange energy through interaction with the solid state lattice. Spin-Spin Relaxation (T_2) refers to the recovery time for transverse magnetization ($M_{x,y}$). In this process, there is no energy exchange (since no Zeeman transitions), but only relaxation through interaction with other neighboring nuclear spins.

If we consider the torque experienced by a single nucleus under an uniform magnetic field, then we will have: $\mathbf{T}=\boldsymbol{\mu} \times \boldsymbol{B} = \frac{d\boldsymbol{J}}{dt}$, where $\mathbf{J}$ is the angular moment. Since $\boldsymbol{\mu} = \gamma \boldsymbol{J}$, we can write the

torque equation as: $\gamma \boldsymbol{\mu} \times \boldsymbol{B} = \frac{d\boldsymbol{\mu}}{dt}$. Since the net magnetization $\mathbf{M}=\sum \boldsymbol{\mu}_i$, so, for a spin ½ system, we can have:

$$\gamma \boldsymbol{M} \times \boldsymbol{H} = \frac{d\boldsymbol{M}}{dt}, \tag{2.4}$$

We can write the above equation as x, y and z components:

$$\frac{dM_x}{dt} = \gamma(\boldsymbol{M} \times \boldsymbol{H})_x + \frac{M_x}{T_2}; \tag{2.5}$$

$$\frac{dM_y}{dt} = \gamma(\boldsymbol{M} \times \boldsymbol{H})_y + \frac{M_y}{T_2}; \tag{2.6}$$

$$\frac{dM_z}{dt} = \gamma(\boldsymbol{M} \times \boldsymbol{H})_z + \frac{M_0 - M_z}{T_1}; \tag{2.7}$$

The above (2.5), (2.6) and (2.7) equations are also called Bloch equations to represent the motion of magnetization; The second terms in (2.5), (2.6) and (2.7) equations represent the magnetization relaxation rate in each direction with only considering the static field H_0. To simplify the equations, we can write M_z, M_{xy} going back to thermal equilibrium equations as [105-107]:

$$\frac{\mathrm{dM_z}}{\mathrm{dt}} = \frac{\mathrm{M_0 - M_z}}{\mathrm{T_1}}, \tag{2.8}$$

$$\frac{\mathrm{dM_{xy}}}{\mathrm{dt}} = -\frac{\mathrm{M_{xy}}}{\mathrm{T_2}}, \tag{2.9}$$

With, $M_z(t) = M_0 e^{-\frac{t}{T_1}}$ and $M_{xy}(t) = M_0 e^{-\frac{t}{T_2}}$

where M_0 is the magnetization at equilibrium, and t is the decay time in each case. Figure 2.5 is used to display the magnetization recovery time exponential graphs.

2.1.5 Instruments

In this dissertation, NMR measurements were performed from two different sweepable superconducting magnets with maximum external static magnetic fields 11T and 18T for each of

them, where the 11T magnet was used for studying ^{209}Bi in Bi_2Se_3 sample and the 18T magnet for ^{209}Bi in $Nb_{0.05}Bi_2Se_3$. In the NMR instrument setup, the probe was inserted into a home-built double wall cryostat with a needle valve on the bottom to control the liquid ^4He flow, as shown in Figure 2.6. The cryostat can reach temperatures as low as 4.2K, where the temperature was measured using a Lakeshore Model 340 temperature controller. By pumping the sample space even more, the temperature can drop to 1.6K.

Figure 2.6 The 11T magnet inside of home-built double wall cryostats with side view (a) and top view (b).

The ^4He NMR probe contains an RF coil with the sample placed inside of a rounded copper wire shell and necessary circuits (containing the rf electronic circuit for tuning and matching of the resonant frequency through the coil) for pulsing as well as receiving the nuclear signal, shown in figure 2.7 (b). A goniometer was attached to the bottom of the probe, which can be used to control the angle between concerned crystal plane of the sample and the static magnetic field. During

measurements, the angles were manually controlled and were able to rotate to up to 360 degrees.

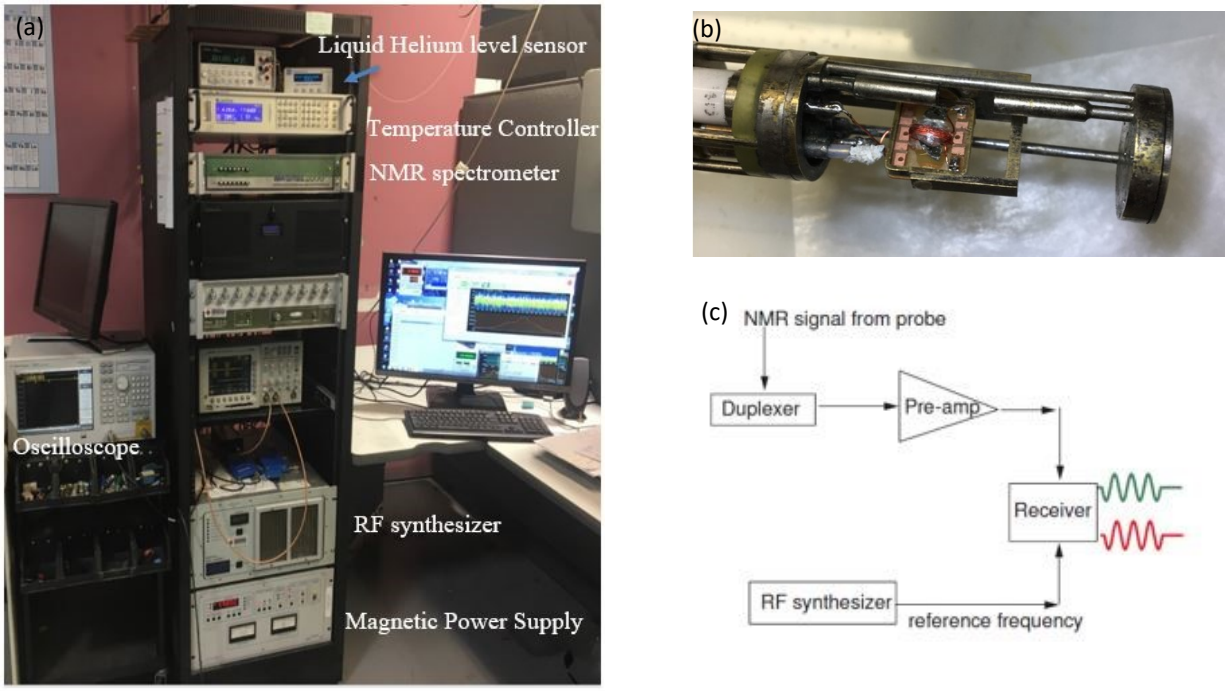

Figure 2.7 NMR instruments (a) NMR instruments set-up, (b) sample inside of rf coil and (c) Schematic diagram of the receiver section ((c) was adapted from Ref. [106]).

As displayed in Figure 2.7, the NMR hardware are labeled as shown in Figure 2.7 (a). NMR measurements were operated by a home-coded Magres2000 software through the user interface and later processed. First, a radio frequency synthesizer generates an oscillating electrical signal at the reference frequency ω_{ref}, with an output of $s_{synth} = \cos(\omega_{ref} t+\varphi(t))$ (φ is the rf phase). Simultaneously, the rf pulses are increased to a higher amplitude by means of a power amplifier. Then, the rf pulses pass through a duplexer (a bi-directional signal travel device) and transmit through the probe and rf coil (Figure 2.7(b)) to the sample. After the resonance, the concerned nuclear signal will also be released through the same coil and travel back to the duplexer through NMR probe. The weak NMR signal (10^{-6} V) will then be amplified through a pre-amplifier and

sent to the spectrometer's receiver. Finally, the received signal will be displayed on the Magres2000 software. Besides the NMR basic setup, General Purpose Interface Bus (GPIBs) were used to connect computer with the magnetic power supply, the liquid helium level detector, and the Lakeshore Model 340 temperature controllers.

2.2 Transmission Electron Microscopy (TEM)

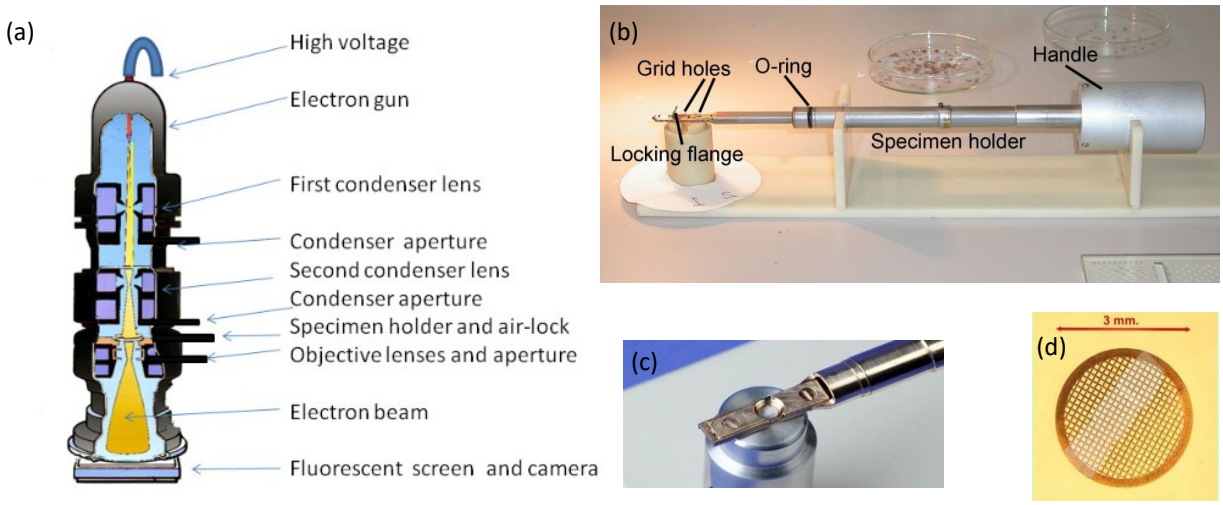

Figure 2.8 Transmission Electron Microscopy Instruments. (a) Instrument layout (b) sample holder and its component (adapt online) (c) Grid holder (d) Copper grid (all the figures here are adapted online).

The first TEM instrument was built by Max Kroll and Ernst Ruska in 1931, and the first TEM was produced for commercial purposes in 1939 [112]. When studying crystals, Transmission Electron Microscopy (TEM) is a powerful microscopy technique, which can be used to study the crystal structure, superlattice, defects and grain boundaries of a crystal. As shown in Figure 2.8 (a), the processing of TEM imaging is: First, a V-shaped filament made of LaB_6 or W (tungsten) will be heated up to (hundreds of keV) to generate the electron beams; second, the electron gun will pass

through the magnetic lenses, which are used to focus the beam of electrons of the specimen; third, the focused beam of electrons will reach, interact with and then transit through the specimen, where the transmitted electrons will form an image; finally, the image will be magnified and focused onto the imaging device, such as a CCD camera. TEM is a high-vacuum system: near the electron source area, a vacuum of 10^{-7} to 10^{-10} mbar must be used to prevent oxidation/burning of the heated filament; The column and the specimen area are evacuated steadily to a vacuum of 10^{-5} to 10^{-7} mbar with liquid nitrogen cooling the specimen area.

An ultra-thin specimen is required in order to transmit sufficient electrons and to form an image with minimum energy loss [113]. If a specimen is too dense, most electrons will scatter and form a dark area. Thus, the specimen preparation is key to getting the right TEM result. For most electronic materials, preparatory techniques are used in this order: ultrasonic disk cutting, dimpling, and ion-milling. Likewise, in my measurements, I gently implemented a mechanical grinding method. After sample preparation, sample will be placed on a 3mm wide copper grid and then placed into the sample holder, as shown in Figure 2.7 (d).

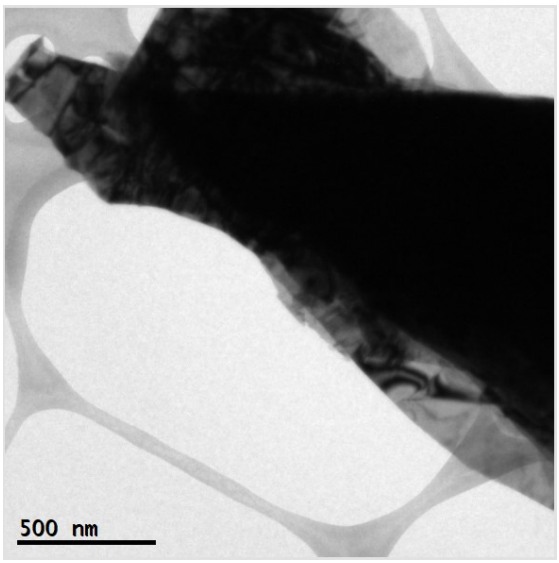

Figure 2. 9 Example of a bright field image on a Bi_2Te_2Se sample, where the dark reflection is the Bi_2Te_2Se sample, the light reflection is the carbon background.

There are two types of TEM imaging methods, bright-field and dark-field images. Bright-field imaging (example in Figure 2.9) refers to the unscattered (transmitted) electrons being selected in the aperture while the scattered electrons are blocked [114]. Thus, the crystal lines or high mass density area of the sample will form a dark region, whereas the remaining area surrounding the sample region will appear brighter in color. Dark-field TEM imaging is the opposite, where the scattered electrons are selected, and unscattered electrons are blocked. Thus, the sample will appear much brighter in color compared to the surrounding area with no sample. In this dissertation, most of the images in the results section chapters 3, 4 and 5 were taken through bright field image and then followed by performing a Selected Area Electron Diffraction (SAED), where diffraction patterns are obtained from electron beam elastically scattered by the sample lattice. By Bragg's law ($2dSin(\Theta)=\lambda$) and geometric relationship in the reciprocal space, the index of the diffraction spots can be calculated and compared with the published crystal index phase pattern. SAED can be used to examine the superlattice of a crystal or charge density wave with satellite

diffraction. The image mode can also be taken as High-resolution transmission electron microscopy (HRTEM), which allows for the imaging of atomic structure of a sample. HRTEM can be used to extensively study lattice imperfections such as atoms' dislocations, grain boundaries, twin boundaries, and surface characterizations for a 2D material, such as in Figure 2.10.

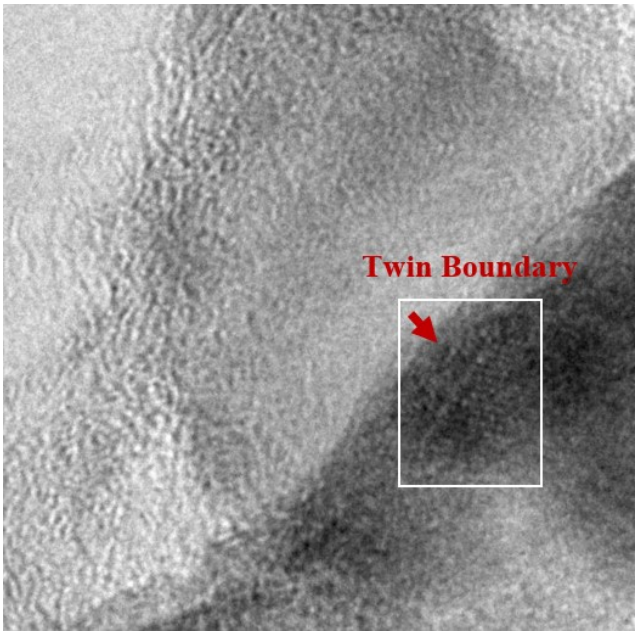

Figure 2.10 High-resolution transmission electron microscopy (HRTEM) on Bi_2Te_2Se single crystal. The white rectangular area with line overlapping indicates twin boundary.

2.3 Transport Measurement

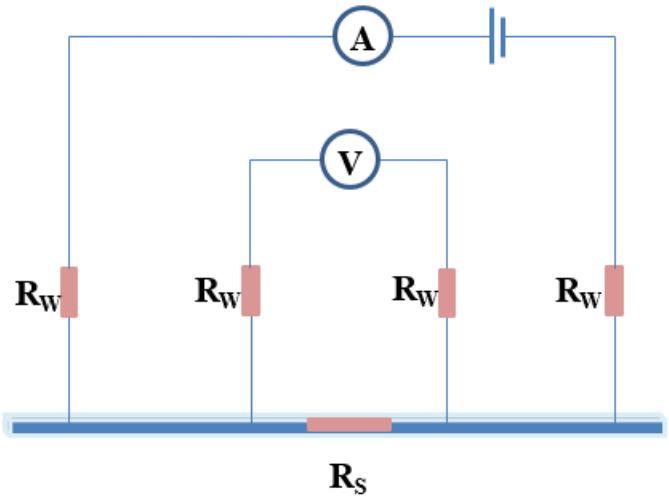

Figure 2.11 A simple diagram for Four-probe resistivity measurement, where R_w represents resistance from wires and contacts and R_s is the sample resistance.

2.3.1 Four-probe resistivity measurement

Resistivity vs temperature measurements were performed by a 4-probe inline method as shown in Figure 2.11. In the 4-probe measurement, a current will first be applied through the outer probes, after which voltage can be introduced through the inner probes, and sample resistance (R_s) can be measured. In this technique, no voltage drops through the wires (R_w) or contact resistance need to be considered because there is no current flowing through the loop measuring the voltage. Once sample dimensions are determined, the resistivity of the sample can be written as $\rho = \frac{R \times t \times w}{l}$ where R,t,w and l are the sample resistance, thickness, width and length.

To get the best measurement values, 4-probe method requires:

1. The resistivity of material must be uniform in the measurement area.

2. The probes must be attached to flat sample surface area to avoid electrical leakage.

4. The contacts' points much be in a straight line.

5. The contact points should be reasonably smaller than the distance between the probes to avoid short circuiting.

2.3.2 Physical Property Measurement System (PPMS)

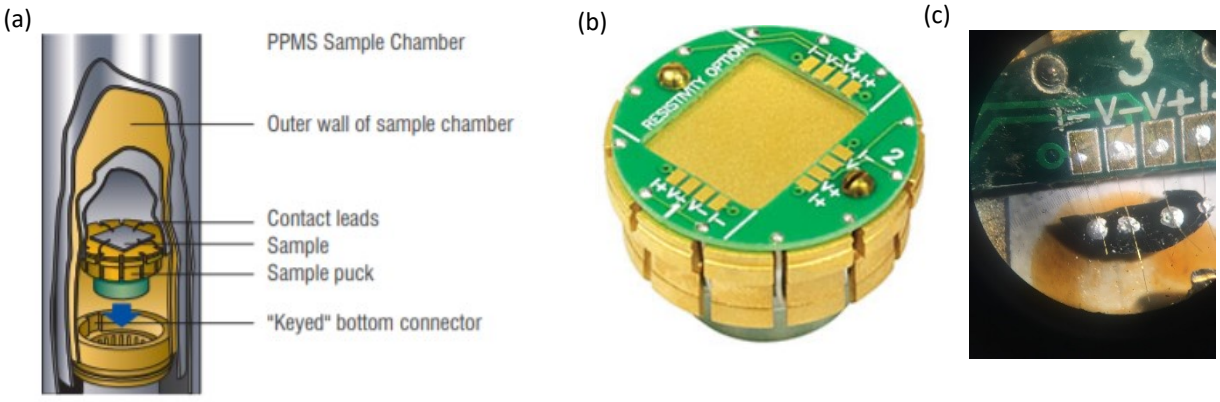

Figure 2.12 Physical Property Measurement System (PPMS), sample chamber (a) and sample puck (b), with maximum of three samples. (c) an example of four probe contacts on a sample and attached on channel 3.

Temperature and magnetic field dependent resistivity measurements were performed by the Physical Property Measurement System (PPMS) manufactured from Quantum Design. The sample environment controls include magnetic field up to 9T and temperature range of 0.3-350K. The base unit of PPMS consists of a cryostat with a superconducting magnet coil. The cryostat in PPMS includes superinsulation, Nitrogen jacket, vacuum space, and liquid helium bath. A local Helium recycler was connected with the cryostat in order to re-liquefy Helium gas in continuous mode. The PPMS sample mounting provided at the bottom of the sample chamber a 12-pin connector pre-wired to the system electronics, as shown in Figure 2.12 (a) where the bottom connector allows it to be plugged into the removable sample puck, as shown in Figure 2.12 (b).

Samples were mounted on a “Resistance Puck”, and each puck can be maximized to measure three samples. Figure 2.12 (c) displayed a four-probe contact on one of the samples which is placed on channel 3. Samples were mounted to the puck by using VGE7031 varnish at room temperature. Electrical connections (I-V connects) between sample and puck used 20 μm gold wire affixed to samples and were glued with silver paint. All wires connections were made under a microscope. With field dependent measurement, the magnetic field was applied along the c-axis of the crystal planes.

2.4 Raman Spectroscopy

2.4.1 Raman Spectroscopy principles

Raman Spectroscopy [114] is a spectroscopic technique which can be used to analyze the structure and the symmetry of molecules by detecting their vibrational modes. This phenomenon was first observed by C.Venkata Raman in Kolkata for which he received the Nobel Prize in 1930. In Raman Spectroscopy, a monochromatic light laser beam usually in the UV, IR, or visible range is used to irradiate the sample surface. Scattered light is associated with energy absorption by phonons as detected by a detector. Most of the scattered light is elastic scattering which is called Rayleigh scattering having the same frequency as incident light. A filter can be used to avoid detecting Rayleigh scattering light. Only 10^{-5} of the scattering light will have Raman inelastic scattering in which the lower vibration mode due to releasing phonon is called Stokes Scattering and higher vibration mode due to absorbing phonon is called anti-Stokes Scattering. Stokes Scattering is stronger in intensity compared to anti-Stokes scattering.

As originally theorized, the origin of Raman Spectra comes from the change of polarizability. The incident laser beam is an electromagnetic wave with a time varying electric field:

$\mathbf{E}=\mathbf{E}_0\cos(2\pi\gamma_0 t)$, (2.10)

Dipole moment for a diatomic molecule is:

$\mathbf{P}=\alpha\boldsymbol{E} = \alpha\mathbf{E}_0\cos(2\pi\Upsilon_0 t)$, (2.11)

If the molecule is vibrating with a frequency γ_m, the nuclear displacement can be written as:

$Q=Q_0\cos(2\pi\gamma_m t)$, (2.12)

For a small vibration, the polarizability α is a linear function with Q

$\alpha= \alpha_0 + \left(\frac{\partial\alpha}{\partial Q}\right)_0 Q + \ldots\ldots$ (2.13)

Thus,

$\mathbf{P}=\alpha\boldsymbol{E} =\alpha_0\,\mathbf{E}_0\cos(2\pi\gamma_0 t) + \left(\frac{\partial\alpha}{\partial Q}\right)_0 \boldsymbol{E}_0 Q_0\cos(2\pi\Upsilon_m t)\cos(2\pi\Upsilon_0 t)$, (2.14)

$= \alpha_0\,\mathbf{E}_0\cos(2\pi\Upsilon_0 t) + \frac{1}{2}\left(\frac{\partial\alpha}{\partial Q}\right)_0 \boldsymbol{E}_0 Q_0\{\cos2\pi(\Upsilon_0+\Upsilon_m)t + \cos2\pi(\Upsilon_0-\Upsilon_m)t\}.$

If $\left(\frac{\partial\alpha}{\partial Q}\right)_0 = 0$, it is only Rayleigh scattering without Raman active; If $\left(\frac{\partial\alpha}{\partial Q}\right)_0 \neq 0$, then it is Raman active, with $\gamma_0 + \gamma_m$ Stokes Scattering, $\gamma_0 - \gamma_m$ anti-Stokes Scattering.

Since the electric field takes into account x, y and z axis, the polarizability is written as a tensor:

$\alpha=\begin{pmatrix}\alpha_{xx} & \alpha_{xy} & \alpha_{xz}\\ \alpha_{yx} & \alpha_{yy} & \alpha_{yz}\\ \alpha_{zx} & \alpha_{zy} & \alpha_{zz}\end{pmatrix}$, (2.15)

If any one of the tensor components is changed during the vibration, then it is Raman active.

In Quantum Mechanics, the selection rule for polarizability can be written as:

$\alpha_{xx}=\int \varphi_{v'}^{*}(Q)\alpha_{xx}\varphi_{v''}(Q)dQ$, (2.16)

$\alpha_{xy}=\int \varphi_{v'}^{*}(Q)\alpha_{xy}\varphi_{v''}(Q)dQ$, (2.17)

……

Where, α_{xx}, α_{xy} ……are the components of the polarizability. $\varphi_{v'}$, $\varphi_{v''}$ are vibrational wavefunctions. v' and v'' are the vibrational quantum numbers before and after the transition. Q is the normal vibration coordinate of the normal vibration. If any of those α components is zero, then it is Raman active.

Group theory is used to determine the vibrational modes in Raman Spectroscopy. Molecules which have the same symmetry are classified into the same point group. The symmetry properties of each point group are laid out in a character table which contains all the symmetry elements (symmetry operations), along with a complete set of irreducible representation. From the irreducible representations we can subtract translational and rotational motion and then determine if the final vibrational modes are IR or Raman active. For a molecule in the condensed state, screw axis and glide plane will be considered which is more complicated when determining vibrational modes.

For simplicity, we consider a crystal in a linear chain with two atoms. In the first Brillouin Zone, it can be divided into the optical branch and the acoustic branch. The optical branch is at a higher frequency which is responsible for the Raman and IR vibrational modes and is proportional to the force constant, inversely proportional to the reduced mass. The acoustic branch is usually in the sonic or acoustical region.

Polarized Raman Spectra [114, 115] is important to be used to obtain the orientation of the sample, the symmetry properties of normal vibrations and their assignments. In the polarization, a linearly polarized light will be used to irradiate the sample and then collect the polarized scattering light. The configuration for Polarized Raman Spectra is written as a(bc)d, where a is the direction of the

incident laser, b is the direction of the polarization for the incident laser, c is the direction of the polarization for the scattering light, and d is the direction of the scattering light. In this work, Polarized Raman Spectra in the configuration of Z(XX)$\underline{Z}$ and Z(XY)$\underline{Z}$ were applied on the $Cu_xBi_2Te_2Se$ (x=0~0.5) samples.

2.4.2 Raman Modes for Bi_2X_3

For the pure Bi_2X_3 sample, each primitive cell contains 5 atoms. Thus, at the center of the Brillouin zone the total lattice dynamical modes are 15, during which 3 of them are acoustic modes and 12 of them are optical modes. According to group theory, the 12 optical modes contributes to $2A_g^1$ + $2E_g$ Raman active symmetry modes, and $2A_u^1$ + $2E_u$ Infrared-active symmetry modes [116], where g signifies Raman active and u signifies IR active. The Raman tensors for A_g^1 and E_g are as follows:

$$A_g^1 : \begin{pmatrix} a & 0 & 0 \\ 0 & a & 0 \\ 0 & 0 & a \end{pmatrix}, \tag{2.18}$$

$$E_g : \begin{pmatrix} C & 0 & 0 \\ 0 & -C & d \\ 0 & d & 0 \end{pmatrix}, \begin{pmatrix} 0 & -C & -d \\ -C & 0 & 0 \\ -d & 0 & 0 \end{pmatrix}. \tag{2.19}$$

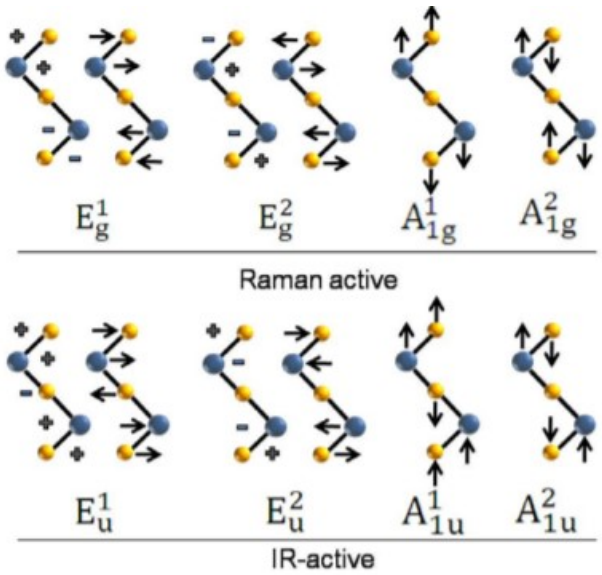

Figure 2.13 Raman Vibrational mode for Bi_2X_3, where Eg and Ag represent Raman active modes while Eu and Au represent IR-active modes (Adapted from Ref. [117]).

2.5 Crystal Growth Method

The commonly used methods for growing bulk Bi_2X_3 include Bridgman, Floating Zone and self-flux method [73, 118, 119]. Bridgman-Stockbarger method is a method of producing a crystal from a melt by progressively freezing it from one end to the other with growth rates in the range of 0.1-30 mmh^{-1}, where crystals can be either grown vertically or horizontally. Floating Zone method is implemented to move a liquid zone through the material. If properly seeded, a single crystal may form. Self-flux method is used to take stoichiometric amounts of the elements and fill in evacuated reaction vessels, after which they are heated until they melt. By the end, sample is slowly cooled to the desired temperature [120]. Most of the published metal intercalated Bi_2Se_3 topological superconductors were grown by a self-flux method followed by high temperature quenching, where it seems that high temperature quenching has an important impact on the electronic properties [96]. All the studied samples in this dissertation used the self-flux melting growing method, followed by high temperature quenching in cold or ice water

Chapter 3: Charge Density Wave in Bi_2Se_3 Single Crystal

This chapter reports the discovery of Charge Density Wave in self-doped Bi_2Se_3 crystal. The bulk crystal was grown using the self-flux method followed by quenching in ice-water. In this work, the existence of CDW was identified from crystal structure, electronic structure, and the local nuclear environment, utilizing a combination of X-ray diffraction, Selected Area Electron Diffraction, Transport measurement and Nuclear Magnetic Resonance measurement. X-ray diffraction on the powered Bi_2Se_3 shows an enlarged c-axis compared to earlier reports, which indicates Bi or Se self-doping. Room temperature SAED reveals a Periodical Lattice Distortion identified as diffused scattering in between the Bragg diffraction spots, which points to the Incommensurate Charge Density Wave (I-CDW) state driven by the distortion. Temperature dependent resistivity measurements show a metal-to-insulator transition at 140K, indicating the opening of an energy gap where the room temperature I-CDW locked into an ordered Charge Density Wave state. In ^{209}Bi NMR measurements, temperature dependent spin-relaxation (T_1) measurements further confirmed the CDW transition at 140K. With analysis of $1/T_1$ results, an energy gap ~10meV was revealed in both magnetic field H//c-axis and H⊥c-axis directions. Most of this work has been published in Li et al on arXiv [70].

3.1 Motivation and background for potential CDW in Bi_2Se_3

As discussed earlier in section 1.2.2 and 1.2.4.2, bulk Bi_2Se_3 crystal is a 3D Topological Insulator and belongs to the chalcogenide family with a 2D layered structure. The unique topological properties (such as time-reversal protected symmetry) with strong spin-orbital coupling and the layered crystal structure with weak van der Waals bonding makes Bi_2Se_3 a promising material for the production of topological superconductivities as well as some other intertwined electronic

ordered phases at the ground state, such as a Charge Density Wave.

Ideally, a Topological Insulator Bi_2Se_3 will host a single Dirac cone with a bulk energy gap (0.3 eV) [121]. If that is the case, the circular Fermi surface in an ideal TI will not allow the formation of Charge or Spin Density Wave order. However, many experiments have observed a lowering of the bulk conduction band due to natural electron doping from Se vacancies or Bi_{Se} antisite defects crossing the Fermi energy and allowing for bulk electron conduction [70-73]. Due to the native defects from the bulk states, an evolution of Fermi surface from circular to hexagonal geometry had been reported in naturally electron doped Bi_2Se_3 and observed by performing Angle-resolved Photoemission Spectroscopy (ARPES) measurements and an initial calculation[68, 91]. In the ARPES study, Kuroda et al [68] reported that the energy dispersion curves of the surface Brillouin zone along Γ-M direction is linear while along Γ-K direction is warped at small $k_{//}$, as well as an observation of anisotropic Fermi surface topology. Near the Dirac point, the constant energy contour is circular in shape; however, with the bulk conduction band enclosed inside the surface of constant energy, the constant energy starts to deform into a hexagon at above 200 meV. Similarly, an unconventional hexagonal warping term had been found in Bi_2Te_3 [91]. The calculation of surface band structure from $\mathbf{k}\cdot\mathbf{p}$ theory by Fu [91] stated that two flat segments of a hexagonal Fermi surface facing each other across $2\vec{k}_F$ along $\vec{\Gamma} - \vec{k}$ could lead to strong nesting. One of the possible outcomes of strong Fermi nesting is the appearance of Density Waves. Note, as a corollary, that some of the predictions and calculations refer to surface states.

By applying high pressure or intercalating foreign metals, Bi_2Se_3 also has been reported to host unconventional superconductivities or promising topological superconductivities [87-90,122]. Normally, unconventional superconductivity is driven by strong electron-electron correlations

[81]. Since Bi_2Se_3 is weak in *sp* electron coupling [100, 101], a phonon-medicated mechanism for its unconventional pairing has been recently proposed in this system. The first-principles linear response calculation on $Cu_xBi_2Se_3$ [100] and elastic neutron diffraction experiment on $Sr_{0.1}Bi_2Se_3$ [101] revealed that it was in fact the singular electron-phonon interaction brought by strong Fermi nesting at long wavelengths that plays the essential role in pseudo-triplet pairing with A_{2u} symmetry. In these studies, they also showed: (a) a phonon dispersion in Bi_2Se_3 is due to the motion of the Bi atoms along the z-direction, where phonon dispersion is also a direct effect of CDW; (b) with electron doping (such as intercalated with Cu or Sr), one of the phonon modes showed a large phonon linewidth, as well as a strong Fermi nesting and strong electron-coupling constant, which further led to crucial changes in electronic structure.

Both Density Wave Order and Superconductivity result in broken symmetry at the ground state. Charge density wave (CDW) [1-4] transition can be lifted by energy instability at the Fermi level and can further lead to an energy gap opening. The driving force behind such a CDW transition in low dimensional systems is mostly strong Fermi nesting and electron-phonon coupling. Thus, these earlier observations can help us explain why we can observe Charge density wave in naturally Bi self-doped Bi_2Se_3.

A few studies have hinted at the existence of CDWs in Cu-, Nb-Bi_2Se_3 [28, 29, 123], but so far have shown no result indicating a gap opening with temperature variation, signaling a CDW transition. Additionally, there have been no such reports in Bi_2Se_3. Here, I report for the first time that Bi_2Se_3 undergoes a transition to a CDW state at 140K. This work can help further understand

the origin of unconventional superconductivity in intercalated Bi_2Se_3 and potential topological superconductors in similar weakly correlated electron systems.

3.2 Experimental results

3.2.1 Periodic Lattice Distoration (PLD) in self-intercalated Bi_2Se_3

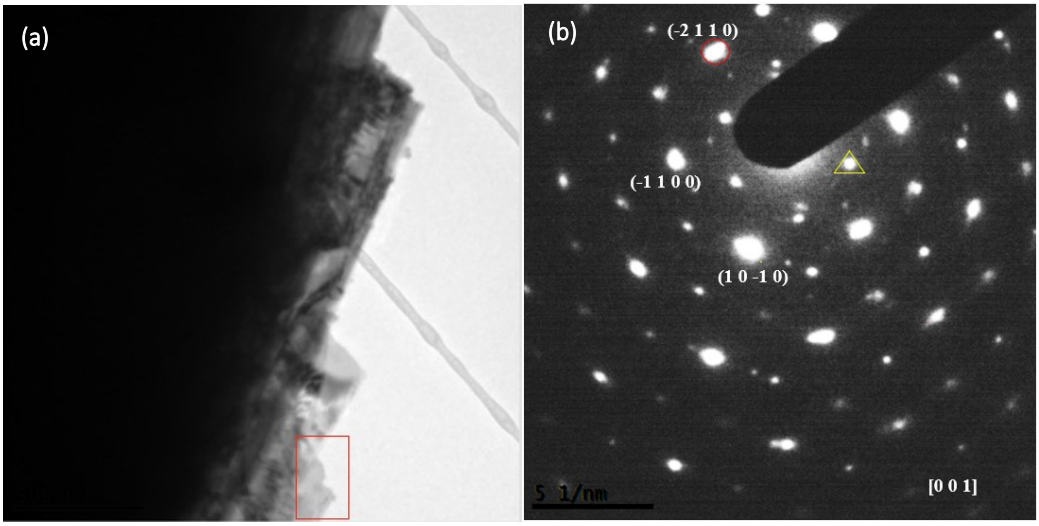

Figure 3.1 Transmission Electron Microscopy (TEM) and Selected Area Electron Diffraction (SAED) studies on Bi_2Se_3 single crystal at room temperature. **a** Bright field image of a piece from single crystal of Bi_2Se_3. The red box indicates the region on which SAED was performed. **b** Electron diffraction along [001] zone axis. Weak reflections of the type identified by a yellow triangle represent normally forbidden reflections from 3a/2 reflections in the [001] zone axis. Relatively strong reflections, circled in red, are identified reflections from the [001] zone axis.

Figure 3.1 displays bright field image (Figure 3.1 (a)) and Selected Area Electron Diffraction (Figure 3.1(b)) on single crystal of Bi_2Se_3, where measurements were taken at room temperature. Fig. 3.1(a) shows a bright field image of a single crystal with the red circle region indicating the area where the diffraction was taken for Figure 3.1(b). Figure 3.1(b) shows the results from SAED along [001] zone axis. The labeled Miller indices were the spots from the expected host-Bi_2Se_3

lattice with Bragg reflection spots along [001] direction. Inside of this strong Bragg hexagonal pattern there are six weaker reflection spots at reciprocal space positions of 2/3 (labeled in yellow triangle). For an ideal Bi_2Se_3 structure, the atom layers occupy the (001) planes in a cubic-like ABC stacking order symmetry (see Figure 1.5 in section 1.2.2), thus, the 2/3 spots are normally forbidden. This appearance of 2/3 positioned weak reflections indicates that ABC stacking faults. The same patterns have also been observed in zerovalent metal intercalated Bi_2Se--by Koski et al. and Wang et al. [28, 29],where they both explain that the intercalants at the van der Waals gap changed the energetics of interlayer stacking and thus changed the relative stability from rhombohedral structure to hexagonal structure resulting in a high intensity of stacking fault. In our sample, there is no foreign metal intercalation, hence the stacking fault is likely from Bi or Se self-doping. This is further confirmed by our X-ray Diffraction result.

Rietveld fitting of X-ray diffraction (XRD) on our Bi_2Se_3 samples reveal that the a=b axis value is 4.14±0.000242 Å, which matches with results from other reports. However, we find that our c-axis value is 28.66 ±0.001730Å. This is 0.02 Å higher than the 28.64 Å reported in most previous experiments on Bi_2Se_3. Previous authors have discussed that a longer c-axis, with values as high as 28.65 Å, can arise from the unintended intercalation of Bi into the van der Waals gap as a neutral metal Bi_2 layer [73]. Based on the higher c-axis value in our samples, and our evidence for stacking faults in SAED, we suggest that the van der Waals gaps in our Bi_2Se_3 crystals have zero-valent Bi or Se metal resulting from self-intercalation. See section 3.3.2.2 for more details.

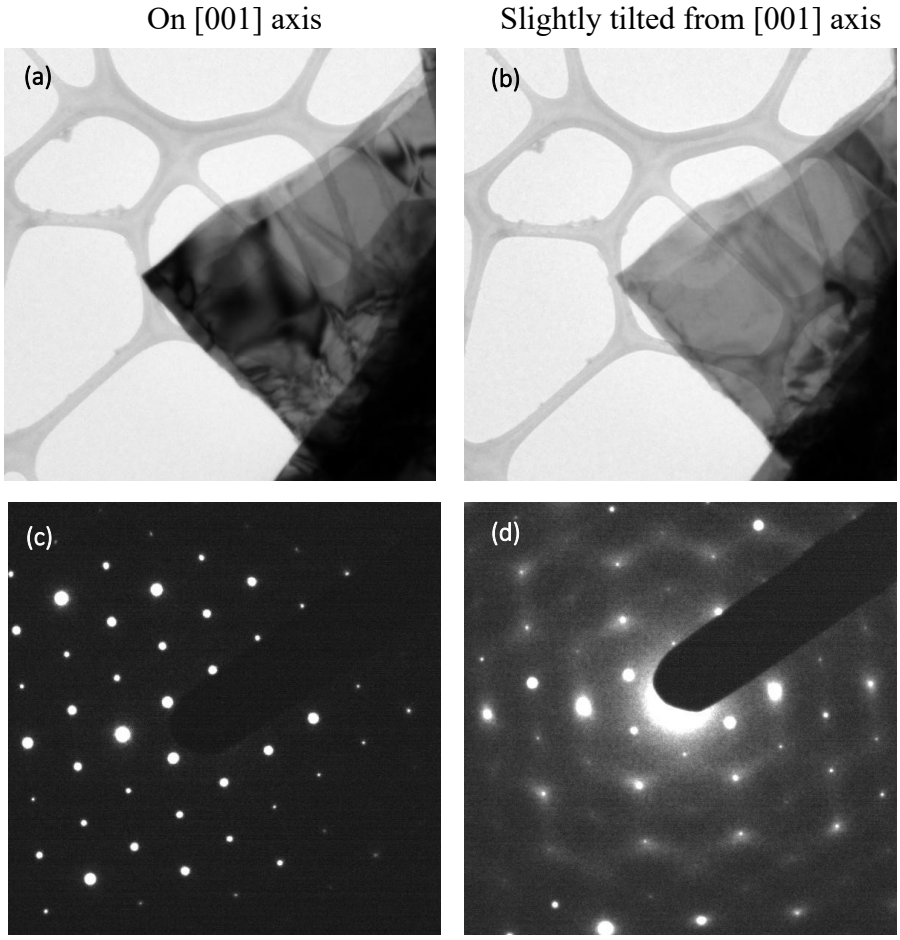

Figure 3.2 **a, b** Bright field TEM on a flake obtained from single crystal Bi_2Se_3. **c,d** Selected Area Electron Diffraction from the corresponding areas shown in (a) and (b). The images in (a) and (c) show results when the beam is on [001] axis. Images in (b) and (d) show off-axis electron diffraction, for which the sample was tilted slightly (less than 5 degrees) away from zone axis.

Figure 3.2 displays bright field TEM and SAED on flakes obtained from single crystal Bi_2Se_3. Figure 3.2 (a), (c) are bright field images taken on Bi_2Se_3 flake on the [001] zone axis. Figure 3.2 (b), (d) are taken from the same region of the flake, with the sample tilted slightly (less than 5 degrees) away from the zone axis. The images in Figure 3.2 (c), (d) correspond to the areas shown in Figure 3.2 (a), (b), respectively. By slightly tilting away from the [001] zone axis, as shown in Figure 3.2 (d), diffused set of lines can be observed in between the Bragg spots. These diffused

streaks suggest that the low intercalant concentration from self-doping is disordered and leads to a lattice distortion. From earlier SAED studies of the layered chalcogenide [17-21, 38, 76], this diffused intensity is most likely from the incommensurate charge density wave which is the precursor to charge density wave at lower temperatures. This phenomenon can be explained using Peierls theory that CDW is always accompanied by Periodic Lattice Distortion (PLD) [2,4]. At high temperatures, when the periodicity of CDW is not commensurate with the underlying crystal lattice and with many incommensurate spots, it will become diffused, forming a line between Bragg spots. Therefore, these diffused streaks are the result of Incommensurate Charge Density Wave (I-CDW) introduced by PLD [17-21]. A Commensurate CDW can be expected at lower temperatures.

To summarize, the crystal structure studies from XRD and SAED on Bi_2Se_3 reveal a native defect associated with unintentional self-doping of Bi or Se. Evidence of this can be seen as its lattice parameter c becomes larger and the ABC stacking order breaks down. Furthermore, when the crystal is slightly titled off [001] zone axis, PLD introduced stripes between diffraction spots, which is associated with an Incommensurate Charge Density (I-CDW). This occurrence of I-CDW at room temperature can be well explained by the locked-in CDW transition with an energy gap opening at 140K, which is observed in the transport measurement and ^{209}Bi NMR spin-lattice relaxation measurement shown as follows:

3.2.2 Transport measurement: metal-insulator-metal transtion at 140K

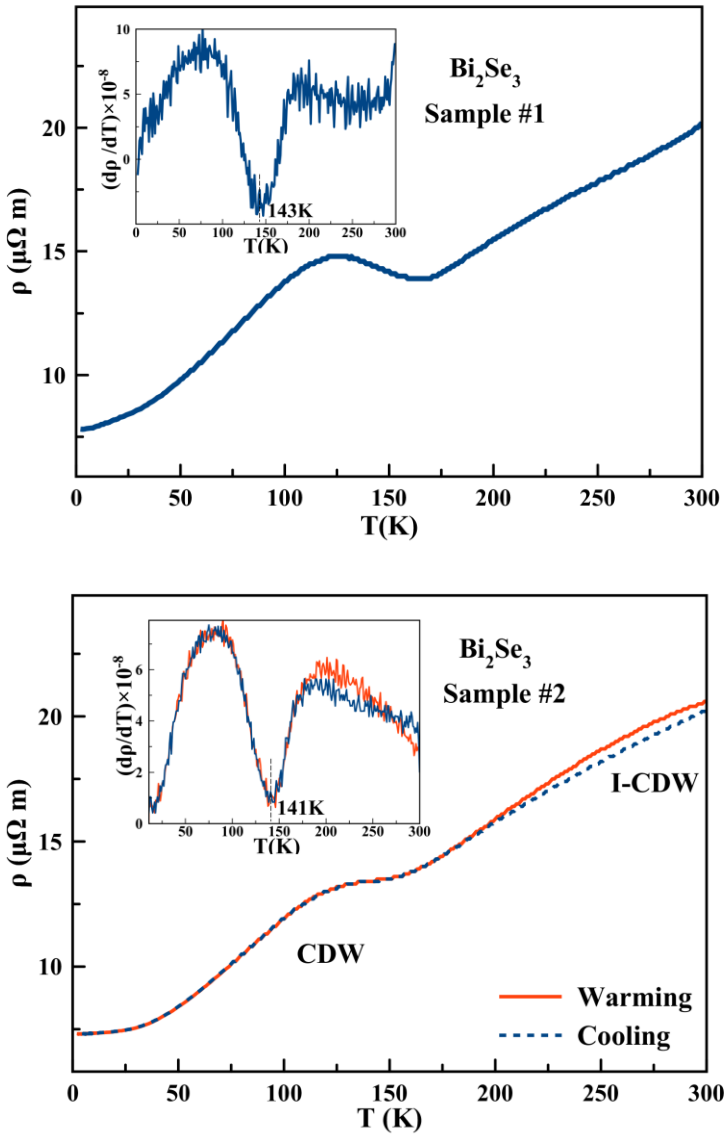

Figure 3.3 Resistivity of Bi_2Se_3 as a function of temperature for two different pieces, sample#1 and sample#2, measured in zero magnetic field with the electric field along the ab plane. (a) Measurement on sample #1 while cooling the sample from 300 K to 2 K; (b) Measurement on sample#2 for both cooling and heating. Insets for (a) and (b) are the plots of dρ/dT as a function of temperature to clarify the temperature values of the inflection points and the CDW transition temperature T_{CDW}.

Figure 3.3 shows results from four-probe DC resistivity measurements on the ab plane of Bi_2Se_3 single crystal, with temperatures ranging from 2 K to 300 K. To ensure reproducibility,

measurements were performed on several different pieces of the as-grown single crystal. Figure 3.3 (a) and (b) are the results from different pieces of the same crystal batch. The resistivity curves at zero field all show approximately linear (metallic) behavior from room temperature to around 140 K. A sharp phase transition upturn is observed with an onset temperature near 140 K, with resistivity initially increasing with decreasing temperature, followed by a return to metallic behavior at lower temperature. In Figure 3.3(a), with cooling, we see a rise in resistivity from ~1.38×10^{-5} Ωm to 1.47×10^{-5} Ωm; In Figure 3.3(b), we observe a rise ~1.31×10^{-5} Ωm to 1.36×10^{-5} Ωm, followed in both cases by a return to metallic behavior with decreasing temperature. Insets to Figures 3.3 (a) and (b) show dρ/dT as a function of temperature, clarifying the inflection point and onset near 140K. This transition behavior indicates a gap opening at the Fermi level upon cooling corresponding to a CDW phase transition [54]. Heating and cooling cycles were performed on the second piece of Bi_2Se_3, as shown in Figure 3.3 (b). No clear thermal hysteresis behavior was observed at the onset transition temperature 140K, indicating that this transition is possibly of unconventional second order [26]. However, a thermal hysteresis from heating and cooling in resistivity above 200K (shown as solid blue line and dashed red line) was observed, which corresponds to a first order transition, in which the onset transition is possibly above room temperature. This agrees with the earlier I-CDW state observed from room temperature SAED. Conventionally, a normal phase to I-CDW phase transition usually is second order and I-CDW phase to CDW phase transition is first order, with signature of thermal hysteresis in the first order. However, in some unconventional cases the picture can be opposite [26], as is in our sample. The reason behind this is not very clear, but it could be from the same origin as earlier discussed phonon-medicated unconventional superconductivity of Cu-, Sr intercalated Bi_2Se_3 [100, 101].

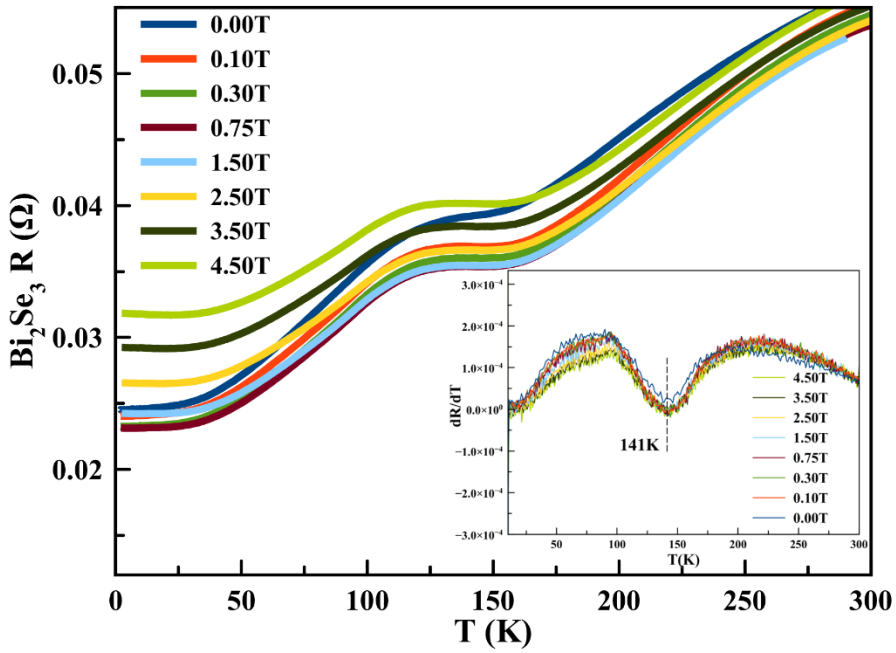

Figure 3.4 Resistivity of sample #2 Bi_2Se_3 as a function of temperature, with applying various magnetic fields along c axis (Magnetic field B=0.00 T, 0.10 T, 0.30 T, 0.75 T, 1.50 T, 2.50 T, 3.50 T and 4.50T)

To further examine the CDW transition behavior at 140K, constant magnetic fields were also applied along the c-axis of the sample #2 Bi_2Se_3 crystal. The results are displayed in Figure 3.4, where the inset shows dρ/dT as a function of temperature, where under different magnetic fields (0.00T to 4.5T), no apparent shift for CDW transition was seen. This result agrees with the one obtained for an unconventional CDW in $La_3Co_4Sn_{13}$ [26] and our conclusion from Figure 3.3. It is also consistent with our NMR spin-lattice relaxation measurement result observing the same 140K transition when magnetic field is applied at 9.86T.

3.2.3 ^{209}Bi NMR: Spin-lattice relaxation ($1/T_1$) anomaly at 140K and 200K

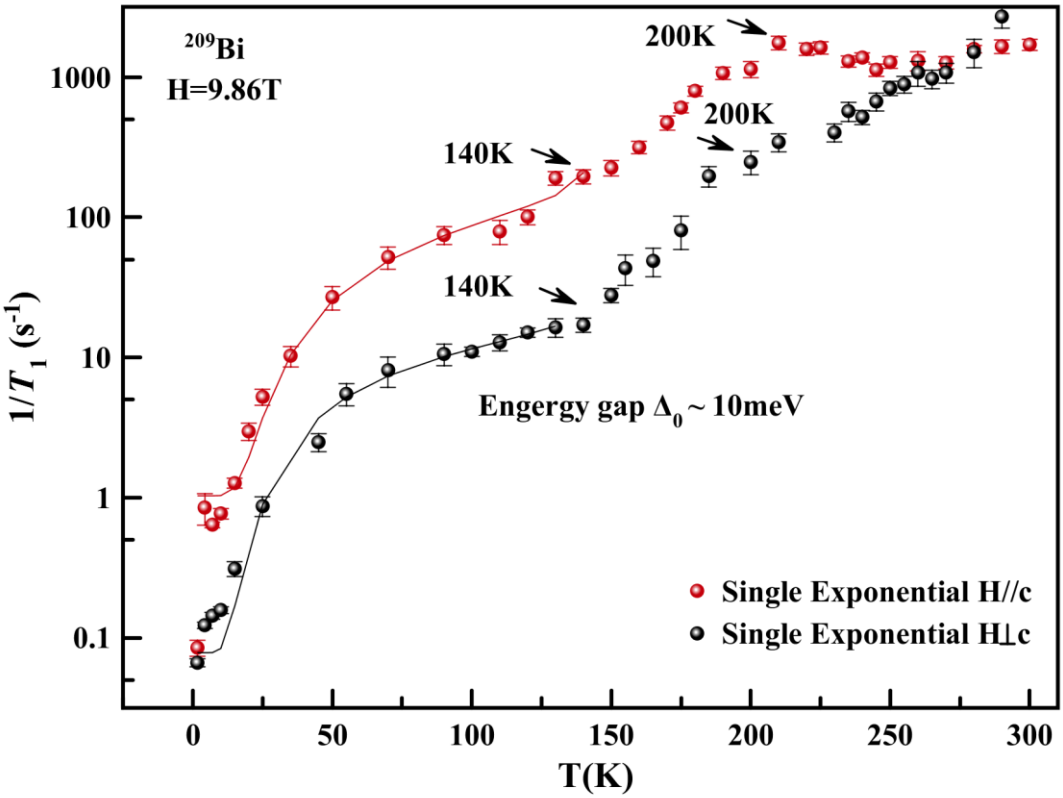

Figure 3.5 Spin-lattice relaxation rate ($1/T_1$) shown with temperature T varying between 1.6K and 300K with applied magnetic field directions: H // c-axis (red solid ball) and H ⊥ c-axis (black solid ball). Arrows indicate possible transitions at 140K and 200K in each direction, where the 140K is the Commensurate CDW transition temperature. Solid lines are fits to a temperature-dependent CDW energy gap, with gap value ~10meV.

In order to provide a microscopic information about the nature of these transitions we performed NMR relaxation measurements. The nuclear spin-lattice relaxation rate $1/T_1$ measures the recovery of the longitudinal nuclear magnetization following an external perturbation such as an RF field. Figure 3.5 display the temperature dependence of $1/T_1$ of the central $\langle \pm 1/2| \leftrightarrow |\mp 1/2\rangle$ transition of the ^{209}Bi nuclei, with temperature varying from 1.6K to 300K, and with the external magnetic field H = 9.86T applied in two orientations, H//c-axis and H ⊥ c-axis. It is clear that the spin-lattice

relaxation rate $1/T_1$ for both field orientations follow similar behavior as a function of temperature. Although the relaxation rates for H//c are about an order of magnitude longer when compared to H ⊥ c, they approach nearly the same value at room temperature.

Depending on the initial set-up of the pulse sequence, M (t) can be either fitted by a master equation or a stretched exponential equation [125,126]. The master equation assumes the saturation is only set on the central transition, but there's still contributions from satellite transitions to the relaxation. However, the stretched exponential equation is under the consideration of saturating all transitions simultaneously (such as we set for the pulse sequence trains), then the characteristic recovery will be governed by all the transitions simultaneously relaxing. This will give us a single exponential form. Also, depending on which equation is used for the fit, the results for T_1 are different in magnitude (usually Master result is 50 times of exponential fit), see the discussion in Nisson et al.[127] Thus, based on our experimental setup with looped pulse train sequence, we chose the stretched exponential method (see methods). However, we find that the fits with and without the stretch parameter gives similar T_1 results, giving stretched component β values close to 1. Same analysis was also used in Guehne et al [128] for Bi_2Se_3. The results of this fit are shown in Figure 3.5 for both orientations of the magnetic field, where we see two obvious slope changes: at 140K and at 200K, indicated by arrows. The 140K anomaly coincides with the metal-insulator-metal transition observed in our resistivity measurements which we interpreted earlier as a transition to a commensurate CDW state. The anomaly seen at 200K exhibits a weak anisotropy with applied magnetic field.

3.3 Discussion

3.3.1 Transition near 200K

There are two possible mechanisms for the appearance of the 200K transition. One is related to the Debye temperature at $\Theta_D \approx 182$K for Bi_2Se_3 [129]. The other is the mechanism from I-CDW [130]. Given that the behavior of $1/T_1$ is dependent upon the details of the high temperature phonon spectrum, one would expect it to behave differently above and below the Debye temperature. Thus, it is plausible that the transition observed around 200K in Figure 3.5 is due to changes in the phonon spectrum across Θ_D. However, the anisotropy in this transition with the direction of applied magnetic field, H//c and H⊥c would point toward a different mechanism, as is clear from Figure 3.5.

In Figure 3.3 (b), we observe a thermal hysteresis in resistivity above 182K. Whereas a transition related with Θ_D would yield a change in slope of resistivity, it is hard to explain the thermal hysteresis in resistivity, for T > 182K, based purely on a Debye temperature transition. On the other hand, a hysteresis between heating and cooling is often observed below a first-order I-CDW to CDW transition. The absence of a thermal hysteresis, as in the case of $Lu_5Ir_4Si_{10}$, often leads to speculation that the transition either is of second order or has some "unconventional" origin [26, 131]. In our case, as shown in Figure 3.3 (b), the resistivity below 140K does not display a thermal hysteresis. This indicates that the 140K transition is likely a second-order CDW transition. If this reasoning is correct, the 200K transition is a first-order transition. Additional work is needed in order to differentiate one mechanism from the other.

Note in Figure 3.5 that the $1/T_1$ data for both orientations follow similar behavior as a function of temperature, except that the relaxation rates for H//c are about an order of magnitude faster compared to H ⊥ c. However, they approach almost the same value at room temperature. Above 200K, the temperature behavior differs: the $1/T_1$ value remains constant from room temperature to 200K for the parallel case while it precipitously drops for the perpendicular case. This would imply a constant relaxation mechanism that only exists in the parallel direction and is weakly dependent on temperature, while in the perpendicular direction, this mechanism monotonically diminishes until the temperature reaches 200K. The origin of this mechanism is not clear but it may be related to the topological nature of this family of systems which suppresses the relaxation channel when the field is applied parallel to the plane of the layers [132, 133].

Comparing our results to the earlier results for $1/T_1$ as Ref [130], the peak feature of $1/T_1$ in the magnetic field parallel to crystal c-axis direction can be linked to the I-CDW transition. The driven force of this behavior is possibly from the interaction of quadrupolar relaxation with lattice. Due to defects pinning on the charge order, the PLD with diffused scattering was started to be seen in room temperature SAED but the I-CDW transition temperature is observed at 200K in NMR (some papers call this is Nearly Commensurate CDW transition) [134]. Native defects (Bi/Se self-doped into Bi_2Se_3's van der Waals gap) has caused a Lattice Distortion along *[001]* zone axis as had been discussed in our earlier room temperature SAED, in turn, this distortion can further lead to a fluctuation in quadrupolar relaxation. This transition at 200K can also help to explain the anomalous behavior of $1/T_1$ between the two magnetic field orientations, where it is possible that the Fermis surface only opened small segments, and thus shows stronger signal in a particular direction [130].

3.3.2 Transition near 140 K

Nuclear relaxation measurements, in Figure 3.5, together with resistivity measurements in Figure3.3(a) and Figure 3.4 clearly reveal a transition near 140K. We interpret this as a transition to a CDW state below 140K. We support this conclusion from electronic diffraction measurements at room temperature (Figure 3.1and Figure 3.2), which reveal the presence of a periodic lattice distortion (PLD) combined with diffuse scattering in off-axis diffraction, suggesting the presence of an incommensurate charge density wave (I-CDW) state already at higher temperature. Interestingly, T_1 anomalies have been associated with CDW transition in layered systems [135-138]. With temperature lowered down to T_{CDW}, more segments of the Fermi surface are opened, and thus we can observe the 140K transition in both magnetic field directions for $1/T_1$ measurements. According to Periels theory, this energy gap originates from a strong coupling between the electrons near the Fermi level and the phonons, with "nesting" wavevector at $Q=2k_F$. In the NMR microscope point of view, this $1/T_1$ anomaly is possibly driven by the change of lattice and phonon spectrum that is caused by self-doping [case (c) in Nission's paper [127]]. Thus, the quadrupolar relaxation correlates with lattice imperfection along the z-axis direction started from or above room temperature with first anomaly transition at 200K and reached to the locked-in CDW state at 140K.

Below 140K, the relaxation rate is determined by the CDW gap, as following [2, 139]:

$$1/T_1 = a \exp[-\Delta(T)/T] + c, \tag{3.1}$$

where we shall use the form of T-dependent BCS gap equation

$$\Delta(T) = \Delta_0 \tanh\left(1.74\sqrt{\frac{T_c}{T} - 1}\right), \tag{3.2}$$

Here, $T_C = T_{CDW}$ is the CDW transition temperature, a and c are fitting constants. The fit (Figure 3.5) yields a zero-temperature energy gap of Δ_0=10± 2meV in both directions of applied field. Normally, in the weak coupling limit, coupling constant λ is close to 1.7 [2]. We estimate our coupling constant $\lambda=\Delta_0/k_B T_{CDW}$=0.7 (where T_{CDW}=140K and k_B is the Boltzmann constant) which is close to the weak coupling limit. Further experiments on superconducting Bi_2Se_3, intercalated with Cu, Nb, or Sr, can reveal the full extent of whether the electron-phonon coupling in the CDW ground state assists is in any way related with the electron-phonon coupling of the superconducting state [100, 101, 140].

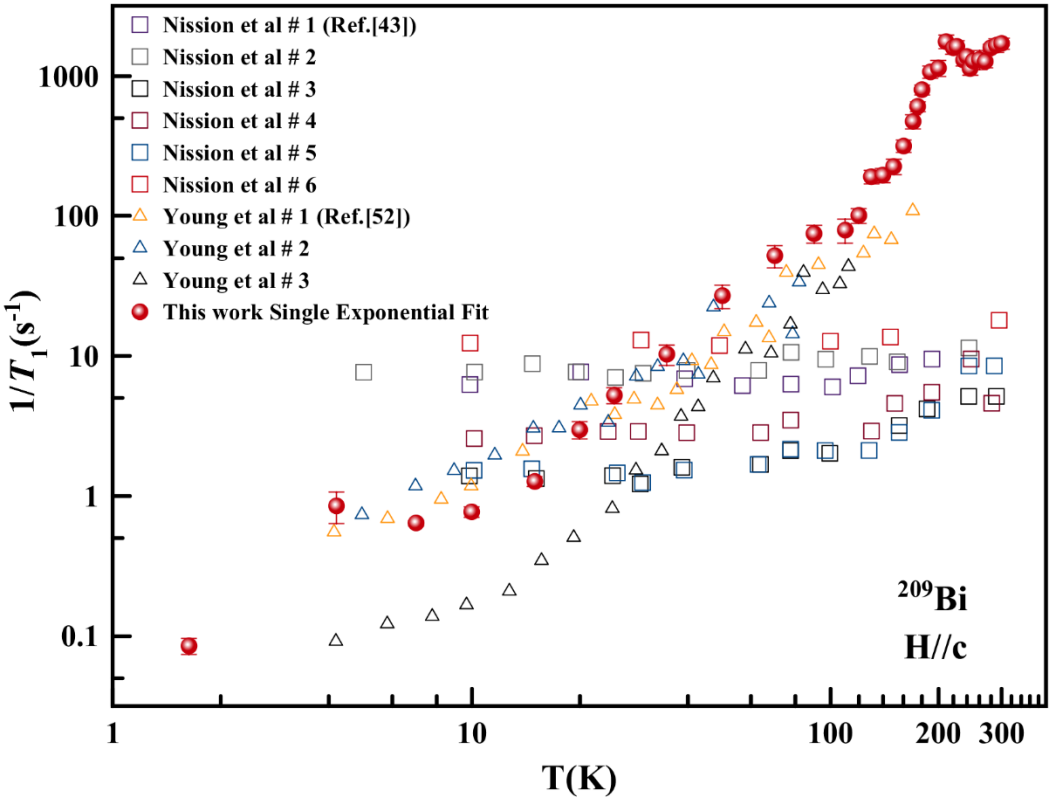

Figure 3.6 Comparison of Spin-lattice relaxation rates of ^{209}Bi versus temperature from earlier published papers to our result in the magnetic field H//c direction. The open data points are reproduced from Ref. [127] (square shapes) and Ref. [129] (triangle shapes). Solid data points are our results same as displayed in Figure 3.5 H//c direction data, with single exponential fit.

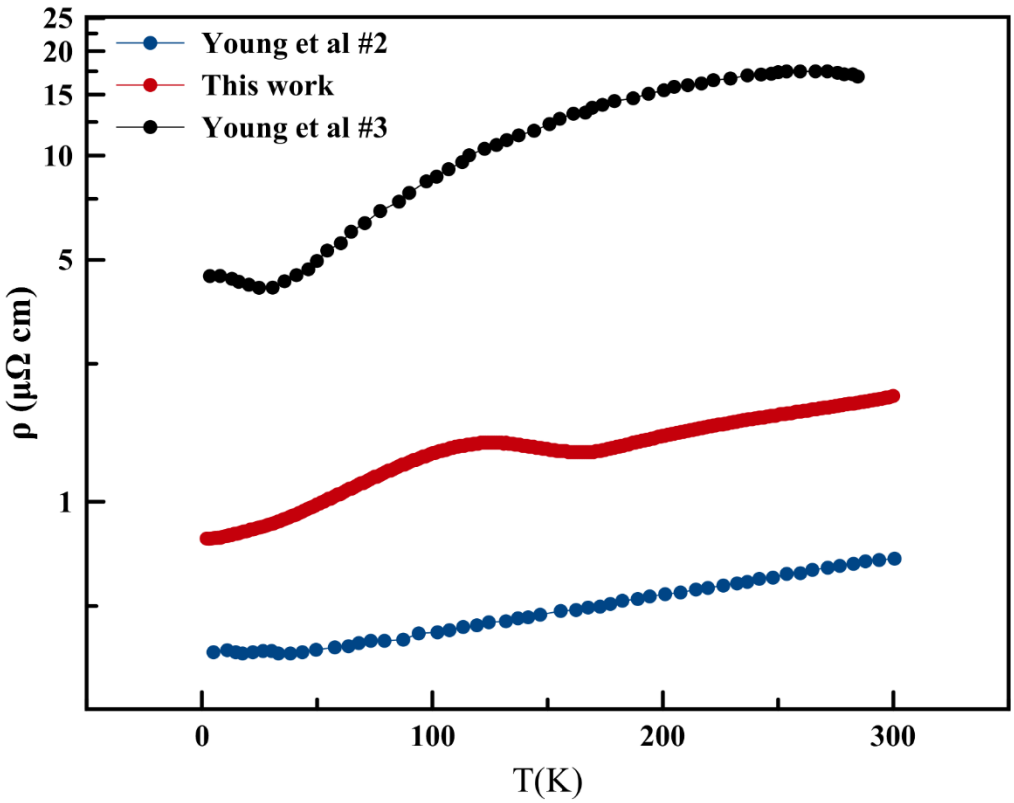

Figure 3.7 Comparison of resistivity vs temperature results from our transport measurement (red) and from Ref.[52] Young et al (bule and black).

Previous relaxation measurements show a large variation in magnitude and temperature dependences across samples prepared using various methods (refs. [127, 129]). These variations were attributed in part to the level of defects associated with Se-vacancies which could shift the Fermi level by partially occupying the conduction band. Unlike previous studies, our data shows a very strong temperature dependence from 1.6 to 300K, spanning almost 4 orders of magnitude for H⊥c. Figure 3.6 displays a comparison of our results from temperature dependent $1/T_1$ data with earlier references from Young et al [129] and Nission et al [127]. Our results in low-

temperature behavior (1.6K to 15K) is comparable to that of sample #2 of Ref. [129] which the authors identify the sample with higher carrier concentration, with a $1/T_1$ proportional to T. Further, comparison of the resistivity data (Figure 3.7-our sample to Young's sample #2 and #3) shows that our sample has slightly fewer carriers than their sample #2 but is far from insulating, suggesting that the Fermi level in our sample sits lower in the conduction band. This is consistent with a narrower NMR spectrum, and a comparatively smaller Knight shift to Young's sample #2 (K_{iso} ~0.4% vs. Young's #2 ~0.65% and Young's #3 ~0.34% at 4.2K). An argument can be made that it is possible that in some direction of the reciprocal space that half band-filling, essential for Peierls transition, has been serendipitously achieved in our sample by appropriate doping through Se-vacancies leading to the formation of CDW in our sample. The fact that $1/T_1$ is dependent on electronic mobility, is consistent with our earlier discussion for 140K transition.

3.3.3 The origin of CDW order in Bi_2Se_3

3.3.3.1 Doping effects on Fermiology and CDW dimensionality

As introduced in section 3.1, topological insulators such as Bi_2Se_3 and Bi_2Te_3 with native defects are expected to host density wave order due to their complex fermiology – in particular, strong Fermi surface nesting [68, 103], which is possibly contributed by Fermi surface deformation. Shubnikov-de Haas measurements on Nb intercalated Bi_2Se_3 have revealed evidence for a small extra Fermi pocket besides the main Fermi surface of Bi_2Se_3 [123]. Additionally, a first-principles linear response calculation for Cu intercalated Bi_2Se_3 has revealed a 'prism-like' fermi pocket at the Γ point, with opportunities for strong Fermi nesting [100]. Since Fermi nesting is the driving

force behind CDW in low dimensional chalcogenides, a CDW transition should not be overly surprising in theory.

As described by Zhu et al [33, 34], the origin of CDW is also strongly related to dimensionality. They describe "Type-I" CDWs as quasi-1D systems with origins in traditional Peierls' instability and Fermi Surface Nesting (FSN), with lattice distortion being a consequence of the electronic disturbance, as found in linear-chain compounds. Zhu et al assert that "Type-II" CDWs, in contrast, are driven by electron-phonon coupling (EPC) and not by FSN. In such case, the electronic and lattice instabilities are intimately tied to each other with a phonon mode at q_{CDW} which goes to zero at the transition temperature T_{CDW}. This second type does not require a metal-insulator transition associated with T_{CDW}. They further describe a "Type-III" case, where a charge modulation is found without the driving force of an FSN or EPC, and where the driving force is possibly electron correlations.

Most CDW occurs in quasi-1D or quasi-2D; Since *sp* electrons in Bi_2Se_3 are weakly correlated, our current understanding of CDW does not include all the complexities involved in the 3D case, where electron correlations are thought to play a primary role [33,34]. In this context, it is instructive to further discuss the possible effect of intercalation on k_F anisotropy between k_z versus k_X, k_Y. Xiangang and Sergey [100] suggest that small changes in the position of Bi in the z-direction can modify the nesting vector $X(q)=\Sigma\delta(\varepsilon_k)\delta(\varepsilon_{k+q})$, where, ε_k *and* ε_{k+q} are the energy of states at/near the Fermi level. This nesting vector is largest for wavevector q along the Γ_Z direction, when q is close to zero. This can lead to strong Fermi nesting, and strong electron-phonon coupling. Displacement along <001> at small *qs* (i.e., small momenta) breaks spatial inversion symmetry, lifts double degeneracy, and leads to a large electron-phonon coupling matrix

element along this direction close to zone center. Further calculations by Xiangang and Sergey[100] and neutron scattering experiments by J. Wang, et al [101] show broad phonon linewidths for small *qs*, which could dominate electron-phonon coupling. Based on these arguments, we tentatively pose the possibility of the presence of a quasi-1D Peierls-type transition in the z-direction of Bi_2Se_3.

3.3.3.2 Materials considerations

As previously discussed (section 3.1), the unintentional doping from native defects or intentional intercalating metals into Bi_2Se_3 has an important effect on the Fermiology as regards CDW order. However, it is also important to emphasize that the crystal growth condition (such as annealing and quenching condition) may cause differences in the defects and intercalation level in the crystal structure, which would then eventually cause a significant change in the electronic state.

The crystals discussed here were grown using a standard self-flux method, and a quenching temperature of 650C. The ideal topological insulator, Bi_2Se_3, has separate bulk and surface states. However, experimentally, intrinsic defects and disorder can be widely found in Bi_2Se_3 and intercalated/electron-doped Bi_2Se_3 [70-73]. Schneeloch et al [96] used different growth conditions to grow Cu doped Bi_2Se_3 superconductor and reported that high temperature quenching (above 560C) is essential for superconductivity, especially superconductivity with high diamagnetic shielding fraction. Other growth conditions either cause no SC or weak diamagnetic shielding fraction. This is also our observation [141] in Cu-Bi_2Se_3. Schneeloch et al suggest that the quenching process either helps maintain a primary intercalated phase or a secondary phase responsible for superconductivity. Huang et al show that high annealing temperature (~600C) can cause intercalation of Bi_2 in Bi_2Se_3 [73]. Our results indicate that high-temperature quenching

(from above 650C) leads to strong lattice and charge order, and to interesting electronic ground states such as a CDW or superconductivity.

X-ray diffraction (XRD) on powdered samples reveals that the a-axis value of our single crystal Bi_2Se_3 agrees with those of most other reports, but that the c-axis, at 28.66 Å, is 0.02 Å higher than the 28.64 Å reported in most previous reports on Bi_2Se_3 [73, 142, 143]. Huang et al assert that a longer c-axis arises from unintentionally doped Bi-rich flux growth of Bi_2Se_3 where Bi forms a neutral metal Bi_2 layer intercalated into the van der Waals gap [73]. They also show that crystals with patches of intercalated Bi show high c-axis values of up to 28.65 Å, close to the c-axis value of 28.66 Å obtained from our Rietveld refinement. XRD results on our Bi_2Se_3 single crystals show no signs of the formation of metastable phases of staged $(Bi2)_m(Bi2\ Se3\ )_n$. The solidification temperature of Bi_2Se_3 (705 C) is higher than the melting point of both pure Bi (271.4 C) and pure Se (220 C). Additionally, Se is a vapor above 685 C, which is below the solidification temperature of Bi_2Se_3. Consequently, the stoichiometry of Bi_2Se_3 forming at the liquid-vapor interface can be highly dependent upon the vapor pressure of Se at 705 C. For high annealing temperature (around 600 C), partial decomposition might occur. Huang presumes that this is due to a large number of Se vacancies created in an evacuated environment, resulting in liquid Bi in the flux ending up in the van der Waals gaps rather than incorporating into a Bi-Se quintuple layer containing Se vacancies. Our crystals, quenched at 650 C (above the high annealing temperature of 600 C that Haung claims results in Se vacancies) could lead to Se vacancies and intercalated Bi. We surmise that, as there is not enough excess Bi to form the metastable phase of staged $(Bi_2)_m(Bi_2Se_3)_n$, excess Bismuth in our crystals forms randomly distributed Bi_2 inter-layers in the crystal. The resulting Bi-chains could help form a quasi-1D Peierls-type transition or a quasi-2D type CDW

[50,55,65,70, 76]. In summary, specific growth conditions can drive the observation of a CDW or superconductivity in Bi_2Se_3. Further work is needed in this direction.

3.4 Experimental Method

3.4.1 Crystal Synthesis

Single crystals of Bi_2Se_3 were prepared by melting high purity (99.999%) powders of Bi and Se. Stoichiometric mixtures of 2.5 g were vacuum sealed in high-quality quartz tubes after being weighed and sealed in an inert glove box, taking extreme care to never allow air exposure. The mixtures sealed in quartz tubes were heated up to 850 C and maintained as such for 20 hours. They were then cooled to 650 C at 0.1 C/min, followed by quenching in ice water from its scorching high temperature. This yielded large, shiny single crystals which were easily cleaved along the ab plane.

3.4.2 Measurements and related analysis method

Powder X- ray diffraction data were collected from pieces of single crystals powdered inside an inert glove box. Rietveld refinement was performed using GSAS (General Structure Analysis System) and the EXPGUI interface. Selected Area Electron Diffraction (SAED) was performed at room temperature with a Hitachi H-9000NAR high-resolution transmission electron microscope (HRTEM) operated at 300 kV. Four-probe resistivity measurements were performed at varying temperatures and magnetic fields using a Quantum Design Physical Property Measurement System (PPMS).

Pulsed ^{209}Bi NMR (Nuclear Magnetic Resonance) measurements were performed on a Bi_2Se_3 single crystal, with crystal dimensions ~0.94 x 0.58 x 0.41 cm, which was placed inside a home-

built probe in an 11-Tesla Helium cryostat. The single crystal of Bi_2Se_3 was studied with the magnetic field oriented in two directions, H⊥c and H//c. Spin-echo signals for ^{209}Bi NMR spectra were processed using the summed Fourier transform method, with field swept from 9.7T to 10.5T. Spin-lattice relaxation time T_1 measurements in both H//C and H⊥C directions were performed at stabilized temperature points ranging from 1.6K to 300K. We employed a train of RF pulses on the central transition to saturate the magnetization followed by variable delays and integration of spin-echoes to map the magnetization recovery.

The magnetization recovery $M(t)$ was fitted with a stretched single exponential, appropriate for the initial condition where the quadrupolar satellites are completely saturated: (see Ref. [125])

$$M(t) = M_\infty \left[1 - e^{-(t/T_1)^\beta}\right] \tag{3.3}$$

where the parameter β allows for a distribution of T_1.

3.5 Conclusion

To conclude, we have presented evidence for the first direct experimental observation of charge density wave (CDW) order in Bi_2Se_3. Diffuse streaks in SAED measurements indicate the presence of an incommensurate periodic lattice distortion at room temperature, reminiscent of an incommensurate charge density wave (I-CDW). A metal to insulator transition at 140K in resistivity measurements indicates the opening of a CDW-like energy gap. NMR spin-lattice relaxation rate $1/T_1$ measurements further confirm the presence of the 140K transition with an energy gap of about 10meV. Using this, together with thermal hysteresis studies of resistivity, we conclude that Bi_2Se_3 displays an unconventional second-order quasi-1D CDW transition temperature at 140K. NMR also reveals another transition near 200K. This 200K transition shows

an anisotropy with the direction of applied magnetic field, H//c and H⊥c. We also discuss how growth methods could promote the formation of a CDW. We suggest that strongly correlated ground states are present in Bi_2Se_3 crystals grown with a high annealing and quenching temperature. In this scenario, the higher temperature growth conditions resulted in self-intercalation of Bi into Bi_2Se_3, leading to a Periodic Lattice Distortion and producing, in turn, a Charge Density Wave transition. Thus, further studies are required in order to elucidate the dependence of electronic correlations on growth conditions, and to the occurrence of interesting ground states such as CDW and superconductivity.

Chapter 4: Charge Density Wave in Superconducting Nb-Bi_2Se_3

4.1 Motivation

This chapter reports the observation of charge density waves and superconductivity in Nb intercalated Bi_2Se_3. The interplay between charge density wave (CDW) order and superconductivity has been of great interest in Condensed Matter Physics [11-14], because both symmetry orders use electron-phonon/electron interactions and feature broken symmetries at the ground state. The underlying relationship (cooperate, compete, or simply coexist) between CDW and superconductivity has long been a topic of debate. Well-known systems which display both a CDW state and an unconventional superconducting state include several layered chalcogenides [41-46], where the fermiology plays an important role in the occurrence of these two states. Recent reports of intercalation in topological insulators such as Bi_2Se_3 (which also belongs to the class of chalcogenides) with Cu, Nb, and Sr, have revealed unconventional pairing and have been promoted as a source of potential topological superconductivity [87-89]. Earlier work from first principles electronic structure calculations, recently supported by neutron diffraction measurements, suggest that unconventional electron pairing in superconducting Cu- and Sr-intercalated Bi_2Se_3 might be driven by a singularity in electron-phonon interactions arising from strong Fermi Nesting at long wavelength, along Γ_z direction [100, 101]. By observing Strong Fermi Nesting and multiple Fermi pockets [102, 123], it is expected that charge density wave order can be searched for in the intercalated Bi_2Se_3 system, such as in $Nb_xBi_2Se_3$. Here, I discuss the observation of CDW and SC in $Nb_xBi_2Se_3$ from the change of crystal structure to the change of electronic structure by performing Selected Area Electron Diffraction, Transport measurements and local Nuclear Magnetic Resonance Measurements.

4.2 Experimental results and discussion

4.2.1 Crystal structure: PLD due to Nb intercalation

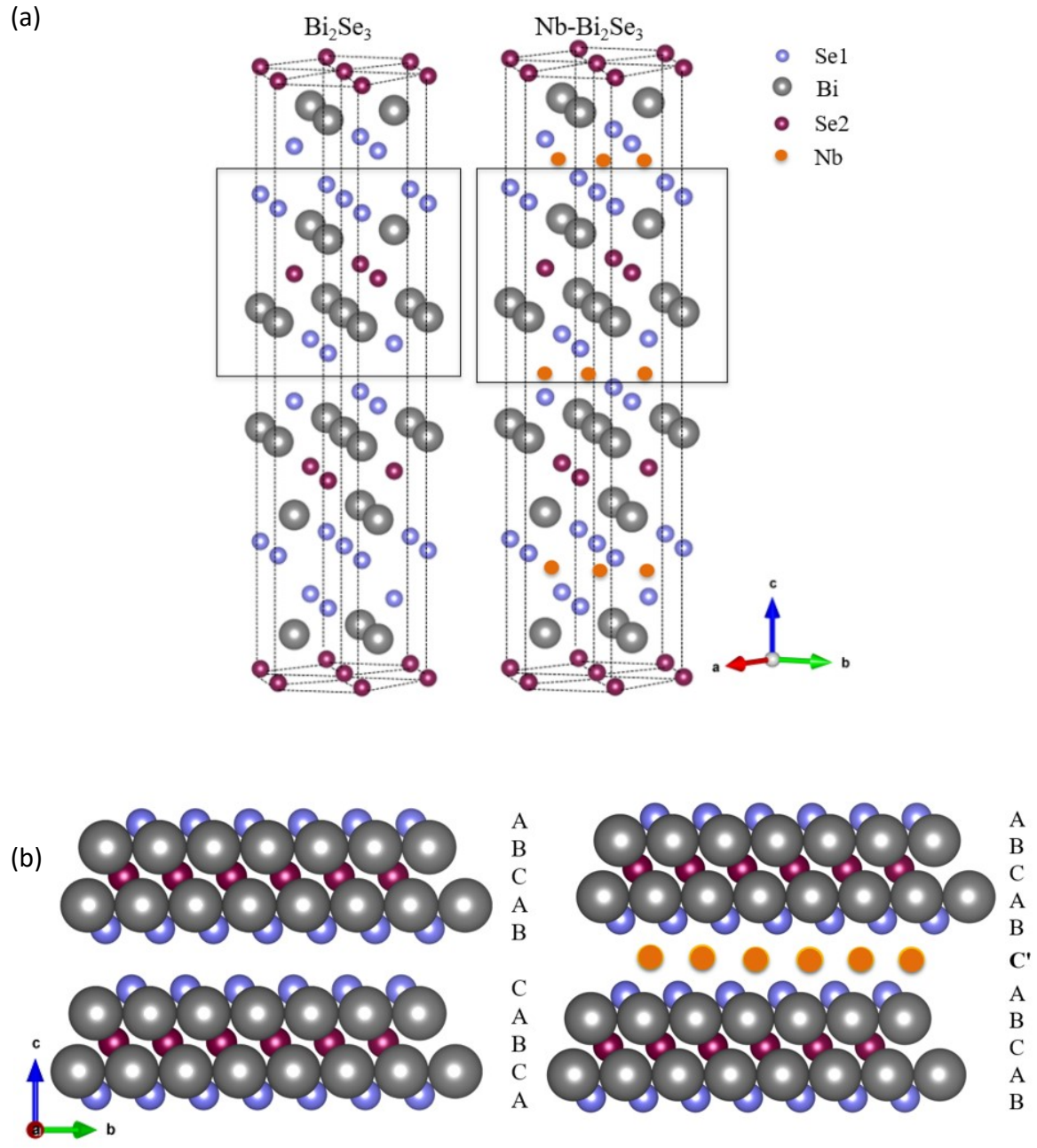

Figure 4.1 Crystal structure of $Nb_xBi_2Se_3$ and ABC stacking symmetry: (a) Crystal structures of Bi_2Se_3(left) and Nb intercalated Bi_2Se_3 (right). Inside the Quintuple Layer structure of Bi_2Se_3 (Square shape), blue solid ball represents Se1 (outer layer Se site), grey solid ball represents Bi, red solid ball Se2 (inter layer Se site) and in the case of $Nb_xBi_2Se_3$, orange ball represents

intercalated Nb. (b) ABC stacking along c-axis for Bi_2Se_3(left), with stacking order along c-axis as –A(Se1)–B(Bi)–C(Se2)–**A(Bi)–B(Se1)–C(Se1)–A(Bi)** –B(Se2)–C(Bi)–; while ABC stacking falls with Nb intercalated into van der Waals gap of Bi_2Se_3(right), where C'(Nb) breaks the original C(Se1) site, with c-axis now stacking as –A(Se1)–B(Bi)–C(Se2)–**A(Bi)–B(Se1)–A(Se1)–B(Bi) –** C(Se2)–A(Bi)–.

Figure 4.1 (a) displays the crystal structures of host Bi_2Se_3 (left) and Nb intercalated Bi_2Se_3 (right). Bulk host crystal Bi_2Se_3 belongs to D_{3d}^5 R$\underline{3}$m space group. The supercell of Bi_2Se_3 can be considered as having a hexagonal layered structure, with Quintuple layers (QL-Se1-Bi-Se2-Bi-Se1-) of atoms stacked along the trigonal axis. Inside of each Quintuple layer, Se has two possible positions, with Se1 representing the outer layer Se atoms, and Se2 representing the inner layer Se atoms. Bi only has one site. The coupling between each adjacent atom planes within a QL is a strong covalent bond, while between the QLs are weak van der Waals interactions, which allows the crystal to be easily cleaved along inner QL plane. Each atomic layer has three possible positions along the c-axis of the crystal, stacked in A(Se1)–B(Bi)–C(Se2)–A(Bi)–B(Se1)–C(Se1)–A(Bi) – B(Se2)–C(Bi)– ABC order [62], as shown in Figure 4.1(b)-Bi_2Se_3(left). With foreign atoms' intercalation, the intercalants (in this case Nb) tend to go in-between the weak van der Waals gap, which breaks the ABC stacking symmetry of the Bi_2Se_3 host structure. Now with C' (Nb) replacing the C(Se1) stacking, the new stacking order in Bi_2Se_3 becomes –A(Se1)–B(Bi)–C(Se2)–A(Bi)–B(Se1)–A(Se1)–B(Bi)–C(Se2)–A(Bi)–, shown in Figure 4.1(b) Nb-Bi_2Se_3(right). This ABC stacking faults further leads to a lattice disorder observed as Periodic Lattice Distortion in our following Selected Area Electron Diffraction (SAED) measurements, shown as Figure 4.2.

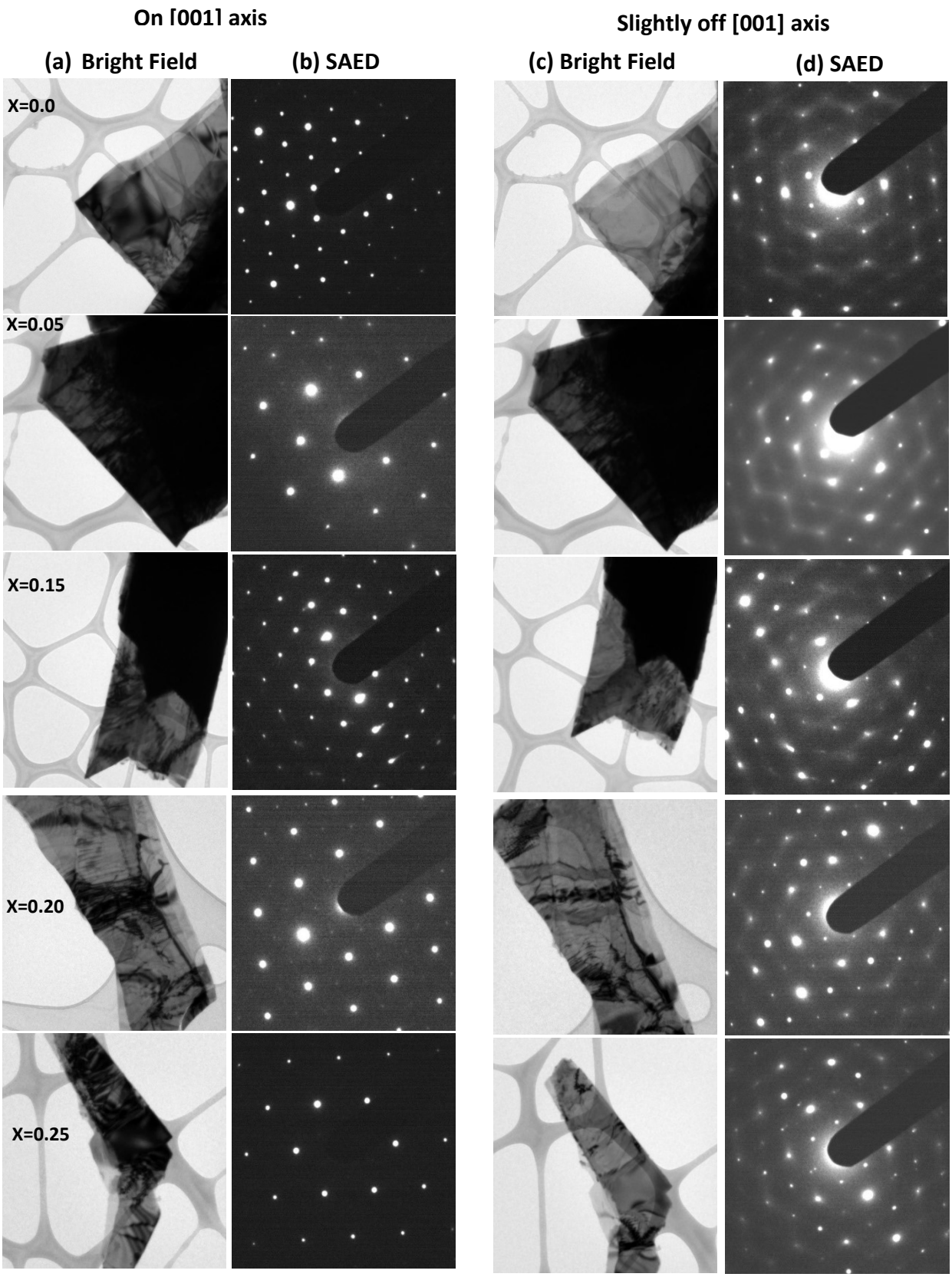
On [001] axis
Slightly off [001] axis
(a) Bright Field
(b) SAED
(c) Bright Field
(d) SAED
X=0.0
X=0.05
X=0.15
X=0.20
X=0.25

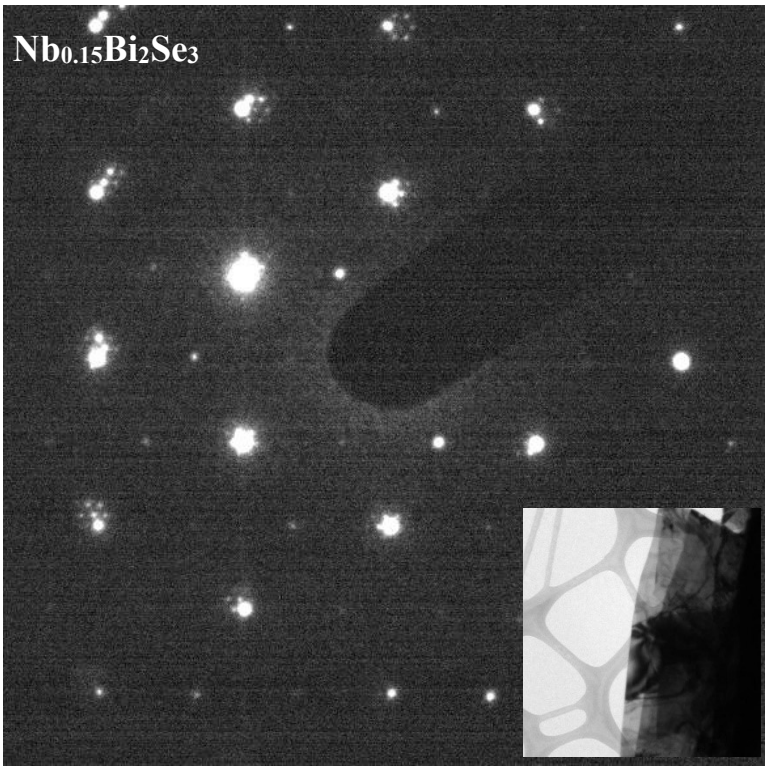

Figure 4.2 Bright field Transmission Electron Microscopic and Selected Area Electron Diffractogram (SAED) for $Nb_xBi_2Se_3$ with x=0.00, 0.05, 0.15, 0.20 and 0.25. Each row in the figure corresponds to a specific value of x, as shown. Each column in the figure corresponds to a different type of image, as described here. (a) Bright field images on [001] zone axis; (b) SAED on the same [001] zone axis; (c) Bright field image with a slight off-zone-axis tilt of less than 5 degrees; (d) SAED with the same slight off-zone-axis tilt of less than 5 degrees, as in (c). Figure (e) shows on [001] zone axis SAED results from a second piece of the x=0.15 sample, with the corresponding bright field image as an inset . Note six small, weak satellite spots near each Bi_2Se_3 Bragg spot, indicating the formation of a superlattice.

Figure 4.2 displays Electron Diffaraction images for bright field images(a) on single crystal pieces with x=0.00, 0.05, 0.15, 0.20 and 0.25, and Select Area Electron Diffractions (b) along [001]-zone axis on the respective crystals of (a). The strong diffraction contrasts with layered structure can be seen in Figures 4.2 (a), indicating of good crystal quality and single crystal features. In Figures 4.2 (b), besides the Bi_2Se_3 host structure, the normally forbidden 2/3 of the reciprocal lattice diffraction spots are also observed with weak diffraction features. Usually these weak diffraction spots are

generated by ABC stacking fault. Along c-axis, the Nb or Bi intercalation changed the local structural stability and broke the original structure symmetry [68, 69]. To further examine the reasons behind this extra fraction spots, we tilted each of the crystals by less than 5 degrees as shown in bright field images in Figures 4.2 (c) and the corresponding SAED is in Figures 4.2 (d). In this case we were not only able to see these extra diffraction spots, but we also observed diffuse "streaks", which are located in between the reflections of the Bragg spots. Such diffuse streaks are an indication of Incommensurate Charge Density Wave related to structural lattice disorder (discussion please see section 3.2.1), which leads us to look for possible ordered Charge Density Wave at lower temperatures. Note: on a different piece of x=0.15, we also observed satellite spots which were identified around each of the strong reflection spots around host structure. These satellites and spacing indicate an Incommensurate Charge density Wave [17-21, 28, 29]. Such I-CDW has also been reported in Kristie's TEM studying of zero valent metal intercalated Bi_2Se_3, in which different doping levels I-CDW were observed as different parameters of real spacing [28].

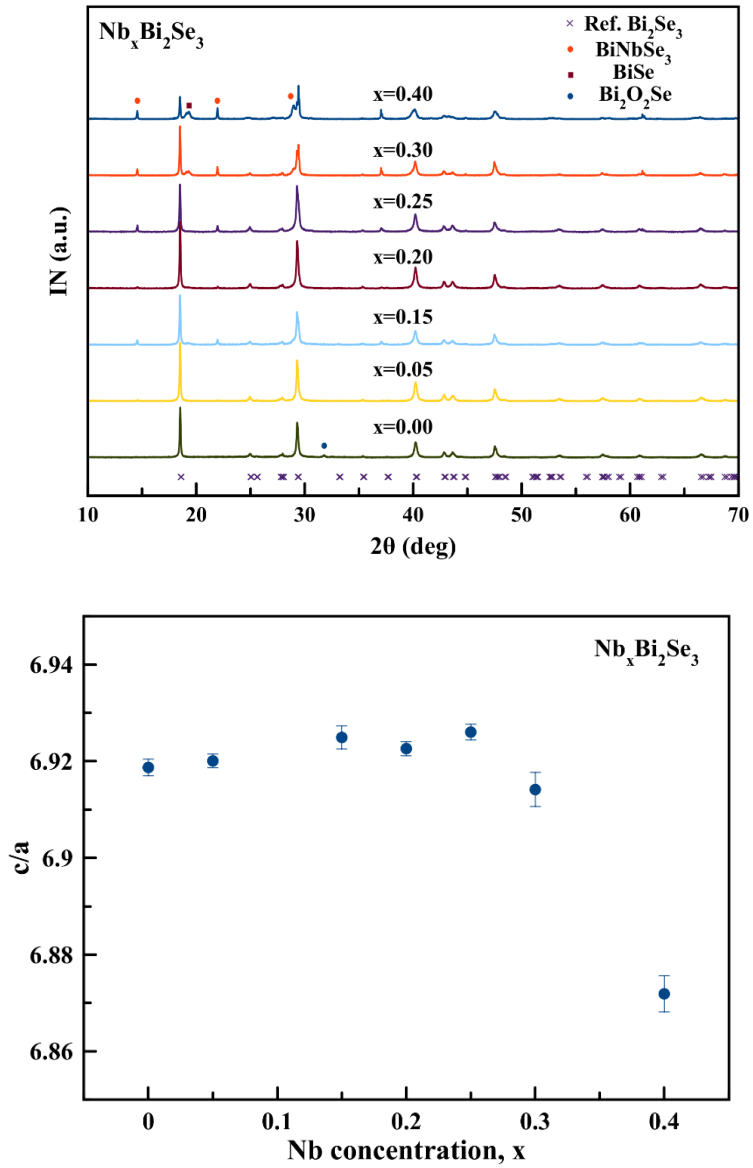

Figure 4.3 Powered x-ray Diffraction results on $Nb_xBi_2Se_3$. (a) X-ray Diffraction results with increasing Nb concentration *x* (bottom to top, *x* = 0.00, 0.05, 0.15, 0.2, 0.25, 0.3 and 0.4). Same as earlier reports on this compound, different levels of impurity phase were identified: blue dot on Bi_2Se_3 indicating grinding introduced $BiSeO_2$, Orange dots indicating $BiNbSe_3$ and red dots indicating BiSe. (b) c-axis/a-axis ratio shifting with Nb concentration, where the results are from fitting of the Bi_2Se_3 phase by setting impurity phases as background in the Rietveld refinement.

Crystal structures of the sample were also examined by XRD. Figure 4.3 displays XRD from powdered crystals together with results of Rietveld refinement based on R$\underline{3}$m (D_{3d}^5) space group

with a rhombohedral crystal structure. Crystal parameters *a* and *b* were constrained at *a*=*b*. Same as earlier reports for this material, different levels of impurity phases were identified from the refinement as displayed in Figure 4.3 (a). In Figure 4.3 (a) The blue dot on Bi_2Se_3 is grinding introduced $BiSeO_2$ impurity which did not show on the other samples; This impurity can be reduced when I grind the sample in an Argon flowed glovebox. At higher concentrations above x=0.15, secondary phase BiSe were obtained showing as blue stars in the X-ray diffraction data. With concentration x=0.3 and 0.4, a third phase $BiNbSe_3$ were obtained, which are shown as the triangle in Figure 4.3 (a). The red triangle corresponds to the formation of a BiSe, a secondary phase. These same BiSe and $BiNbSe_3$ phases have been observed by other groups [144, 145], such as reference [49] and [50]. Figure 4.3 (b) displays the c/a ratio vs Nb concentration from GSAS retrieved fitting, where c/a first increases with Nb concentration (x=0.0 to 0.25); however, at x=0.3 a sharp drop was observed. As most reports have shown, the increased c-axis is an indication that most Nb have intercalated into the host structure [76]. While, the sharp drop at x=0.3 to x=0.4 can be related to over doping of Nb, where Nb^{3+} started to replace Bi^{2+} site [76].

To summarize this section, the effect of Nb doping on the crystal structure of Bi_2Se_3 was studied by using X-ray Diffraction and Selected Area Electron Diffraction (SAED). In the SAED results, appearance of the normally forbidden 2/3 reciprocal spacing diffraction spots indicates the ABC stacking faults which are likely caused by impurity (Nb/Se/Bi) intercalation. The diffuse scattering with the “streaks” feature in between the Bragg Diffraction spots together with the satellite spots on x=0.15 sample are indications of periodical lattice distortion, which are associated with an Incommensurate Charge Density Wave state. The X-ray diffraction, similar to earlier reports of Ref [144] and Ref [145], with Nb concentration x>0.15 impurity phase of BiSe and $BiNbSe_3$ were

found in the host structure. Also, for the host Bi_2Se_3 phase, c/a ratio initially increased with Nb doping levels, indicating intercalation. At x=0.3 and x=0.4, c/a ratio dropped, as in Figure 4.3 (b), which indicated that with increased Nb doping, some of the Nb^{3+} will start to replace the Bi^{2+} site.

4.2.2 Observation of CDW and SC transitions from Transport Measurements

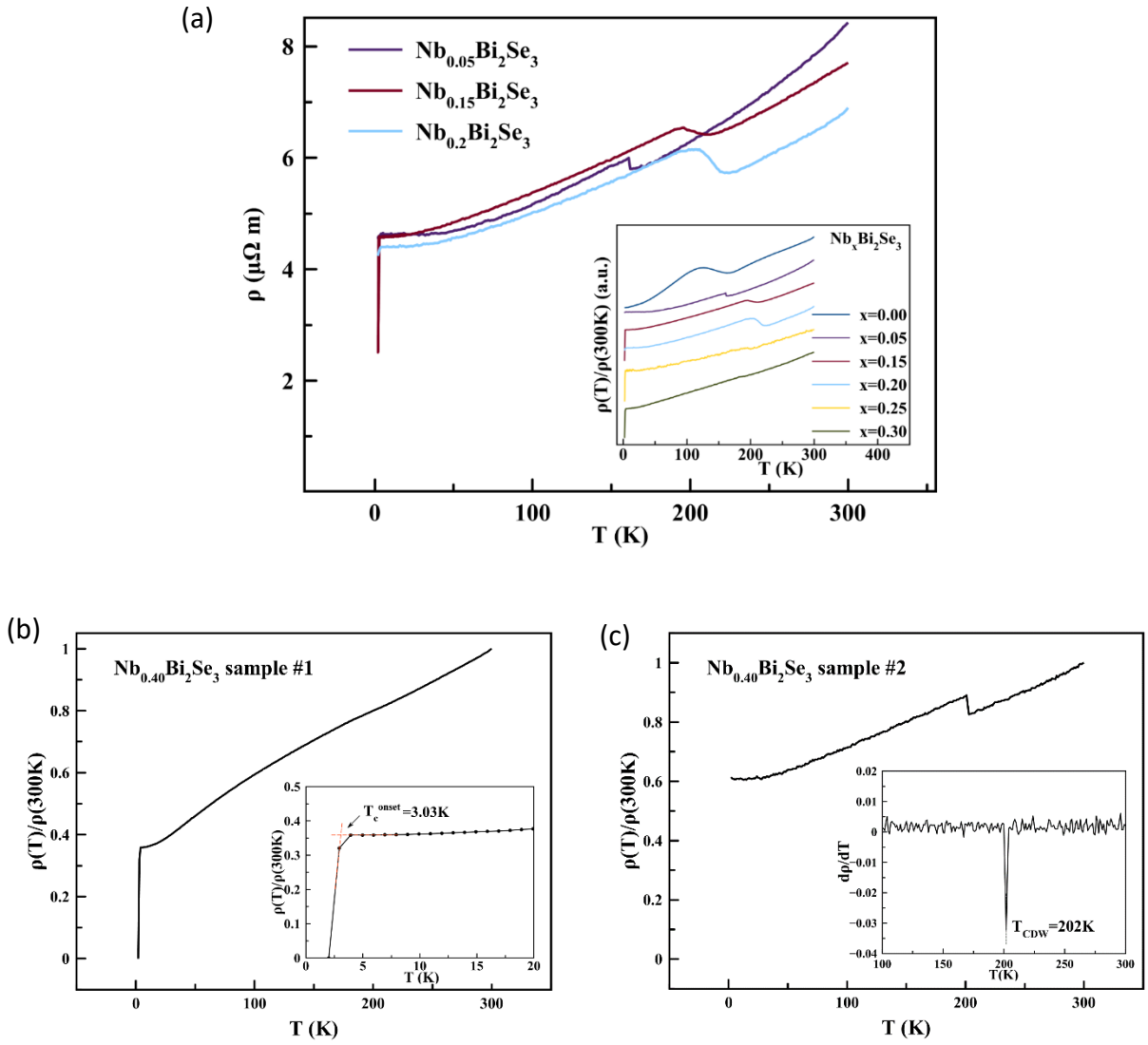

Figure 4.4 (a) Temperature dependence of resistivity ρ(T) for $Nb_xBi_2Se_3$ (x=0.05, 0.15, 0.20) crystal. Inset: ρ (T)/ρ (300K) as a function of T for $Nb_xBi_2Se_3$ (x=0.00, 0.03, 0.05, 0.15, 0.20, 0.25 and 0.30). Note Charge Density Wave transition temperatures T_{CDW} in the temperature range 140K - 200K. Superconducting transitions are observed between 0.0K - 3.9K. (b),(c) are two different

pieces of x=0.40. Interestingly, sample #1 in (b) displays only a SC transition, whereas sample #2 in (c) displays only a CDW transition. Inset graph of (b) is T_c^{onset}, taken from the intersection of lines from the normal resistence curve and the linear drop of the superconduting state. Inset graph of (c) is T_{CDW}, taken from the lowest inflection point dρ(T)/dT.

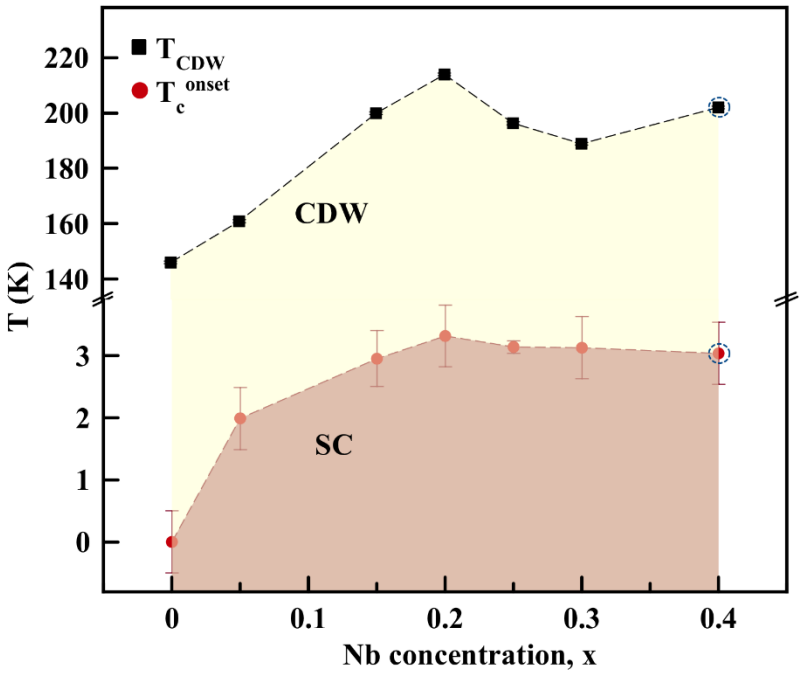

Figure 4.5 Phase diagram of $Nb_xBi_2Se_3$ showing temperature of transition varying with nominal Nb concentration x and superconducting onset. Charge Density Wave phase (black square) and Superconducting Phase (red dot) serve to differentiate the two phases. Reported density wave transition temperatures T_{CDW} correspond to the lowest inflection point in dρ(T)/dT curves for CDW, same as Figure 4.4(a) inner. Superconducting transition T_c^{onset} corresponds to the superconducting onset for each sample, same as Figure 4.4(b) inner. Bule circles for the x=0.4 Nb concentration sample are used to indicate that the SC and CDW were not found to co-exist but were instead taken from different pieces. In all of the remaining samples, SC and CDW were measured from the same sample.

Figure 4.4(a) shows temperature dependent zero-field resistivity on ab-plane of $Nb_xBi_2Se_3$ (x=0.05, 0.15 and 0.20), with temperatures ranging from 2K to 300K. Inset of Figure 4.4(a) displays ρ(T)/ρ(300K) with temperature dependent for all different concentrations of Nb doped Bi_2Se_3. For all the displayed data, metal-to-insulator-like transitions were observed, signaling the opening of an energy gap. This indicates that the room temperature observed I-CDW locked into

an ordered charge density wave (CDW) state. The onsets of the CDW transition are between 140K to 200K. For the Nb doped samples with x>0.00, another sharp drop of resistivity was also obtained with temperature ranging from 2.9K to 3.4K, which is an indication of superconducting transition. Transition temperature in the superconducting transition temperatures are similar to earlier reports from Kobayashi et al. [144] for various Nb doped Bi_2Se_3 samples. The key difference with our results compared to earlier reports is that we discovered the Charge Density wave transition, whereas earlier reports did not show this. Such Charge Density wave transition was predicted by Lawson's group [123]. In their Quantum Oscillation study on Nb doped Bi_2Se_3, they found multiple Fermi pockets; however, we are the first ones to obtain experimental results. We also noticed that for our higher doped sample x=0.3 and x=0.4, the coexistence of SC and CDW are very weak, and in some cases only one or the other can be seen at all, as seen in Figure 4.4 (b) and (c). This might be due to the fact that increased doping can suppress the CDW state as studied in other materials [21].

Figure 4.4 (d) displays the Phase diagram of $Nb_xBi_2Se_3$ with Charge Density wave and superconducting phase transitions, temperature vs Nb concentration. Transition temperatures were determined from ρ(T) measurements by examining the lowest reflection point in dρ/dT for CDW and the Superconducting onset as T_c. No direct competition between CDW and superconducting states was observed from the phase diagram at x≤0.2. In fact, zero-field transport measurement shows that as Nb concentration increasing to x=0.2, both T_c^{onset} and T_{CDW} increase as Nb concentration increases. The coexistence of the two phases might have originated from our growth conditions caused by intercalation and structural disorder. The onset of SC and CDW for x=0.40 sample are from two different pieces: sample#1 and #2. This separation of CDW and SC can be

an indication of the competition between the two-phase transitions or the impurity which suppresses the CDW state.

4.2.3 Examination of SC transitions from Magnetization Measurements

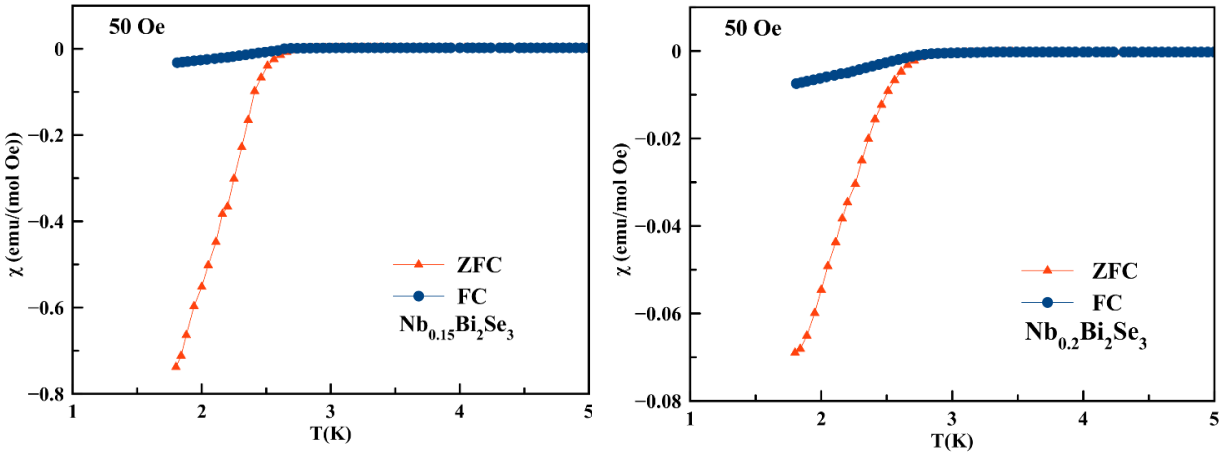

Figure 4.6 Temperature dependent DC magnetic susceptibility of single crystals of $Nb_{0.15}Bi_2Se_3$ and $Nb_{0.20}Bi_2Se_3$. (a) and (b) Under a nominal applied magnetic field of 50 Oe, ZFC and FC susceptibility for $Nb_{0.15}Bi_2Se_3$ and $Nb_{0.2}Bi_2Se_3$ from 1K to 5K.

Figure 4.6 displays DC magnetic susceptibility in zero-field cooled (ZFC) and field-cooled (FC) modes, with applied field of 50 Oe during field cooling and during measurement in the warm-up cycle. The single crystals were mounted inside plastic straws, with the c-axis parallel to the applied magnetic field and with plugged-in quartz wool to stabilize the sample inside the straw. Due to limitations of size and shape of the straw and the crystal, the x=0.2 sample had to be mounted slightly off-center. Note, superconducting transitions for (a) $Nb_{0.15}Bi_2Se_3$, and (b) $Nb_{0.2}Bi_2Se_3$ with T_c onsets of 2.8K and 3.5K respectively. These T_c values agree with the onset temperature measured by resistivity, of 2.95K and 3.32K, respectively.

It is important to rule out the CDW or SC from a secondary phase, such as the well-known CDW in $NbSe_2$ or $NbSe_3$. After a carefully researching related literature [47, 48, 54], we found the T_c and T_{CDW} for $NbSe_2$ and $NbSe_3$ are not in the range of what we are observing. For $NbSe_2$ its T_c is at 7.2K which is higher than the T_c of our Nb doped Bi_2Se_3, while, its T_{CDW}=33K is much lower than our T_{CDW} transition. For $NbSe_3$, it only has superconducting under pressure, while T_{CDW} is 145K, which is below most of our Nb dope Bi_2Se_3 CDW transition temperatures. Even though this transition is close to the CDW transition temperatures reported here for $Nb_{0.05}Bi_2Se_3$, we do not believe that the significant change in resistivity reported in Figure 2 can come from a minor $NbSe_3$ secondary phase. Furthermore, considering the fact that our pure Bi_2Se_3 also has the Charge density wave transition and T_{CDW} shifts with increasing Nb concentration, it confirms that our T_{CDW} transition was not from a secondary phase, but is rather related to Bi_2-layer/Se self-doping [70, 73] and Nb intercalation.

Relationship between SC and CDW phases:

Layered chalcogenides can host both CDW and SC ground states, which is discussed and shown in section 1.1.3. Bi_2Se_3 has a similar crystal structure to other transition metal dichalcogenides. Even though the Bi_2Se_3 we grew is a 3D bulk crystal, it has a 2D-like layered structure. In between the adjacent quintuple layer building blocks of Bi_2Se_3, the bonding force is weak van der Waals Force, whose strength is tunable by external perturbation. By applying pressure or metal intercalation, unconventional superconductivity was reported in this material, as in $NbSe_2$, the leading factor of unconventional superconductivity which seems to be related to strong electron-phonon interactions at long wavelengths [47, 48]. Thus, in our case, the CDW and SC are possible from the same origin; however, the underlying relationship of the two phases is hard to distinguish

(see discussion 4.3.2). As shown in Figure 4.5, T_{CDW} increases with SC transition T_c below Nb concentration x=0.2. However, for x≥0.2, with increased Nb concentration, the T_{CDW} decreases. Rietveld refinement of X-ray diffraction in Figure 4.3 reveals a decrease in c/a ratio, implying a change in intercalation-induced chemical pressure. Based on similar previous studies, including our own [76], we suggest that increasing x beyond x>0.25 results in substitution of Nb into Bi sites. Additionally, we note a gradual increase in the formation of secondary phases ($BiNbSe_3$ and BiSe) with increasing x beyond 0.25, as also reported previously [144, 145]. In conclusion, it seems that doping Nb beyond x>0.25 results in increased disorder, in turn leading to a suppression of T_{CDW}. It is interesting to now observe that T_C also decreases, as if to follow T_{CDW}. This scenario of disorder-induced suppression of T_{CDW} also appears to be borne out from the broadening of the T_{CDW} transition for x≥0.25 shown in Figure 4.4, eventually lost the transition feature by the time we reach a Nb concentration of x=0.4.

To summarize these findings, our resistivity measurements identify a metal-to-insulator-like phase transitions and SC transitions, where SC phased was further examined by magnetization measurement. The possibility that an impurity phase may introduce CDW and SC transitions were ruled out based on the earlier reports and these transitions shifting with Nb concentrations. With the coexistence of strong Fermi nesting, electron-phonon interaction, spin-orbital coupling and multiple band structure, the underling mechanism for SC and CDW in Nb doped Bi_2Se_3 is hard to explain in just a single picture. In order to confirm SC and CDW order and their correlation at levels below T_c, further measurements at lower temperatures are needed, such as STM and ARPES to ascertain whether the CDW state persists with SC.

4.2.4 ^{209}Bi NMR Spectra linewidth broadening on $Nb_{0.05}Bi_2Se_3$

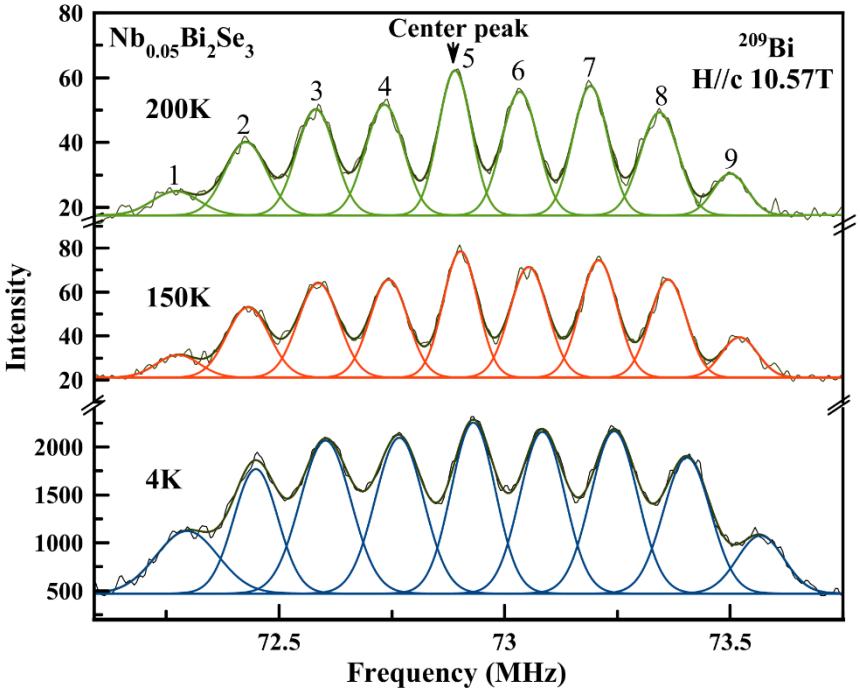

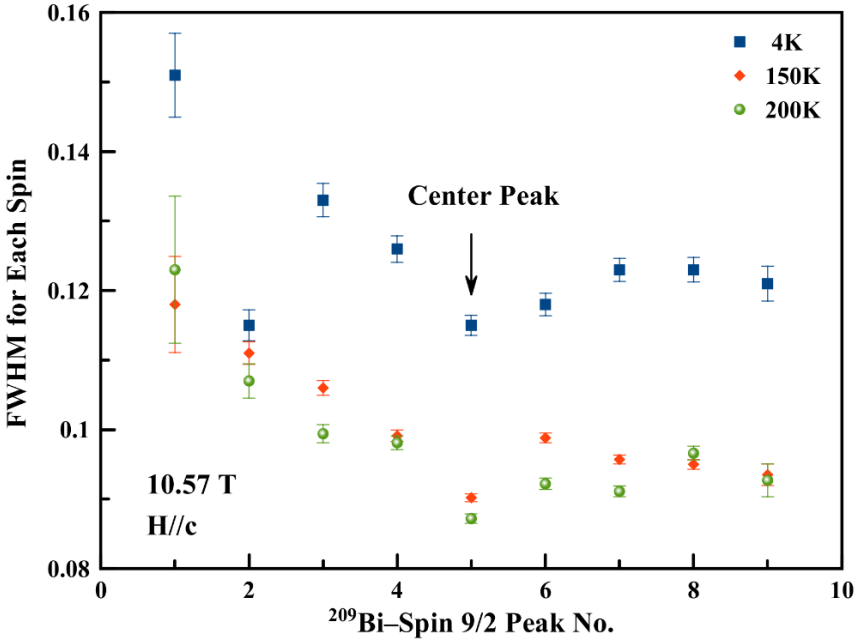

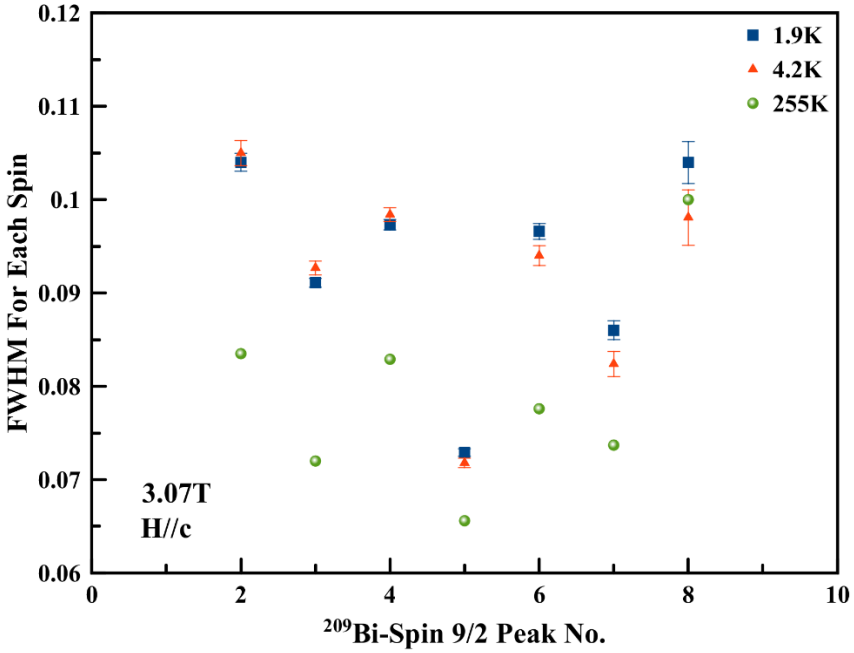

Figure 4.7 ^{209}Bi NMR on crystal $Nb_{0.05}Bi_2Se_3$, with applied magnetic field H=10.57T(a), (b); H=3.07T(c) and parallel to the c-axis of the crystal. (a) Frequency sweep spectra (72MHz to 74MHz) at temperatures below T_{CDW} (4K, blue), near T_{CDW} (150K, orange) and above T_{CDW} (200K, green). Each peak was fitted by Gaussian function. The black curve line and dark green curve line for each spectra, represent the raw data and Fit-sum. The numbered 9 peaks are from the spin-9/2 of ^{209}Bi, with center peak labeled as No.5. (b) Full Width at Half Maximum (FWHM) for each individual peak from (a) vs Bi-Spin 9/2 Peak No. at three different temperatures. Blue square, Orange diamond and green solid ball represent 4K, 150K and 200K. (c) H=3.07T, Full Width at Half Maximum (FWHM) for each individual peak (No.2 to No.8—No.1 and No.9 has missing intensities) from Bi-Spin 9/2 Peak No. at three different temperatures. Blue square, Orange diamond and green solid ball represent 1.9K, 4.2K and 255K.

Figure 4.7 displays the ^{209}Bi NMR measurement for crystal $Nb_{0.05}Bi_2Se_3$, with the applied static magnetic field magnitude H=10.57T (our sample at non-superconducting state, superconducting H_{c2}<3T) [60] and orientation parallel to the c-axis of the crystal. As shown in Figure 4.7 (a), frequency sweep spectra (from 72 to 74MHz) were taken at temperature 4K, 150K and 200K, which are below, at and above T_{CDW} (=161K for $Nb_{0.05}Bi_2Se_3$). With fitting of Gaussian functions, total of 9 peaks from spin-9/2 of ^{209}Bi were shown in each temperature's spectra. The full-width at half-maximum (FWHM) of individual peak line shape vs peak number were plotted to quantify

the lines broadening as a function of temperature, as shown in Figure 4.7(b). Except for the peak No.2, all the other peaks' FWHM show a feature of homogeneous broadening (~30%)--by comparing FWHM at 4K in Figure 4.7(b) to the FWHM above T_{CDW} (200K in Figure 4.7(b)). Besides the individual peak broadening, the satellite transitions are also increasingly broadened and become more asymmetric as their location increases from the central transition. This same observation has been discussed in Willson's dissertation [32]-Figure 5.8 for spin 9/2 ^{93}Nb in $NbSe_2$, which states this is the evidence of the CDW phase because the quadrupolar splitting is an electric field gradient induced effect and would most certainly be affected by a long-range charge order.

Discussion for NMR:

To review from a previous section, NMR is a magnetic local probe to detect local, microscopic information about the spin dynamics, chemical and structure natures of materials through coupling of a specific nuclei with its local environment [107, 108]. The nucleus's degeneracy of spin degrees of freedom can be broken by Zeeman interaction H_z with application of static magnetic field that splits the energy levels, and by the interaction H_{int} of spins with the environment (dipolar interaction, chemical shift, quadrupolar interaction and so on) [108]. With application of Resonant radio frequency radiation, the energy can be absorbed by the nucleus spins that cause transitions between the energy levels. Following the energy absorption, the spins start to exchange this energy among themselves and to transfer energy to other degrees of freedom of the lattice to return to equilibrium. As the magnetization returns to equilibrium, a decaying electrical signal in the time domain called free induction decay (FID) will be introduced. The Fourier transformation of FID

gives us the NMR spectrum. A spin-echo technique is a "back-to-back" FID to get the NMR spectrum. Therefore, both the position and shape of the absorption line (FID) contain structural and dynamical information concerning the nucleus with its local environment [105, 108].

Contributions to NMR line shape have homogenous and inhomogeneous factors, where homogenous line shape usually found in solids and single crystals can be fitted with Gaussian, while the inhomogeneous line shape has separate parts that originated from separate contributions. The line broadening can be either due to inhomogeneous line shape or due to a wide range of homogenous factors such as phase transitions, where CDW is one of the specific examples. In the case of CDW, below the transition, the periodic modulation of the charge density can lead to periodic modulation of the electric-field-gradient (EFG) tensor. The symmetry effects are particularly spectacular on the electric field gradient since the NMR quadrupolar interaction magnitudes are in general large, where even very small local distortions can be detected [107, 108]. This further leads to a change in the frequency associated with the transitions between the nuclear levels, which can be reflected as a line broadening [2].

Above the Peierls transition, a quadrupolar interaction effect can lift the degeneracy between the transitions corresponding to the different nuclear levels, given by:

$$\Delta\nu^{0}_{m\rightarrow m+1}(R) = \frac{2m+1}{4}\nu(Q)f(\Theta), \tag{4.1}$$

with $\nu(Q)=\frac{3e^2qQ}{2I(I-1)}$

where Q is the quadrupole moment, I is the spin of the nucleus, eq is the main component of the EFG tensor induced by external charges of the nuclei, and f(Θ) is orientation factor between external applied magnetic field and the EFG principal axis.

Below the Peierls transition, the electric charge is modulated and the associated transition between the nuclear levels is as shown (Berthier and Segranson, 1987)

$$\Delta\nu_{m\to m+1}(RG) = \Delta\nu^{0}_{m\to m+1}(TC) + \frac{\omega_1}{2\pi}cos(2k_F r + \varphi) + \frac{\omega_2}{2\pi}cos^2(2k_F r + \varphi), \quad (4.2)$$

where the numerical factors ω_1 and ω_2 depend on the amplitude of the CDW and on the quadrupole moment [2, 146].

The satellite widens as it moves away from the central transitions, which is related to the underlying CDW mechanism in the compound [107, 147]. Since we do not have enough evidence to fully understand the nature of CDW (eg. The number of CDW channels, dimensionality and so on), we discuss our speculations based on previous CDW related quadrupolar NMR studies. In the H//c direction, the EFG on the central transitions can be neglected [148]. The most likely reason for satellites becoming wider is due to the nature of quadrupolar splitting being EFG induced and the fact that CDW can provide a supplementary EFG. As additional EFG is distributed, we observed an anomalous NMR broadening on the satellites [147]. This is similar to the conclusion in Willson's dissertation where he mentions this is an indication of discommensurate CDW, which is a mixture of ordered CDW and I-CDW coexisting [107]. Another material with Charge-Density Wave is Cuprate Superconductors [149], which has also discussed similar phenomenon where the long-range correlations below T_{CDW} can produce a lineshape asymmetry that grows with decreasing temperature.

In the NMR studies for line broadening near CDW phase transitions, the FWHM broadening with lowering of temperatures have been reported and discussed in the spin-9/2 ^{93}Nb NMR in $NbSe_2$ and ^{17}O NQR (Quadrupole Satellites of NMR lines) in YBCO [107, 150]. In the case of spin-9/2 ^{93}Nb in $NbSe_2$ [107], CDW was shown by the FWHM broadening as temperature drops at the central transition and the first satellites, where pre-broadening was observed, and it became more rapid after T_{CDW}. In the case of NQR in YBCO [150], the broadening of width starts to increase with a drop in temperature at T_{CDW}, in which the width is the largest with lowest available temperature. According to our results, since we do not have quantitative data to represent the transition shape, we presented the FWHM for individual peak at the three available temperature ranges. Similar to the above aforementioned observations [107, 150], in each spin of ^{209}Bi as shown in Figure 4.7 (b), FWHM at 200K is increased by 30 to 40% when the temperature drops to 4K. As shown in Figure 4.7 (c), we also performed 1.9K, 4.2K and 255K spectrum measurements by applying static magnetic field H=3.07T on the same sample and at the same orientation as in Figure 4.7. The low field (H=3.07T) setup results in Figure 4.7(c), individual peak FWHM broadening from peak #2 to #8 were observed, as well as the FWHM becoming wider and asymmetric the farther away it goes from the central peak, which are contributed by the CDW order. The broadening here is not as homogeneous as Figure 4.7(b), which could be due to the signal-to-noise level in NMR ~$B^{1.5-2}$ [146]. For peak #1, the intensity is missing at 255K, which is probably related to the CDW asymmetric behavior as it moves away from central peak [107]. Thus, our NMR from nuclear local environment further proved the existence of CDW in Nb intercalated Bi_2Se_3.

4.3 Discussion for the origin of the phase transitions

4.3.1 Crystal Lattice Distortion

The crystal structures of $Nb_xBi_2Se_3$ have been studied by X-ray Diffraction and Selected Area Electron Diffraction, where the change of crystal structure has been identified from stacking faults, diffuse scatterings, satellites reflection and increased c-axis. The origin for the changing of crystal structure is largely contributed by intercalation from Nb or/and self-doped Bi into the host structure of Bi_2Se_3 as well as some level of substitution (Nb^{+3} ion replacing Bi^{+2} ion site at x>0.25). Due to these internal "defects", the Periodic Lattice Distortion was induced to the host structure with the sign of diffuse scattering and satellite diffraction. As it has been discussed in Chapter 1 from Peierls theory that Periodical Lattice Distortion (PLD) and charge density wave always accompany each other. PLD can cause a local potential change for each electron which leads to an electronic density modulation. In turn, each ion will also see a different potential that is driven by electronic modulation, and as such, the ions will also try to reposition themselves with the new equilibrium. This phenomenon is commonly seen in chalcogenides [17-21], because their unique layered structures are more convenient in forming atom chains to lead to instability in lattice and charge degrees of freedom. Thus, it is not a surprise to see CDW transition in layered Bi_2Se_3. Since PLD/CDW is generally preferable with the condition of strong electron-phonon coupling, whereas in the case of intercalated Bi_2Se_3 the strong electron-phonon coupling constant associated with phonon dispersion has been recently proven from both theoretical calculations and experimental observations [100, 101][also discussed in chapter3]. It should be mentioned that in the one-dimensional case a complete softening of phonon mode q_0 has a wavelength $\lambda_0 = 2\pi/|\mathbf{q}_0| = \pi/|\mathbf{k}_F|$, where k_F is determined by electron filling of the band structure in the momentum space [2,4]; consequently, the associated superstructure is not necessarily commensurate with the underlying

lattice. As a result, we observed "streaks" between Bragg spots of the host structure and satellite diffraction spots that is not in integer spacing of the crystal lattice, and these observations can also be defined as Incommensurate Charge density Wave at levels above T_{CDW}.

Besides the intercalation phase in Bi_2Se_3, the other possible origin for the CDW order could be related to the anti-phase grain boundaries defects. When performing TEM and STM/STS measurements on thin film Bi_2Se_3, Liu et al. found charged grain boundaries in their material [151, 152]. Combining this with theoretical calculations, they concluded that this charging is specifically due to the appearance of anti-phase grain boundaries. It is likely that during the crystal growth, different nucleation sites of Bi_2Se_3 formed along the *[001]* direction. A mismatch between Bi-Bi plane from one nucleation site's grain to the other nucleation site's grain of Se-Se plane (or the other way around) can introduce such anti-phase grain boundaries. Furthermore, if this Bi-Bi & Se-Se interface follows a certain sequence of repeated numbers (e.g. ±3/5quintuple layer variant), it will lead to charging (and potential shifts) near the grain boundaries. In our case, the $Nb_xBi_2Se_3$ are bulk crystals, and thus, the grain boundaries related mechanism could be more complicated. However, the antiphase boundaries (Bi-Bi to Se-Se or Nb-Nb) can still be formed in the as-grown crystals. With enough interface states, the incommensurate lattice disorder can be generated. When decreasing the temperature, the incommensurate state can be further locked into CDW state. Therefore, it is also possible the anti-phase grain boundaries in our material can lead to CDW.

In addition to the mechanisms mentioned above, a third possible origin that could be discussed is from a misfit phase of BiSe-$NbSe_2$, where the stacking of BiSe and $NbSe_2$ forms a structure of $BiNbSe_3$, which is recently reported having a SC transition [124]. This mechanism seems less

likely to occur in our samples due to the following three reasons: (1) our low concentration samples x=0.0 and 0.05 have no $BiNbSe_3$ secondary phase but show CDW transitions; (2) x=0.05 sample also shows SC transition; (3) our samples show the dependence of CDW and SC transition temperature with Nb concentration.

4.3.2 Fermiology in electronic phase transitions

The particular fermiology (including shape of Fermi surface, the density of states at the Fermi level and underlying dispersion) plays an essential role in the electronic phase transitions in materials that can be described by Peierls theory [1,2, 17-21], such as in layered chalcogenides. CDW and SC both are symmetry breaking phases that can be driven by fermiology and usually feature an energy gap. In the case of Bi_2Se_3, its fermiology can be tuned through chemical doping(intercalation/substitution), changing of strain, and applying pressure [100-102, 123], which further led to the intertwined electronic state. Based on the current literature reports, I summarized three different types of fermiology in Nb-Bi_2Se_3 that could lead to CDW and SC order:

(a)Multiple Fermi surface

Lawson et al. reported that $Nb_xBi_2Se_3$ host a complex electronic band structure, a Fermi pocket off the Brillouin Zone center in addition to the main ellipsoidal Fermi surface characteristic [100-102, 123]. They suspect that this multiple Fermi surface is driven by Nb d-orbital electrons. A potential CDW which can be led by this strong Fermi nesting from multiple Fermi surface and a possibility of the Fermi nesting which can drive the unconventional SC mechanism in $Nb_xBi_2Se_3$, were also suggested by them.

(b)Strong Fermi nesting along Γ_z direction

With Cu intercalation into Bi_2Se_3, A.Yu. Kuntsevich et al. [153], Xiangang and Sergey [100, 101] suggest that small position changes for the intercalant along the Γ_z-direction can modify the nesting vector $X(q)=\Sigma\delta(\varepsilon_k)\delta(\varepsilon_{k+q})$, where ε_k and ε_{k+q} represent energy states near the Fermi level. When wavevector q is close to zero, this nesting vector along ΓZ is largest and resulting in strong Fermi nesting and strong electron-phonon coupling along this direction, which together with the topology of Bi_2Se_3 further lead to unconventional superconductivity in doped Bi_2Se_3. In the same material, Lauhous et al. also report the presence of an open-cylinder like electron pocket in the ΓZ direction [102], centered around the Γ point, indicates the presence of Fermi surface nesting along ΓZ, with the nesting function being strongest at low q [100].

(c) Hexagonal deformed fermi surface

Previous work on compounds such as Bi_2Te_3 and Bi_2Se_3 had revealed a hexagonal Fermi surface with two flat segments which faced each other and were separated by $2k_F$ along the Γ-K direction leading to predictions of strong nesting and density wave order in such systems as well [68, 69]. Fu has proposed that the spin-orbit interaction associated with hexagonal warping plays an important role in pinning the two-component order parameter and makes the superconducting state fully gapped [69].

In summary, the three possible mechanisms for fermiology allow us to understand the connection between SC and CDW, and yet it leaves mysteries unsolved. If the two phases originate from the same Fermi nesting mechanism, they will compete. If they are from different Fermi nesting mechanisms, they can coexist. Or they can have both conditions which are from multiple nesting

channels or they are happening at different parts of a same Fermi surface. However, based on the examination on the crystal structure, our sample's CDW more likely originated from intercalation induced PLD/CDW related to (b). The SC origin could be (a), (b) or (c). Further study is needed to understand the underlying relationship between CDW and SC.

4.3.2 Crystal Growth Considerations

Aside from this, as is discussed in Bi_2Se_3 crystal growth (chapter 3), crystal growth also plays a large role in the resulting crystal structure and further leads to a change in electronic properties. Our crystal growth of Nb-Bi_2Se_3 involved high temperature annealing and quenching. Schneeloch et al. [96], and Nathaniel P. Smith from our group [141], studying $Cu_xBi_2Se_3$, have suggested that quenching (i.e., differences in quenching temperature, as well as the difference between quenching versus not quenching) drives the nature of intercalation, the nature of the Fermi surface, the presence or absence of superconductivity and even the superconducting fraction in a given sample. Schneeloch et al. [96], conclude that high temperature annealing and quenching can help maintain either intercalation phase or the impurity phase which can lead to SC. However, our study showed that the superconducting transition shifts with Nb concentration, which leads us to believe the first scenario is more probable.

4.4 Experimental Method

$Nb_xBi_2Se_3$ single crystals with $0 \leq x \leq 0.4$ were grown by self-flux method. High-purity (99.999%) powders of Bi, Se and (99.99%) Nb in stoichiometric ratios were prepared using a method similar to that described in ref [70]. Stoichiometric mixtures of 2.5g batches were sealed into high-quality quartz tubes in vacuum after being weighed and sealed in an inert glove box, being careful to not

allow it to be exposed to air. The mixtures in sealed quartz tubes were heated up to 850°C and maintained at that temperature for 20 hours. They were then cooled to 650°C at 0.1°C/min, followed by quenching in ice water. Crystals with $x > 0.4$ were of relatively poor quality and are not discussed here.

Powder X-ray Diffraction (XRD) measurements were performed using a Bruker D8 Discover x-ray diffractometer with Cu Kα radiation. Rietveld refinement was performed using GSAS (General Structure Analysis System) with an EXPGUI interface. Selected Area Diffraction (SAED) was performed at room temperature with a Hitachi H-9000NAR high-resolution transmission electron microscope (HRTEM) operated at 300 kV. Crystals of $Nb_xBi_2Se_3$ (x= 0.00, 0.05, 0.15, 0.20 and 0.25) were gently ground by hand in a mortar and pestle and dispersed on lacey carbon grid. Variable temperature resistivity studies were performed using 4-probe silver paste contacts on single crystals placed in a Quantum Design (QD) 9 Tesla Physical Property Measurement System (PPMS). Temperature and field-dependent magnetization measurements were performed using a QD MPMSXL-5 Magnetic Property Measurement System (MPMS) using a superconducting quantum interference device (SQUID). Pulsed ^{209}Bi Nuclear Magnetic Resonance (NMR) was performed on $Nb_{0.05}Bi_2Se_3$ single crystal of crystal size ~5.3 x 4.2 x 1.2 mm^3 placed inside a home-built probe in an 18-Tesla Helium cryostat. The single crystal $Nb_{0.05}Bi_2Se_3$ was studied with magnetic field oriented in H//c-axis, where the orientation was determined by angle-dependent measurements. Spin-echo signals for ^{209}Bi NMR spectra were processed using the summed Fourier transform method, with frequency swept from 72MHz to 74MHz and static magnetic field H=10T.

4.5 Conclusion

In summary, Charge Density Wave and Superconducting transitions were revealed in Nb intercalated Bi_2Se_3. In this system CDW is accompanied by superconductivity in all our samples of $Nb_xBi_2Se_3$, $0 < x < 0.4$. In the $0< x<0.25$ regime, T_{CDW} and T_C increase as Nb concentration increases. In the $x>0.25$ regime, both T_{CDW} and T_C decrease with increasing Nb concentration. This is possibly due to a disorder-induced suppression of both charge orders. Further work is required in order to understand whether the two orders coexist or compete at low temperature. Using Selected Area Electron Diffraction (SAED), which shows diffuse "streaks" and satellite reflections, we confirm the presence of a Periodic Lattice Distortion (PLD) and an Incommensurate Charge Density Wave (I-CDW) at room temperature. Our temperature dependent resistivity measurements reveal metal-to-insulator transitions from 140K to 200K. On sample $Nb_{0.05}Bi_2Se_3$, both high field and low field ^{209}Bi NMR spectra line shape with broadening at 4K (below T_{CDW}) were compared with spectra line shape at 200K/255K (above T_{CDW}), which further confirmed our locked-in CDW state. We believe that a higher-temperature I-CDW state locks into a CDW ordered state around 150-200K, which we assign as the CDW transition temperature T_{CDW}. We discuss our results in the context of weak coupling between layers, and distortion-induced charge order along the z-axis. We also discuss the role of strong Fermi nesting, electron-phonon interaction, spin-orbital coupling, and multiple band structures. This work reveals that a better understanding of the charge order revealed here is important to the eventual understanding of superconductivity induced in this quantum material which is also a topological insulator. Further measurements, and theoretical examination will be needed in order to fully reveal the underlying physics in Nb-Bi_2Se_3.

Chapter 5: Lattice and Charge Order in Cu intercalated Bi_2Te_2Se

Metal intercalation into layered topological insulators Bi_2X_3 (X=Te/Se) has been found to yield new phase transitions such as superconductivity, spontaneous magnetization, charge/spin density waves and novel two-dimensional (2D) electron-gas physics. These provide a fertile ground to examine the interplay between disorder, lattice distortions, charge order, and condensed phases such as superconductivity. Of particular interest is the intercalation-driven interplay between the appearance of superconductivity together with charge density ordering (e.g., a Charge Density Wave) in layered chalcogenides. In this chapter, I will report a study of Cu intercalation effects on Bi_2Te_2Se (BTS) from the point of lattice and charge order. Most of this chapter has been published in Ref. [76]. With Cu concentration $0.00 \leq x \leq 0.50$, we explored the effect of varying Cu content on crystal structure, phonon and electronic properties. Our studies of resistivity and electron diffraction indicate the existence of a charge density wave in this system. In our electron diffraction studies, we also find evidence for strong Bragg spots at reciprocal lattice positions forbidden by ABC stacking. These could result from the formation of a superlattice or other types of stacking faults. With increasing Cu content, the c-axis lattice parameter of $Cu_xBi_2Te_2Se$ increases monotonically for $0 < x < 0.2$, dropping precipitously at higher concentrations. Raman phonon modes A^2_1g and E^2g decrease monotonically for $0 < x < 0.2$. Based on our studies of this system, and studies of other binary systems, we believe that Cu intercalates up to x=0.2 and then begins to substitute for $x > 0.2$. The observation a CDW-like charge ordering in $x = 0.3$ indicates that increasing disorder likely leads to instability in the lattice and charge degrees of freedom in this ternary chalcogenide. Although we do not find evidence for superconductivity in Cu-BTS, the evidence for electron ordering, and possibly increased electron-phonon interactions, points to a strong possibility of superconductivity being discovered in this compound.

5.1 Motivation

As a Quantum Material, Bi-based topological insulators (TI) continue to generate interest due to their non-trivial electronic structure, and possible applications as materials for quantum computing and spintronics [58-61]. Intercalation of Cu in layered Bi_2Se_3 (BS) and Bi_2Te_3 (BT) yields superconductivity [95, 154] and, in the case of BS, a charge density wave (CDW) transition [100, 101]. Previous studies of $Cu_xBi_2Se_3$ (CBS) and $Cu_xBi_2Te_3$ (CBT) have revealed that phase transitions in these systems are driven by the location, nature of ordering, and total content of Cu [155, 156]. Electron diffraction studies of $M_xBi_2Se_3$ (M = intercalated metal) with higher concentration of the intercalant have revealed the formation of a superlattice (for M = Cu, Ag, Co, Sn) with a concomitant CDW ground state (M = Cu, Ag, Co) [100]. At these higher levels of intercalation, selected area electron diffraction displays alternating bright and dark diffraction spots in the (001) zone axis [101]; these dark spots are predicted to be forbidden in the ABC stacking of the host Bi_2Se_3. It is unclear whether the appearance of this superlattice pattern arises from symmetry breaking caused by stacking faults, or some form of periodic disorder caused by intercalation. Koski and colleagues have reported the observation of CDWs in intercalated Bi_2Se_3 based on electron diffraction results [100, 101]. However, these have not yet been followed up with variable temperature transport measurements to identify the CDW transition temperature. In their 1974 paper [18], Wilson, diSalvo and Mahajan had concluded from a study of a large number of dichalcogenides that the adoption of a superlattice distortion usually foretells the possibility of a CDW which, in turn, can co-occur with superconductivity. The question of whether an electronic modulation causes a structural distortion, or vice versa, is still a matter of debate in the literature [4]. In addition, the presence of such lattice and charge instabilities in the proximity of superconducting phases, such as the one in $Cu_xBi_2Se_3$ [95, 157], remains of interest.

In this paper, we examine the effect of Cu intercalation in the ternary chalcogenide Bi_2Te_2Se (BTS), a topological insulator which is isostructural with Bi_2Te_3 and Bi_2Se_3, but with a better ordered structure, and larger bulk resistivity [64, 158, 159]. It has been well-known for decades that $Bi_2(Te_{1-x}Se_x)_3$ is most ordered for $x = 1/3$ (which is Bi_2Te_2Se), due to the suppression of antisite defects, and Se/Te randomness, driven by stronger Se-Bi bonding [160]. In spite of this, and in spite of the observation of superconducting order in intercalated BS and BT, intercalated BTS has not been explored. We report the effects of introducing Cu ordering on the lattice and charge degrees of freedom by studying structural, vibrational, and electronic properties. Our results from x-ray diffraction, electron diffraction, Raman spectroscopy, and resistivity indicate that single crystal $Cu_xBi_2Te_2Se$ undergoes lattice expansion with increasing Cu, reaching full intercalation at Cu concentration of 20%. Higher Cu concentration reveals the presence of charge order and CDW transitions near $T_{CDW} \sim 220$ K. This is consistent with previous studies on layered dichalcogenides such as Cu-Bi_2Se_3, 4Hb-TaS_2 and 1T-$TaSe_2$ [4, 17, 95].

5.2 Experimental results and discussion

5.2.1 Crystal Structure: Cu doping effects on lattice order

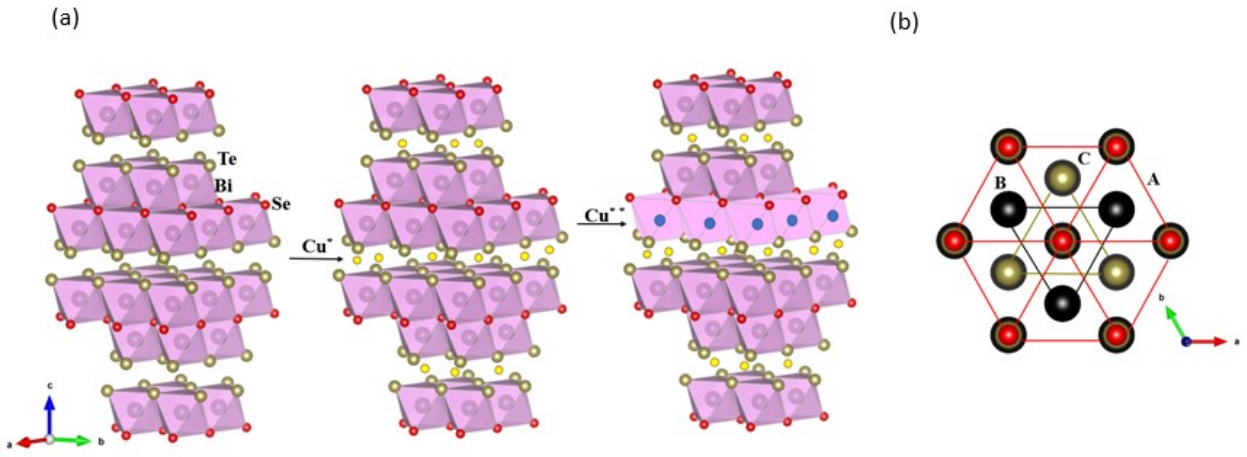

Figure 5.1 Crystal structure. (a) Crystal structure of pure Bi_2Te_2Se (left), Cu intercalated Bi_2Te_2Se (middle) and Cu substituted Bi_2Te_2Se (right), and (b) with ABC stacking image as viewed looking down along the c-axis.

Bi_2Te_2Se has a quintuple layer structure which forms as stacked Te-Bi-Se-Bi-Te, shown in Figure 5.1(a) and 1(b). Five atomic layers are covalently bonded to form the so-called "quintuple layer," while adjacent quintuple layers (QLs) form intercalating spaces bonded via *van der Waals* interactions [159]. Bi_2Te_2Se belongs to the R$\underline{3}$m (D_{3d}^5) space group with a rhombohedral crystal structure. As in the case of Bi_2Se_3 and Bi_2Te_3, introduction of Cu via melt-growth method can result in Cu entering Bi_2Te_2Se as either an intercalant in the *van der Waals* gaps, or as a substitutional defect at Bi sites. As an intercalant, Cu^{1+} acts as a donor. As a Bi-site substituent forming a sigma bond, three Bi 6p electrons are replaced by one Cu 4s electron, resulting in a bi-valent amphoteric (ambipolar) defect.

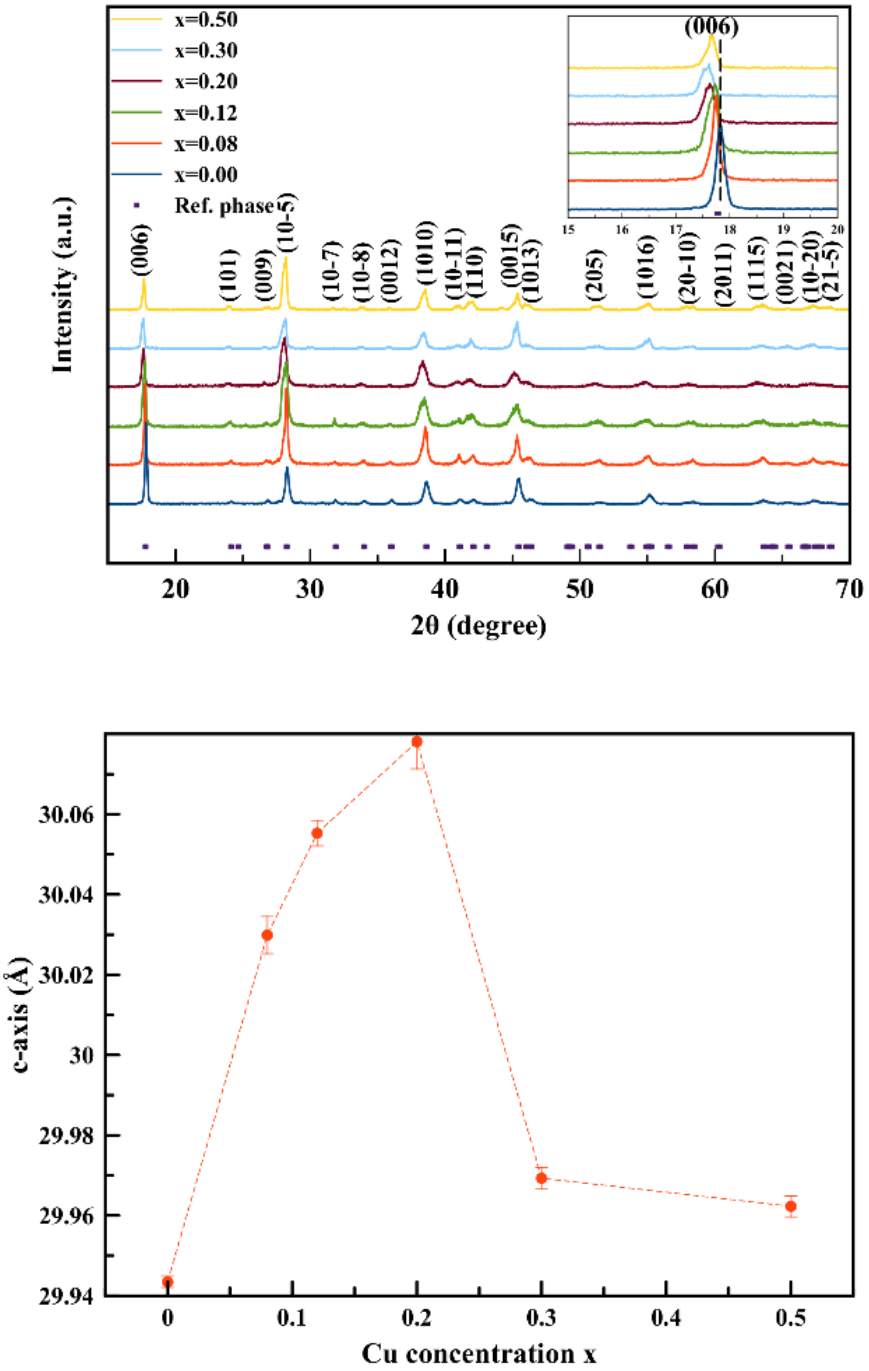

Figure 5.2 (a) Power x-ray Diffraction (XRD) patterns of the as-grown $Cu_xBi_2Te_2Se$ single crystals. Inset: the (006) peak shifting with increasing Cu concentration x (bottom to top, x = 0.00, 0.08, 0.12, 0.2, 0.3 and 0.5); (b) Rietveld refined c-axis values shifting with Cu concentration x.

Figure 5.2 (a) shows results of X-ray Diffraction and analysis on powdered single crystal $Cu_xBi_2Te_2Se$ for x=0.00, 0.08, 0.12, 0.20, 0.3 and 0.50. While the results in Figure 5.2 (b) are from Rietveld refinement of the entire diffractograms, the inset in Figure 5.2 (a) is shown as a visual indication that the (006) reflection follows the c-axis changes as described and reported in Figure 5.2 (b). As seen in Figure 5.2 (a), the c-axis value increases substantially with increasing Cu content, indicating intercalation into the van der Waals gap. Thus, Cu intercalation results in the c-axis increasing from c = 29.94 Å (for x = 0, the parent phase) to c = 30.08Å (for x = 0.2). With higher concentration, x=0.3 and x=0.5, the refinement shows c-axis dropping to 29.97 Å, which we interpret as resulting from a partial substitution at high x values. The tendency for the c-axis to collapse in the $0.2 < x < 0.3$ region is indicative of a tendency to release the stress induced by the lattice expansion due to intercalation, As also discussed for BS and BT [95, 154],Cu in $Cu_xBi_2Se_3$ or $Cu_xBi_2Te_3$ may either intercalate between the Se/Te layers or substitute for Bi within the host structure. Note that, in the case of substitution, a smaller Cu^{2+} ion (ionic radius = 0.72A) replacing a larger Bi^{3+} ion (ionic radius = 1.08A) – instead of intercalating in the van der Waals gaps between the Se/Te layers – can be expected to result in a decrease of the c-axis lattice parameter. In $Cu_xBi_2Te_2Se$, we conclude that most of the Cu has been intercalated into the gap for $x < 0.3$, but that higher Cu levels ($x \geq 0.3$) result in partial Cu substitution at Bi sites.

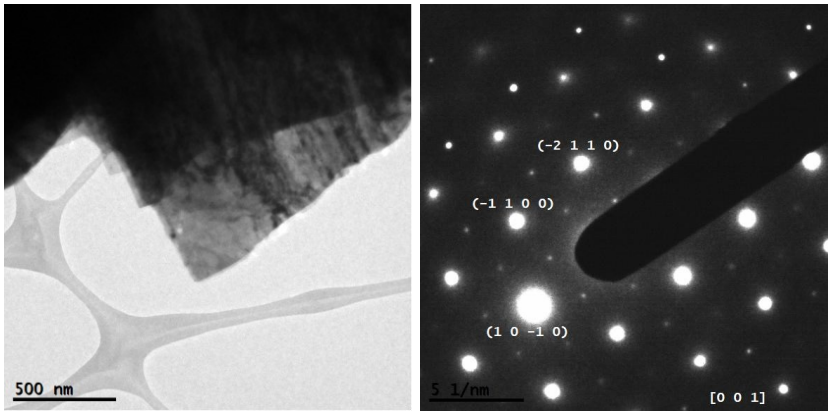

Figure 5.3 Selected Area Electron Diffraction (SAED). (a) bright-field TEM image of an x=0.3 $Cu_xBi_2Te_2Se$ flake, (b) corresponding SAED pattern obtained from the same area in (a).

Transmission Electron Microscopy (TEM) and Selected Area Electron Diffraction (SAED) studies were carried out in order to further assess the crystallinity and morphology of $Cu_xBi_2Te_2Se$ samples. Figure 5.3 is a typical bright-field TEM image (Figure 5.3 (a)) of x=0.3 $Cu_xBi_2Te_2Se$ flake and corresponding SAED pattern (Figure 5.3 (b)) obtained from the same area. As indicated in Figure 5.3 (b), the flake is oriented close to the <001> zone-axis and shows good crystallinity consistent with strong diffraction contrast apparent in the bright-field image of Figure 5.3 (a). Flakes prepared for TEM studies (mechanically ground and dispersed on Lacey-carbon grid) showed large micron-sized regions, and a tendency for a layered morphology, as evident in Figure 5.3 (a). Studies of $Cu_xBi_2Te_2Se$ samples for x = 0, 0.08, 0.12, 0.2, 0.3 and 0.50 were performed. The general results shown in Figure 5.3 (a) are typical of all samples examined. In Figure 5.3 (b), the (100) and (010) reflections, which are kinematically forbidden for ABC stacking in the rhombohedral parent phase of Bi_2Te_2Se [161], are clearly evidence as weak reflections. The appearance of such spots could indicate that either the c-axis ABC stacking sequence symmetry is broken, or that a superlattice ($\sqrt{3}a \times \sqrt{3}a$, $R = 30°$) reconstruction in the

ab-planes is retaining the c-axis stacking order [101]. The intercalated Cu lie mostly in interstitial sites in the van der Waals gap, and it is reasonable to suppose that this effect might cause a disruption of the ABC stacking order and appearance of the kinematically forbidden reflections, as observed and concluded in prior studies of Sn/Fe/Co/Cu intercalated Bi_2Se_3 single crystals [100].

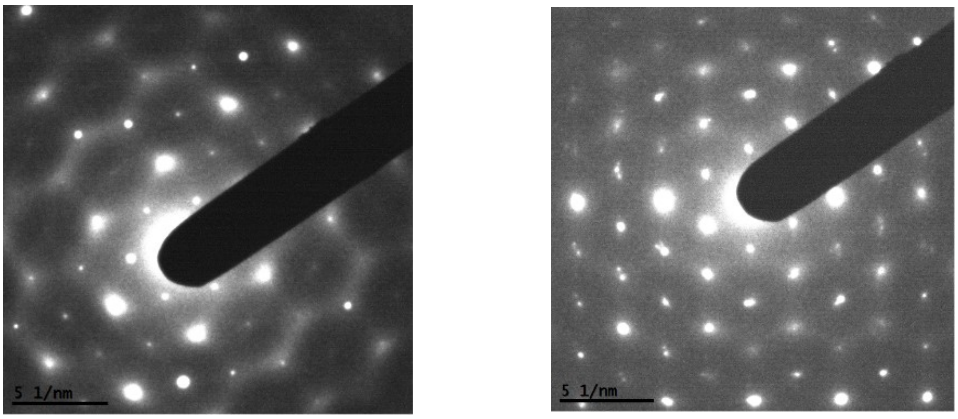

Figure 5.4 SAED patterns recorded slightly tilted off the <001> zone axis for (a) x=0.3 and (b) x=0.0.

It is important to examine whether the forbidden diffraction spots that appear in Figure 5.3 (b) for x=0.3 $Cu_xBi_2Te_2Se$ are due to dynamic scattering, especially considering the strong diffracting conditions of the <001> zone-axis orientation. To address this question, the sample was tilted off the <001> zone-axis in order to reduce dynamical scattering. Figure 5.4 (a) is an SAED pattern obtained from the same region shown in Figure 5.3 (b). In spite of the tilt, the SAED reveals a diffraction pattern clearly associated with the same forbidden reflections. For direct comparison, Figure 5.4 (b) is an SAED pattern from our x=0 $Cu_xBi_2Te_2Se$ sample that is similarly tilted off the <001> zone-axis. However, the forbidden reflections remain. We conclude from this that the pure x=0 sample likely supports some degree of stacking faults based on the layered nature of the material, either intrinsic to the crystal growth method or introduced during TEM sample

preparation through the mechanical grinding steps necessary the reduce the bulk crystal to sufficiently small sizes for TEM studies. In both cases (x=0 and x=0.3) presence of the forbidden (100) and (010) reflections remain comparatively strong when the samples are tilted off the <001> zone-axis with an intent to reduce dynamic scattering effects. This would be the case if the reflections are due to a 2D scattering mechanism where the diffraction spots are rods in reciprocal space and is consistent with the picture of faults in the ABC stacking symmetry.

Note also, in figure 5.4 (a), evidence of diffuse scattering structure in the SAED pattern from the $x = 0.3$ crystal. Similar features are weak or non-existent in figure 5.4 (b), from $x = 0$. The diffuse scattering features shown for the $x = 0.3$ $Cu_xBi_2Te_2Se$ sample (figure 5.4 (a)) appear directly related to Cu content; those features are essentially absent in the pure $x = 0$ sample. Similar diffuse features in SAED patterns have been observed on other layered dichalcogenides where the authors have concluded that the formation of a superlattice at a certain higher temperature foreshadows the possibility of a charge density wave transition (T_{CDW}) at lower temperature [18]. The authors further concluded that the satellite spots above T_{CDW} arise from an incommensurate CDW. We argue below that our SAED observations (performed at room-temperature) are indications of the formation of an induced symmetry-breaking for $x = 0.3$ $Cu_xBi_2Te_2Se$, at the edge of the regimes between intercalation and substitution, and that these results are consistent with the presence of a CDW transition at lower temperature observed in resistivity measurements, and shown in figure 5.6.

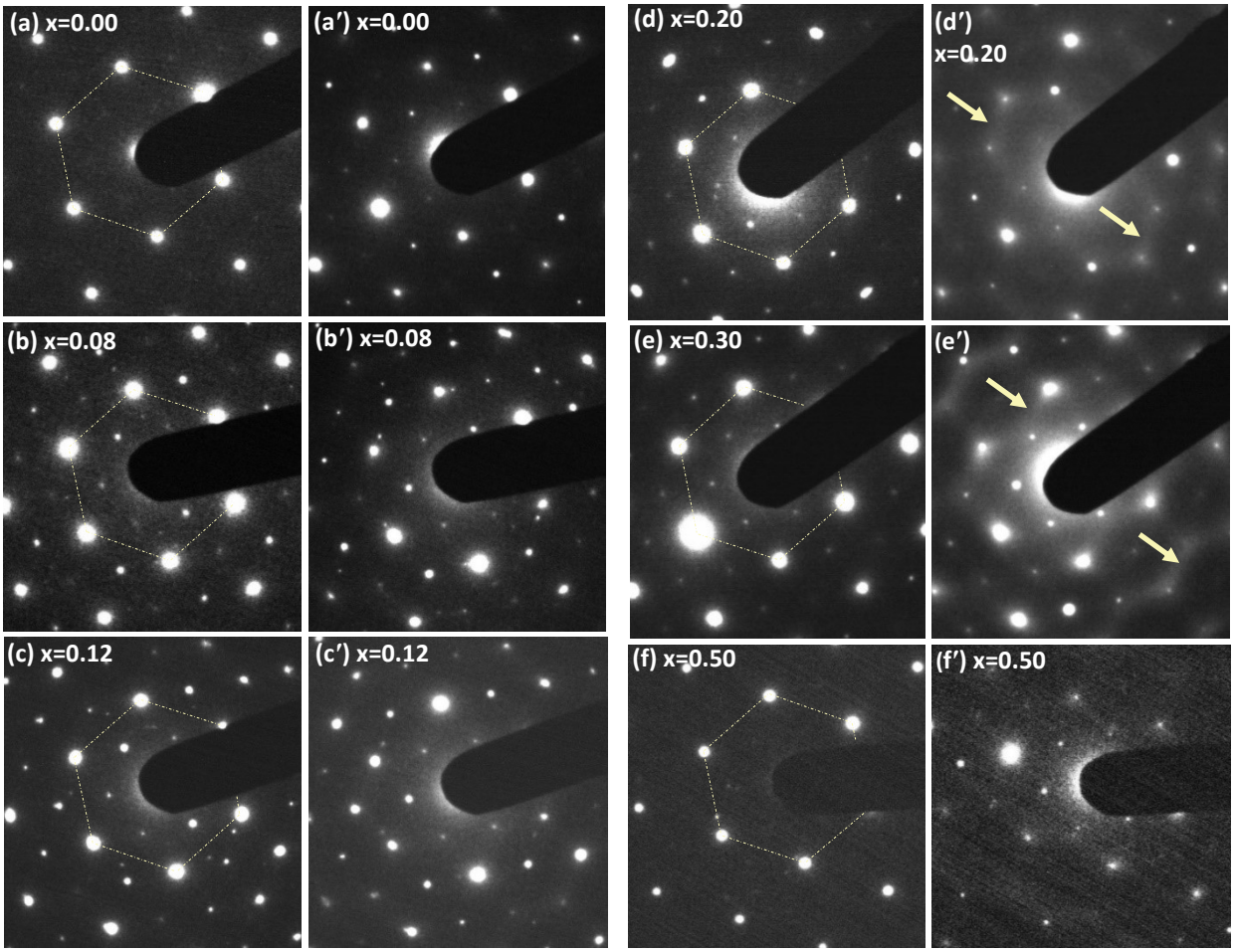

Figure 5.5 Comparison of SAED for as-grown samples (x=0.00 to 0.50)**.** (a)-(f) SEAD recorded close to <001> zone axis, or "on-axis"; (a′)-(f′) same diffraction area and spots as (a)-(f) but slightly tilted off the <001> zone axis, or "off-axis." Yellow arrows indicate streaks (diffuse regions) which intensify for certain values of x. We have optimized contrast to help the reader visualize reflections more clearly.

To further examine the effect of Cu on crystal structure distortion, we show in figure 5.5 our results of SAED studies of $Cu_xBi_2Te_2Se$ samples for x = 0, 0.08, 0.12, 0.2, 0.3 and 0.50. Figure 5.5 (a) through 5.5 (f) are SAED images recorded with the beam aligned closely along the 〈001〉 zone axis ('on-axis'). Figure 5.5 (a') through 5.5 (f') show SAED recorded on the same flake, at the same spot, but with a slight tilt from the 〈001〉 zone axis ('off-axis'). On-axis diffraction patterns (figures 5.5 (a)–(f)) indicate good crystallinity, and confirm that the crystals are, on average,

uniform and well-ordered. Tilting slightly off the zone axis helps minimize the intensity of the Bragg reflections to enable the observation of weak intensities between Bragg reflections. A comparison of the left and right panels in figure 5.5 shows that weak, diffuse intensities show up, off-axis, for all samples. These are especially evident for $x = 0.2$ and $x = 0.3$, and are highlighted with small arrows in yellow. As discussed below, we interpret the observation of weak intensities ('streaks') between Bragg reflections to mean that an incommensurate charge order develops in BTS. We find that the streaks intensify with increasing Cu concentration in the region $0.2 \leq x \leq 0.3$, correlated with distortion and phonon changes observed in the same x region, as shown by figures 5.2 (b), and 5.9 (b) and (c) respectively, serving to help intensify the I-CDW.

A CDW is often found to co-occur with a Periodic Lattice Distortion (PLD) [2,4] such that the periodicity of the CDW is commensurate with the periodicity of the underlying atomic lattice distorted by the PLD. The electronic charge density, a scalar quantity and a natural order parameter of a CDW, is normally assumed to be linearly coupled to the longitudinal PLD, with the ordered CDW period an integral or fractional multiple of the period of the atomic lattice or the PLD. Such a situation could also arise due to planar defects such as stacking faults [162, 163], as is likely to be the case in our samples, given the large changes in lattice constants and phonon frequencies in the $0.2 \leq x \leq 0.3$ region.

Let us now consider the effect of disorder on CDW periodicity such that the periodicity is not represented in the reciprocal lattice by specific vectors $\vec{k}$, but rather one that exists over an entire range of vectors $\vec{k} \pm \Delta\vec{k}$, on either side of $\vec{k}$. This would then lead to diffraction patterns with "diffuse" intensity centered around $\vec{k}$. In the case of large $\Delta\vec{k}$, it is possible to have a scenario in

which diffraction patterns appear as diffuse streaks between Bragg reflections, with the CDW maintaining the overall symmetry of the underlying lattice but not commensurate with the lattice periodicity. This is the basis of the idea of an incommensurate CDW, or I-CDW [164].

In an effort to minimize strain energy, cooling below a certain temperature T_{CDW} could cause an incommensurate CDW (I-CDW) to lock-in to a period commensurate with the period of the lattice or the PLD. Such a transition from an I-CDW to a CDW can be likened to a temperature-driven disorder-to-order transition. An I-CDW, usually observed in diffraction patters as diffuse patterns and streaks, acts as a precursor to a CDW [17-21]. SAED studies of 1T-$TaSe_2$, 2H-$NbSe_2$, 1T-$(Ta_{0.6}Nb_{0.4})S_2$ and 1T-$Ta_xTi_{1-x}S_2$ have shown marked diffuse scattering for $T > T_{CDW}$, but sharp diffraction spots below T_{CDW} [17-21, 164]. In the case of Bi_2Se_3, addition of Cu/Ag/Co/Fe at high concentration yields satellite diffraction spots, interpreted by Koski *et al* to be a signature of an I-CDW [100]. Based on the above, we conclude that in our samples, the observation of an I-CDW at room temperature in Figure 5.5(e′) foreshadows the transition to the CDW observed in Figures 6(a) and 6(b) near 200 K.

Note that some weak diffuse intensity is also seen in other samples, as is clear upon careful examination of Figures 5.5 (b′, c′, d′, e′, j′ and f′) and Figure 5.4(b). The tendency for diffraction intensity arising from an underlying I-CDW seems to be an intrinsic property of the BTS system [163]. Our results point toward Bi_2Te_2Se being intrinsically disordered due to Se/Te dislocation, or due to intercalation by stray Bi atoms inhabiting intercalating spaces [73]. Thus, a weak underlying I-CDW in BTS, already in existence, is enhanced by additional distortions introduced by Cu, as demonstrated in Figures 5.2 and 5.9.

5.2.2 Transport Measurement: charge order for $Cu_{0.3}Bi_2Te_2Se$

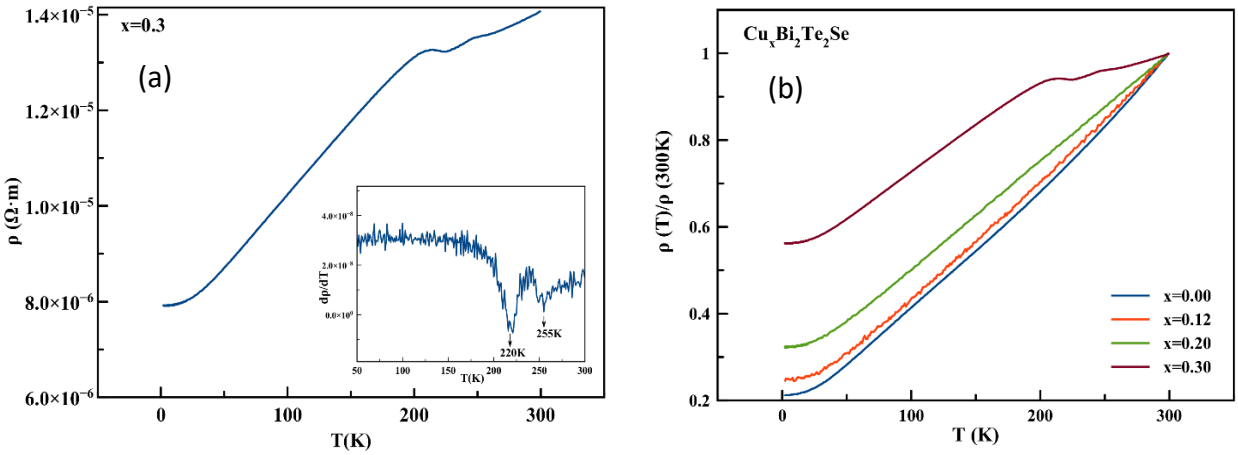

Figure 5.6 (a) Resistivity vs temperature (2 - 300K) on $Cu_{0.3}Bi_2Te_2Se$. Inset: dρ/dT vs T curve enlarged from 50K to 300K. Arrows indicate the minimum point of dρ/dT, indicating a Charge Density Wave (CDW) transition onset temperatures. (b) ρ(T)/ρ(300K) vs temperature (2-300K) for x=0.00, 0.12, 0.20 and 0.30 samples.

Figure 5.6 (a) shows 4-probe resistivity measurements on the x=0.3 single crystal as a function of temperature between 2K and 300K. Note two hump-like features near 220K and 255 K, signaling metal-to-insulator like transitions reminiscent of transitions resulting from a Charge Density wave. The inset to Figure 5.6 (a) shows a plot of dρ/dT as a function of temperature, developing two separate minima near 220K and 255K at the onset of each transition. Figure 5.6 (b) displays ρ(T)/ ρ(300K) as a function of temperature for as-grown single crystal with x=0.00, 0.12, 0.20 and 0.30. Metallic behavior was seen on samples with x=0.00, 0.12 and 0.2. At x = 0.5, excessive Cu doping appears to deteriorate the quality of the crystal as grown. For x = 0.5, we were unable to obtain large enough single crystals for 4-probe resistivity measurements. On the other hand, powder

diffraction SAED, and Raman spectroscopy do not require large crystals; these results are presented in Figures 5.2, 5.5, and 5.9.

5.2.3 Observation of Cu doping effects from XPS and Raman Spectroscopy

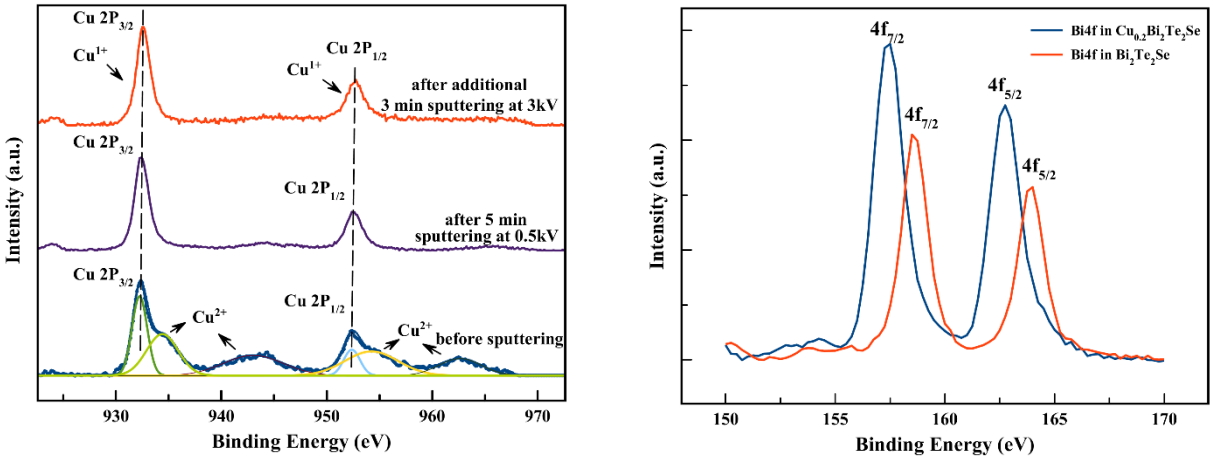

Figure 5.7 High-resolution X-ray Photoelectron Spectra for the orbitals: Cu 2p and Bi 4f. (a) Comparison of Cu 2p for freshly cleaved $Cu_{0.2}Bi_2Te_2Se$ (bottom spectrum), followed by Ar ion gun 0.5kV 5-min surface sputtering (middle spectrum), followed again additional 3kV 3-min sputtering (top spectrum). Before sputtering, both Cu^{1+} and Cu^{2+} are observed on the sample surface. The Cu^{2+} satellite peaks are labeled with arrows. Note that, after sputtering, only Cu^{1+} peaks are left. (b) Comparison of Bi 4f orbitals' shift between Bi_2Te_2Se and $Cu_{0.2}Bi_2Te_2Se$. With Cu intercalation, both $4f_{5/2}$ and $4f_{7/2}$ peaks shift to the left of Bi_2Te_2Se.

One of the questions about integrating Cu into the sample during crystal growth is whether Cu actually intercalates into the van der Waals layers or substitutes into the main lattice. Intercalated Cu has been shown to have oxidation states of either 0 or 1+, whereas substitution into the Bi site would yield Cu^{2+}. Figure 5.7 shows XPS results from the surfaces of x=0.00 and x=0.2 samples, revealing signals from Bi 4f, Te 3d, Se 3d, C 1s and O 1s. Untreated $Cu_xBi_2Te_2Se$ samples show features for both Cu^{1+} and Cu^{2+} oxidation states in Cu 2p. At this stage, it is important to rule out the presence of opportunistic atoms of oxygen which could yield Cu^{2+} due to the formation of CuO. As discussed below, we find clear evidence for the presence of only Cu^{1+} after ablating

approximately 50 nm. from the crystal surface. In Figure 7(a), before sputtering, the $Cu_{0.2}Bi_2Te_2Se$ sample reveals Cu 2p binding Energies (BE) at 932.27 and 952.35eV (corresponding to Cu^{1+}), and at 934.48 and 954.69eV (corresponding to Cu^{2+}) together with two strong satellite peaks [100] which are the characteristics of Cu^{2+}. After 5 minutes of Ar ion sputtering at 0.5kV, the Cu 2p peaks are found to be centered at 932.50 and 952.58eV. Thus, upon ablation, we observe the presence of nearly entirely Cu^{1+}, with the Cu^{2+} feature almost gone, after an additional 3 minutes of 3 kV etching. The binding energy of Cu 2p is at 932.65 and 952.64eV, clearly demonstrating features of the Cu^{1+} oxidation state. This result is consistent with the published literature for the intercalated dichalcogenide $Cu_xBi_2Se_3$ [165, 166].

A comparison of BE for Bi 5d between x=0 and x=0.2 in $Cu_xBi_2Te_2Se$ samples is also shown in Figure 5.7(b), for samples after 0.5kV sputtering. The binding energies of Bi 4f 7/2 and Bi 4f 5/2 in Bi_2Te_2Se (shown in red) are 157.47 eV and 162.78 eV, respectively. A slight shift to a lower BE can be observed for the $Cu_{0.2}Bi_2Te_2Se$ sample (shown in blue). This is further indication of Cu intercalation, in agreement with other reports for $Cu_xBi_2Se_3$ [156]. We conclude from this that, for $0 < x \leq 0.2$, Cu exists in the form of singly ionized interstitial atoms of Cu^{1+} acting as donors and located in the intercalating van der Waals spaces [156, 165]. Note that Cu^{2+} would replace Bi^{3+} sites by creating two holes which act as acceptors [165, 166].

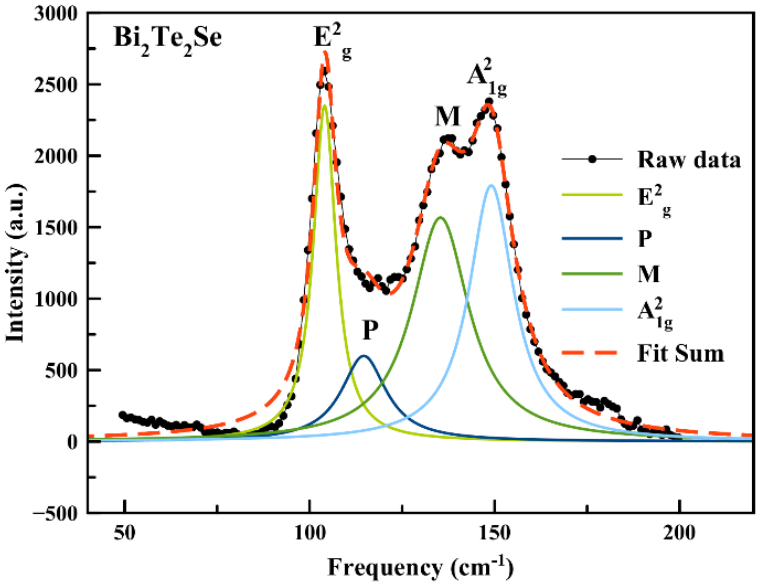

Figure 5.8 Raman spectra of Bi_2Te_2Se taken at room temperature with 10% laser power under a z(xx)$\underline{z}$ polarized configuration. Raw data after baseline subtraction is shown by black dots. Lorentzian functions fitted with four individual modes are labeled as E_g^2, P, M, and A_{1g}^2.

We now examine the effect of Cu on phonon modes in $Cu_xBi_2Te_2Se$. Figure 5.8 displays our results observed on pure (x = 0) Bi_2Te_2Se. Consistent with the literature for Raman modes from Bi_2Te_2Se [160, 167, 168] under z(xx)$\underline{z}$ polarization, we find the A_{1g}^2 mode (149cm^{-1}), the E_g^2 mode (104cm^{-1}), a splitting mode M (135cm^{-1}) of A_{1g}^2, and an extra mode "P" (115cm^{-1}), identified in the literature as possibly arising from E_g^2 mode splitting [160, 167]. Typically, there are four Raman-active modes for Bi_2Te_2Se, A_{1g}^1, A_{1g}^2, E_g^1 and E_g^2, where A_{1g}^1 and E_g^1 show up below 100cm^{-1} [167]. Our filter begins to cut off intensity starting around 100cm^{-1} – thus, our lower frequency modes A_{1g}^1 and E_g^1 (50cm^{-1} to 80cm^{-1}) are indistinguishable from the noise. Our analysis is therefore focused on the behavior of the E_g^2 and A_{1g}^2 modes with varying x. The M mode, previously identified in the literature, is thought to be a local mode arising from Se/Te antisite defects [160, 167, 170]. The so-called P mode (115cm^{-1}) is thought to arise from antisite defects between Te

and Se [160]. In this scenario, Se and Te in $Bi_2Te_{3-x}Se_x$ ($0 \leq x \leq 1$) can randomly replace each other, forming both Bi-Te and Bi-Se bonds [160]. These adjacent Bi-Te and Bi-Se bonds can decouple and lead to two-mode behavior in A_{1g}^2 (resulting in the M mode) and in E_g^2 (resulting in the P mode).

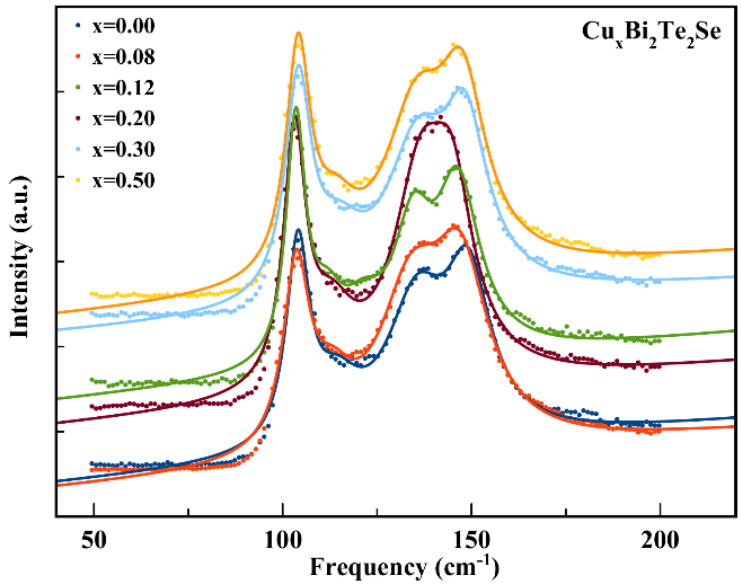

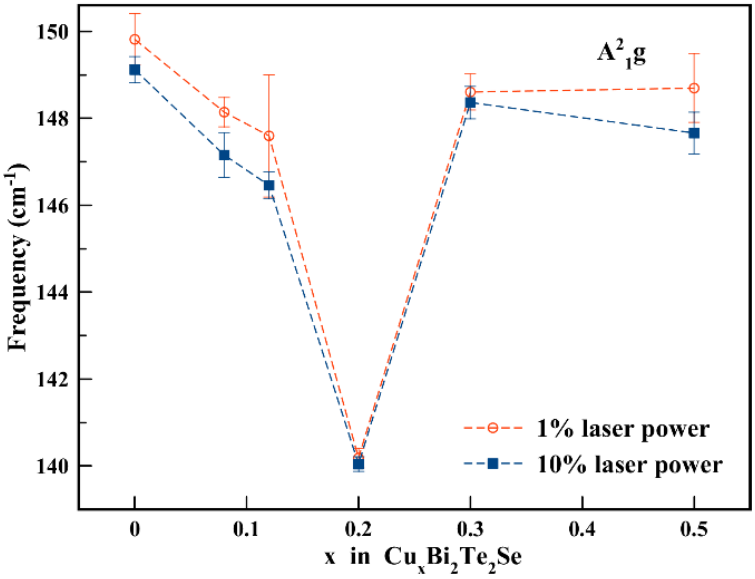

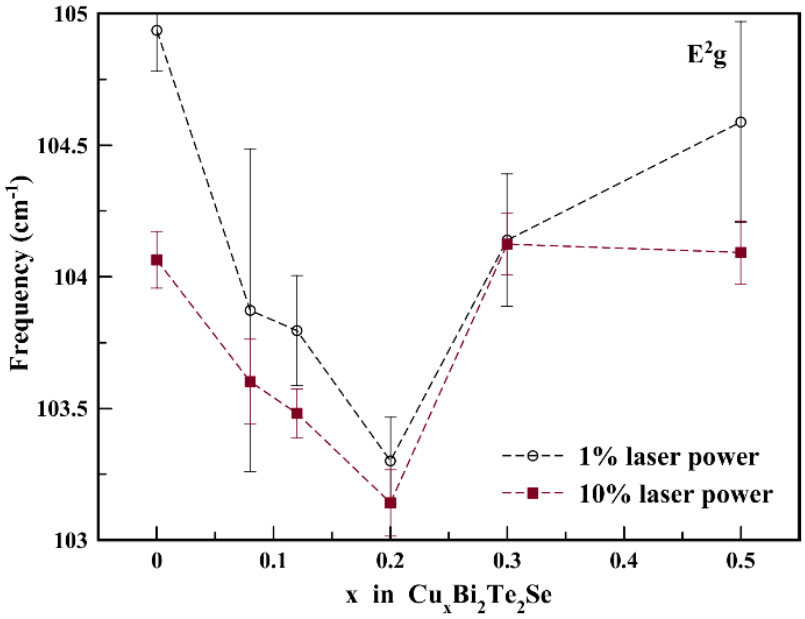

Figure 5.9 Raman spectra under z(xx)z̲ polarization. (a) Raman spectra of $Cu_xBi_2Te_2Se$ (from bottom to top, x=0.00, 0.08, 0.12, 0.2, 0.3 and 0.5) raw data with Lorentzian fit. (b) and (c) are $A^2{}_1g$ and E^2g peak dependence with Cu concentration x; Empty circle and solid square are a comparison of 1% and 10% laser power.

Figure 5.9 (a)-(c) shows the effect of Cu in Bi_2Te_2Se for A_{1g}^2 and E^2g modes. Figure 9(a) is the raw data, shown here together with Lorentzian fits. Figure 5.9(b) and 5.9(c) show the variation of the peak positions of $A_{1g}^2$and E_g^2 with total Cu concentration, x. To examine possible effects of local heating from the focused laser, Raman spectra were measured at both 1% power (0.0875 mW/μm^2) and 10% power (0.875 mW/μm^2), separately. As shown in Figure 5.9 (b) and 5.9 (c), peak shifts for the two different laser power settings were within each other's error bars. In Figure 9(b) and 9(c), $A_{1g}^2$and E_g^2 phonons clearly soften with increasing Cu concentration between x=0.0 and x=0.2. However, with higher Cu concentration, of x=0.3 and x=0.5, we observe a hardening of the A_{1g}^2 and E_g^2 phonon modes, together with a broadening of the peak widths. Previous reports have ascribed similar softening versus hardening of A_{1g} and E_g modes to intercalation and

substitution [172, 173]. Chen et al [173] conclude that the A_{1g}^1 mode in Bi_2Se_3 shifts to lower frequency with increasing Cu intercalation. In contrast, substitution of lighter atoms at the Bi site has been found to result in A_{1g}^1, A_{1g}^2, E_g^1 and E_g^2 modes shifting to higher frequency [160, 172].

We could try to understand this as follows. When Cu enters as an intercalant between two quintuple layers (QL), each QL experiences an extra Coulomb force resulting from the Cu in the van der Waals spaces [95, 156, 173]. This Coulomb interaction can modify bond-lengths and structure of the QL, thus affecting the phonon vibrational frequency. The hardening of phonon modes for $x \geq 0.3$, compared with lower $x \leq 0.2$, is in reasonable agreement with our XRD results. In other words, lower Cu concentrations lead to Cu intercalation whereas higher Cu concentrations can lead to partial substitution of Cu^{2+} to Bi^{3+}. The increase in peak width for x=0.3 and x=0.5 is likely due to additional disorder introduced by the Cu intercalant when it substitutes into the Bi_2Te_2Se host structure [174]. We conclude from this that Cu incorporation in $Cu_xBi_2Te_2Se$ primarily occurs as an intercalant at low concentrations, as indicated by phonon modes shifting to lower frequencies when compared to pure Bi_2Te_2Se. At higher concentrations, Cu incorporates as a substituent, as indicated by phonon modes shifting to higher frequencies.

5.3 Origin of the charge order

We now return to discuss the origin of the CDW observed in $Cu_{0.3}Bi_2Te_2Se$. A typical CDW phase transition is accompanied by the opening of a gap at the Fermi level, resulting in a metal-to-insulator like transition in resistivity as a function of temperature. In most microscopic models, a CDW transition is understood as being driven by either an electron energy instability near the Fermi level, or due to Fermi nesting [16, 33, 175]. Most commonly, CDW phase transitions are

observed in 1D chains [47], or in 2D layered di-chalcogenide materials [54]. In practice, single crystals with *imperfect chains* (quasi-1D), or *imperfect nestings* (quasi-2D), can lead to such an energy gap being partially opened. This is more often seen as a metal-to-semimetal transition similar to our observations in Figure 6 in our data, and as also observed in multiple other systems [176, 177]. The CDW transition observed here in $Cu_{0.3}Bi_2Te_2Se$ is likely to be related to the nature of the quintuple layers in this material. As seen from X-ray diffraction, increasing Cu concentration lengthens the c-axis. The crystal lattice is likely to respond to this by forming new periodic structures, which we observe as a superlattice in electron diffraction results from our crystals. The lattice might also respond by creating stacking faults, or other disorder types, helping reveal forbidden reflections in the ABC stacking which we observe. At this point, it is difficult to tease out whether the forbidden reflections arise from a superlattice, or from other types of disorder. Based on the fact that the reflections are retained when the crystals are tilted from the (001) zone axis, we conclude that the forbidden reflections do not arise from dynamic scattering. Thus, a *periodic lattice distortion* (PLD), such as the ones described above, is often accompanied by a charge density wave (CDW) [4, 175, 178]. The "fundamental origin" question, of whether an electronic modulation causes a structural modulation, or vice versa, is still being debated in the current literature [4, 164, 178, 179]. We have demonstrated here the presence of both a possible PLD and a CDW in $Cu_xBi_2Te_2Se$, without commenting upon which one leads to the other.

The presence of diffuse scattering in Figure 5(e′) is clearly indicative of charge ordering. Most authors interpret such intensities in electron diffraction as arising from the formation of an incommensurate charge density wave (I-CDW). The combined observation of an incommensurate CDW in SAED at room temperature, together with the transitions observed in resistivity near 220-

225 K, indicate that the feature in resistivity is a transition from an I-CDW to a (possible) CDW phase below 220 K. Rossnagel provides a review of both theoretical and experimental results for a series of dichalcogenides [4], and uses existing data to indicate that the physical picture provided by the Peierls model is likely to be correct for systems such as 1T-TaS_2, 2H-TaS_2 and 1T-$TiSe_2$. An incommensurate CDW/PLD is mostly associated with long coherence length, small energy gap and weak electron-phonon coupling. Such a transition is driven by an instability of the Fermi surface, such as in 2H-TaS_2 [18]. On the other hand, in the strong-coupling regime, a CDW shows up with short coherence, and a large energy gap. The latter case is driven by an ionic-covalent bonding picture similar to the case in 1T-TiS_2 [180]. In the broader picture, however, it has not been easy to determine a strong dominant driving force for the origin of CDWs in layered materials: strong electron-coupling and an appropriate density of states near the Fermi level certainly seem to be important. Further work is needed in order to tease-out the details of the origin of CDW in these materials, and the possible discovery of ground states such as superconductivity.

5.4 Experimental methods

Single crystals of $Cu_xBi_2Te_2Se$ (x=0, 0.08, 0.12, 0.15, 0.2, 0.3, 0.5) were prepared by melting high-purity (99.999%) powders of Bi, Te, Se and Cu in stoichiometric ratios. Stoichiometric mixtures of 2.5g batches were sealed into high-quality quartz tubes in vacuum after being weighed and sealed in an inert glove box, taking care to never expose to air. The crystals were grown from a melt using a two-step process. The mixtures in sealed quartz tubes were heated up to 850 C and maintained at that temperature for 48 hours. They were then cooled to 450 C at 0.1 C/min, followed by cooling to room temperature at 0.8 C/min. The tubes were subsequently re-sealed in inert

atmosphere and re-annealed at 600 C for two weeks, before being quenched into tap water at room temperature, yielding high-quality single crystals.

Powder X-ray Diffraction (XRD) measurements were performed using a Bruker D8 Discover x-ray diffractometer with Cu Kα radiation. Powder X-ray diffraction data were collected from pieces of single crystals powdered inside an inert glove box. Rietveld refinement was performed using GSAS (General Structure Analysis System) and the EXPGUI interface. Raman spectroscopy measurements were performed on a Renishaw Inc. 1000B, 1800 grating Raman spectrometer equipped with a microscope. Samples were measured at room temperature using an excitation wavelength of 632 nm through a 20x microscope objective lens, resulting in a laser spot of 4 μm^2 with power of 35mW at 100%. Data presented here were collected using 1% power (0.0875 mW/ $\mu m^2$and 10% power (0.875 mW/ μm^2), while keeping the same microscope objective and laser spot size. The polarization configuration used in our measurements was: $Z(XX)\underline{Z}$. Phonon peaks were fitted as Lorentzian functions.

X-ray Photoelectron Spectroscopy (XPS) was performed in a Perkin Elemer PHI 5440 ESCA System in ultra-high vacuum, with an Mg anode source. Surfaces were prepared by cleaving the crystal surface in inert atmosphere. However, we believe that the transfer process resulted in some exposure to air. For this reason, we studied Cu oxidation state using depth profiling by ablating with an Ar-ion gun. XPS was then used to study the oxidation state of Cu with increasing ablation of the top layer. XPS spectra peaks up to a binding energy of 1000 eV were fitted using a Lorentzian fitting function convolved with a Gaussian after subtracting baseline. Selected Area

Diffraction (SAED) was performed at room temperature with a Hitachi H-9000NAR high resolution transmission electron microscope (HRTEM) operated at 300kV. Crystals of $Cu_xBi_2Te_2Se$ (x= 0, 0.12, and 0.3) were mechanically ground and dispersed on Lacey-carbon grid. Variable temperature resistivity studies were performed using 4-probe silver paste contacts on single crystals placed in a Quantum Design Physical Property Measurement System (PPMS).

5.5 Conclusions

In summary, we used a self-flux method to grow single crystals of $Cu_xBi_2Te_2Se$ and examined the effect of Cu on crystal structure, phonon and electron properties. X-ray photoelectron studies show that Cu exists in the intercalating spaces as Cu^{1+}. Increasing Cu concentration leads to an increase in the c-axis length up to x=0.2. Beyond x=0.2, the c-axis drops to lower values. Similarly, Raman modes A_{1g}^2 and E^2g soften up to x=0.2 and harden for higher values of Cu. This points to the possibility that, while lower concentrations of Cu for $x \leq 0.2$ end up with Cu in the intercalating spaces, higher concentrations end up as substituents. This conclusion is consistent with previous observations in $Cu_xBi_2Se_3$, and also makes the $0.2 \leq x \leq 0.3$ region in the $Cu_xBi_2Te_2Se$ phase diagram a region of much interest due to the presence of possible instabilities and distortions. The observation of a charge density wave (CDW) transition in the x=0.3 sample is therefore interesting. In particular, $Cu_{0.3}Bi_2Te_2Se$ reveals diffuse order in electron diffraction together with CDW-like transitions in resistivity near 220 K. In addition, we also find the existence of reflections forbidden by ABC stacking. These are indicative of a periodic lattice distortion (PLD), often observed as harbingers of a CDW transition in other layered di-chalcogenides. Our work provides strong indications that the Cu-intercalated ternary chalcogenide $Cu_{0.3}Bi_2Te_2Se$, upon cooling below

220K, undergoes a transition from an incommensurate charge density wave (I-CDW) to a charge density wave (CDW) state. Further work is needed, with temperature-dependent electron diffraction, in order to confirm this. Additionally, it is important to study this system further in order to uncover the possibility that an incommensurate CDW with a weak electron-phonon coupling could eventually lead to the discovery of superconductivity in $Cu_xBi_2Te_2Se$.

REFERENCES

[1] Grüner, G. “Density Waves in Solids,” Frontiers in Physics Ed D. Pines (Addison-Wesley) 1994 and Rev. Mod. 60, 1129, 1988.

[2] Grüner, G. The dynamics of charge-density waves. Rev. Mod. Phys. 60, 1129-undefined (1988).

[3] Frölich, H. Proc. R. Soc. London A223, 296, (1954).

[4] Rossnagel, K. On the origin of charge-density waves in select layered transition-metal dichalcogenides. J. Condens. Matter Phys. 23, (2011).

[5] Wilson, J. A., Salvo, F. J. di & Mahajan, S. Charge-Density Waves in Metallic, Layered, Transition-Metal Dichalcogenides. Phys. Rev. Lett. 32, 16 (1974).

[6] Moll, P., Zeng, B., Balicas, L. et al. Field-induced density wave in the heavy-fermion compound $CeRhIn_5$. Nat Commun 6, 6663 (2015).

[7] Gruner, T., Jang, D., Huesges, Z. et al. Charge density wave quantum critical point with strong enhancement of superconductivity. Nature

[8] Peierls, R. Quantum Theory of Solids, Oxford University Press, New York, 1955.

[9] Comès, R.; Lambert, M.; Launois, H.; Zeller, H.R. Evidence for a Peierls Distortion or a Kohn Anomaly in One-Dimensional Conductors of the Type $K_2Pt(CN)_4Br_{0.3}\cdot 3H_2O$. Phys. Rev. B 8, (1973).

[10] Candolfi, C.Coexistence of a charge density wave and superconductivity in the cluster compound $K_2Mo_{15}Se_{19}$. Phys. Rev. B 101, (2020)

[11] Isobe, H., Yuan, N. F. Q. & Fu, L. Unconventional Superconductivity and Density Waves in Twisted Bilayer Graphene. Phys. Rev. X 8, (2018).

[12] Cho, D. N., Brink, J. van den, Fehske, H., Becker, K. W. & Sykora, S. Unconventional superconductivity and interaction induced Fermi surface reconstruction in the two-dimensional Edwards model. Sci. Rep. 6, (2016).

[13] Lee, S. et al. Unconventional charge density wave order in the pnictide superconductor $Ba(Ni_{1-x}Co_x)_2As_2$. Phys. Rev. Lett. 122, (2019).

[14] Miclea C F, Hochheimer H D, Dorhout P K, Martin B and Sparn G. J. Magn. Magn. Mater. 272–276 (2004)

[15] Li, L. et al. Superconducting order from disorder in 2H-TaSe 2- x S x. npj Quantum Materials 2, (2017).

[16] Chen, C., Choe, J. & Morosan, E., Charge density waves in strongly correlated electron systems. Rep. Prog. Phys. 79, 084505 (2016).

[17] Wilson, J. A., Disalvo, F. J. and Mahajan S. Charge-density waves and superlattices in metallic layered transition-metal dichalcogenides. Adv. Phys. 24, (1975)

[18] Wilson, J. A, Di Salvo F. J. and Mahajan S. Charge-density waves in metallic, layered, transition-metal dichalcogenides. Phys. Revs. Lett. 32, (1974)

[19] Williams, P. M., Scruby C., Clark, W. and Parry, G. Charge density waves in the layered transition metal dichalcogenides J. Phys. Colloques. 37, C4-139–150 (1976)

[20] McMillan, W. L. Landau theory of charge-density waves in transtion-metal dichalcogenides Phys. Rev. B 12 1187 (1975)

[21] DiSalvo, F. J. & Maurice Rice T. Charge-density waves in transition-metal compounds Phys. Today 32, (1979)

[22] Inagaki, K. and Tanda, S. Lock-in transition of charge density waves in quasi-one-dimensional conductors: Reinterpretation of McMillan's theory, Phys. Rev. B 97, 115432 (2018)

[23] McMillan, W. L. Landau theory of charge-density waves in transition-metal dichalcogenides, Phys. Rev. B 12, 1187 (1975)

[24] Samnakay,R., Wickramaratne,D., Pope,T. R., Lake,R. K, Salguero, T. T. and Balandin, A. A. Zone-Folded Phonons and the Commensurate–Incommensurate Charge-Density-Wave Transition in 1T-TaSe2 Thin Films, Nano Lett. 15(5), (2015)

[25] Jaeger, G. The Ehrenfest Classification of Phase Transitions: Introduction and Evolution. Arch Hist Exact Sc. 53, 51–81 (1998).

[26] Welsch, J. et al. Second-order charge-density-wave transition in single crystals of $La_3Co_4Sn_{13}$. Phys. Rev. Materials 3, 125003 (2019)

[27] McMillan, W. L. Theory of discommensurations and the commensurate-incommensurate charge-density-wave phase transition. Phys. Rev. B 14, 1496–1502 (1976)

[28] Koski, K J, Cha J J, Reed B W, Wessells C D, Kong, D, and Cu, Y. High-Density Chemical Intercalation of Zero-Valent Copper into Bi_2Se_3 Nanoribbons. J. Am. Chem. Soc. 134, 7584–7587 (2012)

[29] Choi, K. S. et al. Charge Density Wave Caused by Reducing $ThSe_3$ by One Electron. Superstructure and Short-Range Order in ATh_2Se_6 (A = K, Rb) Studied by X-ray Diffraction, Electron Diffraction, and Diffuse Scattering. Am. Chem. Soc. 120, 41, 10706–10714 (1998)

[30] Zong, A. et al. Ultrafast manipulation of mirror domain walls in a charge density wave. Sci. Adv. 4, 5501 (2018).

[31] Fan, G., Zhang, X., Shi, Y. et al. Charge density wave transition in $Na_2Ti_2Sb_2O$ probed by ^{23}Na NMR. Sci. China Phys. Mech. Astron. 56, 2399–2403 (2013)

[32] Wilson, Douglas M. (Douglas Mark), PhD thesis, 2017, Florida State University

[33] Zhu, X., Cao, Y., Zhang, J., Plummer, E. W. & Guo, J. Classification of charge density waves based on their nature. Proc. Natl Acad. Sci. USA 112, 2367–2371 (2015)

[34] Zhu, X., Guo, J., Zhang, J., Plummer, E.W. Misconceptions associated with the origin of charge density waves. Advances in Physics: X, 2, (2017)

[35] Mihaila, B. Lindhard function of a d-dimensional Fermi gas. arXiv: Quantum Gases. (2011).

[36] Zheng, W., Xie, T., Zhou, Y. et al. Patterning two-dimensional chalcogenide crystals of Bi_2Se_3 and In_2Se_3 and efficient photodetectors. Nat Commun 6, 6972 (2015).

[37] Moncton D. E., Axe J. D. & DiSalvo F. J. Study of Superlattice Formation in 2H-NbSe2 and 2H-$TaSe_2$ by Neutron Scattering. Phys. Rev. Lett. 34, (1975).

[38] Wilson, J. A. & Yoffe, A. D. The transition metal dichalcogenides discussion and interpretation of the observed optical, electrical and structural properties. Adv. Phys. 18, 193–335 (1969).

[39] Mattheiss, L. F. Band Structures of Transition-Metal-Dichalcogenide Layer Compounds. Phys. Rev. B 8, 3719 (1973)

[40] Harper, J. M., Geballe, T. E. & Disalvo, F. J. Thermal properties of layered transition-metal dichalcogenides at charge-density-wave transitions. Phys. Rev. B 15, 2943–2951 (1977).

[41] Fang, L. et al. Fabrication and superconductivity of $NaxTaS_2$ crystals,Phys. Rev. B 72, 014534

[42] Suderow, H., Tissen, V. G., Brison, J. P., Martínez, J. L. & Vieira, S. Pressure induced effects on the Fermi surface of superconducting 2H-$NbSe_2$. Phys. Rev. Lett. 95, 117006 (2005).

[43]Yomo, R., Yamaya, K., Abliz, N., Hedo, M. & Uwatoko, Y. Pressure effect on competition between charge density wave and superconductivity in ZrTe3: appearance of pressure-induced reentrant superconductivity. Phys. Rev. B. 71, 132508 (2005).

[44] Zhu, X., Lei, H. & Petrovic, C. Coexistence of bulk superconductivity and charge density wave in Cu_xZrTe_3. Phys. Rev. Lett. 106, 246404 (2011).

[45] Lei, H., Zhu, X. & Petrovic, C. Raising T_c in charge density wave superconductor $ZrTe_3$ by Ni intercalation. EPL. 95, 17011 (2011).

[46] Zhu, X. et al. Superconductivity and Charge Density Wave in $ZrTe_{3-x}Se_x$. Sci. Rep. 6, 26974 (2016).

[47] Straub, T. et al. Charge-density-wave mechanism in 2H−$NbSe_2$: photoemission results. Phys. Rev. Lett. 82, 4504–4507 (1999).

[48] Harper, J., Geballe, T. & Salvo, F. D. Heat capacity of 2H-$NbSe_2$ at the charge density wave transition. Phys. Lett. A 54, 27–28 (1975).

[49] Yang, J. J. et al. Charge-Orbital Density Wave and Superconductivity in the Strong Spin-Orbit Coupled $IrTe_2$:Pd. Phys. Rev. Lett. 108, 116402, (2012).

[50] Sangeetha, N. S. et al. Interplay of superconductivity and charge density wave ordering in pseudoternary alloy compounds: $Lu_2Ir_3(Si_{1-x}Ge_x)_5$, $Lu_2(Ir_{1-x}Rh_x)_3Si_5$, and $(Lu_{1-x}Sc_x)_2Ir_3Si_5$. Phys. Rev. B 86, 024524 (2012)

[51] Kiss, T. et al. Charge-order-maximized momentum-dependent superconductivity. Nature Phys 3, 720–725 (2007).

[52] Cho, K. et al. Using controlled disorder to probe the interplay between charge order and superconductivity in $NbSe_2$. Nat Commun 9, 2796 (2018).

[53] Wang, B. et al. Universal phase diagram of superconductivity and charge density wave versus high hydrostatic pressure in pure and Se-doped $1T-TaS_2$. Phys. Rev. B 97, 220504(R) (2018)

[54] Monceau, P. et al., Phys. Rev. Lett. 39, 161 (1977).

[55] Denholme, S., Yukawa, A., Tsumura, K. et al. Coexistence of superconductivity and charge-density wave in the quasi-one-dimensional material $HfTe_3$. Sci Rep 7, 45217 (2017).

[56] Takahashi, S., Sambongi, T., Brill, J. W. & Roark, W. Transport and elastic anomalies in $ZrTe_3$. Solid State Comm. 49, 1031–1033 (1984).

[57] Zhang, X. et al Superconductivity in large spin-orbit coupled material $IrTe_2$, J. Phys. Chem. Solids. 128, (2019)

[58] Society, P. & April, R. "Topological Insulator Materials," J. Phys. Soc. Jpn 82, 102001 (2013).

[59] Moore, J. The birth of topological insulators. Nature 464, 194–198 (2010).

[60] Qi, X. L. & Zhang, S. C. Topological insulators and superconductors. Rev. Mod. Phys. 83, 1057–1110 (2011).

[61] Hasan, M. Z. & Kane,C. L. Colloquium: Topological insulators. Rev. Mod. Phys. 82, 3045 (2010)

[62] Zhang, H. et al. Topological insulators in Bi_2Se_3, Bi_2Te_3 and Sb_2Te_3 with a single Dirac cone on the surface. Nature Phys 5, 438–442 (2009).

[63] Cava, R. J., Ji, H., Fuccillo, M. K., Gibson, Q. D. & Hor, Y. S. Crystal structure and chemistry of topological insulators. *J. Mater. Chem. C* **1**, 3176–3189 (2013)

[64] Ren Z, Taskin A A, Sasaki S, Segawa K and Ando Y. Large bulk resistivity and surface quantum oscillations in the topological insulator Bi_2Te_2Se. Phys. Rev. B 82, 241306 (2010)

[65] Unzueta, I. et al. Observation of a charge delocalization from Se vacancies in Bi_2Se_3: A positron annihilation study of native defects. Phys. Rev. B 94, 014117 (2016)

[66] Hashibon A. & Elsässer, C. First-principles density functional theory study of native point defects in Bi_2Te_3. Phys. Rev. B 84, 144117 (2011)

[67] Zhang, W. et al. First-principles studies of the three-dimensional strong topological insulators Bi_2Te_3, Bi_2Se_3 and Sb_2Te_3. New J. Phys. 12 065013 (2010)

[68] Kuroda, K. et al. Hexagonally Deformed Fermi Surface of the 3D Topological Insulator Bi_2Se_3. Phys. Rev. Lett. 105, 076802 (2010).

[69] Fu, L. Hexagonal Warping Effects in the Surface States of the Topological Insulator Bi_2Te_3. Phys. Rev. Lett.103, 266801 (2009).

[70] Li, Y. et al. arXiv: 2002.12546.

[71] R.J. Cava, H. Ji, M.K. Fuccillo, Q.D. Gibson, Y.S. Horb, J. Mater. Chem. C 2013, Advance Article, DOI: 10.1039/C3TC00587A.

[72] Kanatzidis, M. G. Nanostructured thermoelectrics: the new paradigm? Chem. Mater. 22, 648–659 (2010)

[73] Huang, F.-T. et al. Nonstoichiometric doping and Bi antisite defect in single crystal Bi_2Se_3. Phys. Rev. B 86, 081104(R) (2012).

[74] Fleurial, J. et al. J. Phys. Chem. Solids 49, (1988).

[75] Fuccillo, M., Jia, S., Charles, M. et al. Thermoelectric Properties of Bi_2Te_2Se Compensated by Native Defects and Sn Doping. Journal of Elec Materi 42, 1246–1253 (2013).

[76] Li, Y., Smith, N. P., Rexhausen, W., Schofield, M. A. & Guptasarma, P. Possible lattice and charge order in $Cu_xBi_2Te_2Se$. J. Phys. Mater. 3 015008 (2020)

[77] Nobel, J. d. and Lindenfeld ,P. “The Discovery of Superconductivity,” Physics Today 49, (1996).

[78] Bardeen, J., Cooper, L. N. & Schrieffer, J. R. Theory of superconductivity. Phys. Rev. 108, 1175–1204 (1957).

[79] Cooper, L. "Bound Electron Pairs in a Degenerate Fermi Gas". Phys. Rev. 104 (4): 1189–1190 (1956).

[80] Kittel, C., 1971, Introduction to Solid State Physics, publisher Wiley

[81] Stewart, G. R. Unconventional superconductivity. Adv. Phys. 6, 75–196 (2017).

[82] Sato M and Ando Y 2017 Topological superconductors: a review Rep. Prog. Phys. 80 076501

[83] Leijnse M & Flensberg K . Introduction to topological superconductivity and Majorana fermions. Semicond Sci Technol 27, (2012).

[84] Sarma, S., Freedman, M. & Nayak, C. Majorana zero modes and topological quantum computation. npj Quantum Inf 1, 15001 (2015).

[85]Das Sarma S, Freedman M, Nayak C . Topological quantum computation. Phys Today 59, (2006).

[86] Yonezawa, S. arxiv:1604.07930

[87] Sasaki, S. et al. Topological superconductivity in $Cu_xBi_2Se_3$. Physical Review Letters 107, (2011).

[88] Asaba, T. et al. Rotational symmetry breaking in a trigonal superconductor Nb-doped Bi2Se3. Phys. Rev. X 7, (2017).

[89] Shruti, Maurya, V. K., Neha, P., Srivastava, P. & Patnaik, S. Superconductivity by Sr intercalation in the layered topological insulator Bi_2Se_3. Phys. Rev. B 92, 020506(R) (2015).

[90] Shen, J. et al. Nematic topological superconducting phase in Nb-doped Bi2Se3. npj Quantum Materials 2, (2017).

[91] Fu, L.& Berg, E. Odd-Parity Topological Superconductors: Theory and Application to $Cu_xBi_2Se_3$. Phys. Rev. Lett. 2010, 105, 097001.

[93] Yonezawa, S. Nematic superconductivity in doped Bi_2Se_3 topological superconductors. Condens. Matter 4, 2 (2019).

[94] Hecker, M. & Schmalian, J. Vestigial nematic order and superconductivity in the doped topological insulator $Cu_xBi_2Se_3$. npj Quantum Materials 3, (2018).

[95] Hor, Y. S. et al. Superconductivity in $Cu_xBi_2Se_3$ and its implications for pairing in the undoped topological insulator. Phys. Rev. Lett. 104, 057001 (2010).

[96] Schneeloch, J. A., Zhong, R. D., Xu, Z. J., Gu, G. D. & Tranquada, J. M. Dependence of superconductivity in CuxBi2Se3 on quenching conditions. Phys. Rev. B 91, (2015).

[97]Matano, K.; Kriener, M.; Segawa, K.; Ando, Y.; Zheng, G.-Q. Spin-rotation symmetry breaking in the superconducting state of $Cu_xBi_2Se_3$. Nat. Phys. 12, (2016).

[98]Yonezawa, S.; Tajiri, K.; Nakata, S.; Nagai, Y.; Wang, Z.; Segawa, K.; Ando, Y.; Maeno, Y. Thermodynamic evidence for nematic superconductivity in $Cu_xBi_2Se_3$. Nat. Phys. 13, (2017)

[99] Pan, Y.; Nikitin, A.M.; Araizi, G.K.; Huang, Y.K.; Matsushita, Y.; Naka, T.; de Visser, A. Rotational symmetry breaking in the topological superconductor $Sr_xBi_2Se_3$ probed by upper-critical field experiments. Sci. Rep. 6, (2016)

[100] Wan, X. & Savrasov, S. Y. Turning a band insulator into an exotic superconductor. Nat Commun 5, (2014).

[101] Wang, J. et al. Evidence for singular-phonon-induced nematic superconductivity in a topological superconductor candidate $Sr_{0.1}Bi_2Se_3$. Nat Commun 10, (2019).

[102] Lahoud, E. et al. Evolution of the Fermi surface of a doped topological insulator with carrier concentration. Phys. Rev. B Condens. Matter 88, (2013).

[103] Fu, L. Hexagonal warping effects in the surface states of the topological insulator Bi_2Te_3. Physical Review Letters 103, (2009).

[104] Levitt, M. H. Spin Dynamics: Basics of Nuclear Magnetic Resonance. John Wiley and Sons, England, 2001.

[105] Slichter, C. P. Principles of Magnetic Resonance. Springer, Heidelberg, 1990.

[106] Lumata, L. L. (Lloyd Laporca), PhD thesis, Spin Dynamics of Density Wave and Frustrated Spin Systems Probed by Nuclear Magnetic Resonance, Florida State University, 2008.

[107] Wilson, D. M. (Douglas Mark) PhD thesis, NMR Investigation of the Layered Superconductor $NbSe_2$, Florida State University, 2017.

[108] Guehne, R. Unusual ^{209}Bi NMR quadrupole effects in topological insulator Bi_2Se_3. *JMR* 302, 34-42 (2019).

[109] R. J. Darton, P. Wormald and R. E. Morris, J. Mater. Chem., 2004, 14, 2036–2040.

[110] Berthier, C. & Segranson, P.: inLow Dimensional Conductors and Superconductors, ed. D.Jérome and L. G.Caron (Plenum Press, New York, 1987).

[111] L.P. Gor'kov, G. Grüner, "Charge Density Waves in Solids", 2000, P.188

[112] Hirsch P, Howie A, Nicholson R, Pashley DW, Whelan MJ. Electron Microscopy of Thin Crystals. R. E. Krieger Publishing Co; 1977.

[113] Cowley JM, editor. Electron Diffraction Techniques. International Union of Crystallography, Oxford University Press; 1992.

[114] Springer Science & Business Media, Transmission Electron Microscopy: A Textbook for Materials Science. (1996)

[114] Nakamoto, K. & Brown, C. W. Introductory Raman Spectroscopy. 2003.

[115] Wieboldt, D., Heintz, R., Wall, M. and Scientific, T. F. "Fundamentals of Raman Polarization Microscopy." Copyright with Thermo Scientific

[116] Zhang, J. et al. Nano Lett. 11, 2407–2414 (2011)

[117] Yuan, J. et al. Raman Spectroscopy of Two-Dimensional $Bi_2Te_xSe_{3-x}$ Platelets Produced by Solvothermal Method. Materials 8, 5007–5017 (2015).

[118] Awana, G., Sultana, R., Maheshwari, P.K. et al. Crystal Growth and Magneto-transport of Bi_2Se_3 Single Crystals. J Supercond Nov Magn 30, 853–856 (2017).

[119] Mo, S. Angle-resolved photoemission spectroscopy for the study of two-dimensional materials. Nano Convergence 4, 6 (2017). https://doi.org/10.1186/s40580-017-0100-7

[120] Capper, p. Bulk Crystal Growth: Methods and Materials, Springer Handbook of Electronic and Photonic Materials, 2017 ISBN : 978-3-319-48931-5

[121] Xia, Y. et al. Observation of a large-gap topological-insulator class with a single dirac cone on the surface. Nature Phys 5, 398–402 (2009).

[122] Kirshenbaum, K. et al. Pressure-induced unconventional superconducting phase in the topological insulator Bi_2Se_3. Physical Review Letters 111, (2013).

[123] Lawson, B. J. et al. Multiple Fermi surfaces in superconducting Nb-doped Bi2Se3. Physical Review B 94, (2016).

[124] Kamminga, M.E. *et al.* Misfit phase $(BiSe)_{1.10}NbSe_2$ as the origin of superconductivity in niobium-doped bismuth selenide. *Commun. Mater* **1,** 82 (2020).

[125] Albert, N., Phys. Rev. 162, 320 (1967)

[126] Suter, J. Phys.: Condens. Matter 10 (1998) 5977–5994

[127] Nisson, D. M. et al. Nuclear magnetic resonance as a probe of electronic states of Bi_2Se_3. Phys. Rev. B 87, 195202 (2013)

[128] NMR Studies of Phase Transitions C. ODIN Groupe Matie`re Condense´e et Mate´riaux, UMR6626 au CNRS, Universite´ Rennes I,Campus de Beaulieu. Bat11A, 35042 Rennes Cedex, France

[129] Young, B.-L. et al. Probing The Bulk Electronic States of Bi_2Se_3 Using Nuclear Magnetic Resonance. Phys. Rev. B 86, 075137 (2012)

[130] Lue, C. S. et al. Observation of a possible charge-density-wave transition in cubic $Ce_3Co_4Sn_{13}$ Phys. Rev. B 85, 205120

[131] Kuo, Y.-K., Lue, C. S., Hsu, F. H., Li, H. H. & Yang, H. D. Thermal properties of $Lu_5Ir_4Si_{10}$ near the charge-density-wave transition. Phys. Rev. B 64, 125124 (2001)

[132] Fal'ko, V.& Jungwirth T. Orbital effect of an in-plane magnetic field on quantum transport in chaotic lateral dots. Phys. Rev. B 65, 081306 (2002)

[133] Taskin, A.A. et al. Planar Hall effect from the surface of topological insulators. Nat Commun 8, 1340 (2017).

[134] Tsen, A. W. et al. Structure and control of charge density waves in two-dimensional 1T-TaS_2. Proc. Natl Acad. Sci. USA 112, 15054–15059 (2015).

[135] Berthier, C., Jérome, D., Molinié, P. J. Phys. C: Solid State Physics, 11, 797 (1978)

[136] Ohno, T., Kishimoto, Y., Miyatani, K. Physica B (Amsterdam) 230, 988 (1997)

[137] Tsuda , T., Kitaoka, Y., Yasuoka, H. Physica B+C (Amsterdam) 105, 414 (1981)

[138] Wada, S., Alloul, H., Molinié, P. J. Physique Lett. 39, 243-247 (1978) Proton spin-lattice relaxation time in the superconducting intercalation complex Tas_2 (pyridine) ½

[139] Yogi, M. , Higa, N. ,Niki, H. , Kawata, T. ,Sekine, C., J. Phys.: Conf. Ser. 683 012030 (2016)

[140] Zhang, X., Liu, W. Electron-Phonon Coupling and its implication for the superconducting topological insulators. Sci Rep 5, 8964 (2015).

[141] Smith, N. P., "Crystal Growth and Manipulation of Intercalated Chalcogenides as Superconductors and Topological Insulators" PhD Thesis, University of Wisconsin Milwaukee (2018).

[142] Chiatti, O. et al. 2D layered transport properties from topological insulator Bi_2Se_3 single crystals and micro flakes. Sci Rep 6, 27483 (2016).

[143] Martinez, G. et al. Determination of the energy band gap of Bi_2Se_3. Sci Rep 7, 6891 (2017).

[144] Kobayashi, K., Ueno, T., Fujiwara, H., Yokoya, T. & Akimitsu, J. Unusual upper critical field behavior in Nb-doped bismuth selenides. Physical Review B 95, (2017).

[145] Wang, J. et al. Investigate the Nb doping position and its relationship with bulk topological superconductivity in $Nb_xBi_2Se_3$ by X-ray photoelectron spectra. Journal of Physics and Chemistry of Solids 137, (2020).

[146] Berthier & P. Segranson, "NMR Studies of Charge Density waves in low Dimensional Conductors", P. 455. 1987, Vol.168. P455

[147] Robert M. White, Theodore H. Geballe, 1984, Long Range Order in Solids: Solid State Physics, P. 197

[148] Phillips, J.C. & Thorpe, M.F. Phase Transitions and Self-Organization in Electronic and Molecular Networks, P.415 (2001)

[149] Wu, T. et al. Incipient charge order observed by NMR in the normal state of YBa_2Cu_3Oy . Nat. Commun. 6, 6438 (2015).

[150] Kharkov, Y., Sushkov, O. The amplitudes and the structure of the charge density wave in YBCO. Sci Rep 6, 34551 (2016).

[151] Liu, Y. et al. Charging dirac states at antiphase domain boundaries in the three-dimensional topological insulator Bi_2Se_3. Physical Review Letters 110, (2013).

[152] Liu, Y. et al. Tuning dirac states by strain in the topological insulator Bi_2Se_3. Nature Physics 10, 294–299 (2014).

[153] Kuntsevich, A. Y. et al. Structural distortion behind the nematic superconductivity in $Sr_xBi_2Se_3$. New Journal of Physics 20, (2018).

[154] Zhang J L, Zhang S J, Kong P P, Zhu J, Li X D, Liu J, Cao L Z, Jin C Q Superconductivity in copper intercalated topological compound $Cu_xBi_2Te_3$ induced via high pressure Phys. C Supercond. its Appl. 493, 75–76 (2013)

[155] Wang Y L et al. 2011 Structural defects and electronic properties of the Cu-doped topological insulator Bi_2Se_3. Phys. Rev. B 84, 075335

[156] López P A, Leal F M, and Derat R E 2016 Structural and Electronic Characterization of $Cu_xBi_2Se_3$. J. Mex. Chem. Soc. 60, 101–107

[157] Matano K, Kriener M, Segawa K, Ando Y and Guo-qing Zheng 2016 Spin-rotation symmetry breaking in the superconducting state of $Cu_xBi_2Se_3$. Nature Phys. 12, 852–854

[158] Jia S, Ji H, Climent-Pascual E, Fuccillo M E, Charles M E, Xiong J, Ong N P and Cava R J. Low-carrier-concentration crystals of the topological insulator Bi_2Te_2Se. Phys. Rev. B 84, 235206 (2011)

[159] Balakrishnan G, Baumberger F, Catlow C R A, Scanlon D O and Catlow P C R A. Controlling bulk conductivity in topological insulators: Key role of anti-site defects.Adv. Mater. 24, 2154-2158 (2012)

[160] Richter W, Kokler H and Becker C R. A Raman and Far-Infrared Investigation of Phonons in the Rhombohedral compounds. Phys. Status Solidi B 84, 619–628 (1977)

[161] Nakajima S J. Phys. D: Appl. Phys. 4, 685 (1971)

[162] Lee M H, Chen C H, Tseng C M, Lue C S, Kuo Y K, Yang H D, and Chu M -W. Concomitant charge-density-wave and Unit-cell-doubling structural transitions in $Dy_5Ir_4Si_{10}$. Phys. Rev. B 89, 195142 (2014)

[163] Hovden R et al. Atomic Lattice disorder in charge-density-wave phases of exfoliated dichalcogenides (1T-TaS_2) (2016)

[164] DiSalvo F J, Wilson J A, Bagley B G, and Waszczak J V. Effects of doing on charge-density waves in layer compounds (1975)

[165] Kriener M, Seqawa K, Ren Z, Sasaki S, Wada S, Kuwabata S and Ando Y. Electrochemical synthesis and superconducting phase diagram of $Cu_xBi_2Se_3$. Phys. Rev. B 84, 054513 (2011)

[166] Vaško A, Tichý L and HorákJ J. Amphoteric nature of copper impurities in Bi_2Se_3 crystals. Appl. Phys. 5, 217–221 (1974)

[167] Tian Y, Osterhoudt G B, Jia S, Cava R J and Burch K S. Local phonon mode in thermoelectric Bi_2Te_2Se from charge neutral antisites. Appl. Phys. Lett. 108 (2016)

[168] Teyssier J, Homes C C, Akrap A and Lerch P. Optical properties of Bi_2Te_3Se at ambient and high pressure. Phys. Rev. B 86, 235207 (2012)

[170] Sokolov O B, Skipidarov S Y, Duvankov N I and Shabunina G G. Phase relations and thermoelectric properties of alloys in the Bi_2Te_3-Bi_2Se_3 system. Inorg. Mater. 43, 8–11 (2007)

[172] Yuan J, Zhao M, Yu W, Lu Y, Chen C, Xu M, Li S, Loh K and Bao Q. Raman Spectroscopy of Two-Dimensional $Bi_2Te_xSe_{3-x}$ Platelets Produced by Solvothermal Method. Materials 8, 5007–5017 (2015)

[173] Chen H et al. Phonon dynamics in $Cu_xBi_2Se_3$ (x=0, 0.1, 0.125) and Bi_2Se_2 crystals studied using femtosecond spectroscopy. Appl. Phys. Lett. 101, 121912 (2012)

[174] Kumar A, Mishra V, Warshi M K, Sati A, Sagdeo A, Kumar R, Sagdeo P R. Strain Induced Disordered Phonon Modes in Cr doped $PrFeO_3$. J. Phys. Condens. Matter 31, 275602 (2019)

[175] Johannes M D and Mazin I I. Fermi surface nesting and the origin of charge density waves in metals. Phys. Rev. B - Condens. Matter Mater. Phys. 77, 1–8 (2008)

[176] Gannon L., Ph.D thesis. Univ. Oxford, 2015.

[177] Kou C N, Shen D, Li B S, Quyen N N, Tzeng W Y, Luo C W, Wang M, Kuo Y K and Lue C S. Characterization of the charge density wave transition and observation of the amplitude mode in LaAuSb2. Phys. Rev. B 99, 235121 (2019)

[178] Chan S K and Heine V Spin density wave and soft phonon mode from nesting Fermi surfaces J. Phys. F Met.Phys. 3, 795-809 (1973)

[179] Rossnagel R K, Rotenberg E, Koh H, Smith N V and Kipp L. Fermi surface, charge-density-wave gap, and kinks in 2H-$TaSe_2$. Phys. Rev. B - Condens. Matter Mater. Phys. 72, 1–4 (2005)

[180] Whangbo M H and Canadell E. Analogies between the Concepts of Molecular Chemistry and Solid-State Physics concerning Structural Instabilities. Electronic Origin of the Structural Modulations in Layered Transition-Metal Dichalcogenides. J. Am. Chem. Soc. 114, 9587–9600 (1992)

Yanan Li

EDUCATION

University of Wisconsin-Milwaukee Milwaukee**,** WI
Ph.D. in Condensed Matter Physics Expected December 2020
Dissertation Title: Lattice and Charge Order in Bi-based Topological Insulators
Advisor: Prof. Prasenjit Guptasarma

Liaoning Normal University Liaoning, China
M.S. in Condensed Matter Physics June 2013
Research Title: Fabrication and properties' study for ZnO nanowire based MWNTs/PVDF composite thermoelectric materials

Bohai University Liaoning, China
B.S. in Education Physics June 2010

RESEARCH EXPERIENCE

University of Wisconsin-Milwaukee Milwaukee, WI
Prof. Guptasarma's lab May 2015 to present

Lattice and Charge Order in $Cu_xBi_2Te_2Se$, project

- While studying Cu intercalated Bi_2Se_3 resulting in superconductivity, became inspired to develop experiments of previously unstudied doping effects of Cu intercalation on Bi_2Te_2Se
- Proposed new innovative research based on recognition of superconductivity on Cu doped Bi_2Se_3 resulting in the creation of a new previously unstudied material
- Grew single crystals and improved the crystal growth conditions
- Independently performed 4-probe resistivity, X-ray Diffraction, Raman Spectroscopy measurements
- Participated in performing Electron Diffraction and X-ray Photoelectron Diffraction measurements with experts
- Analyzed each measurements' data using Gaussian and Lorentzian distribution and Crystal Graphical functions
- Communicated results obtained from above procedures to research advisor verbally and in email on a weekly basis
- Achieved and recognized novel Metal to Insulator Transition in Transport and Electron Diffraction
- Reviewed literature identifying the experiments' novel outcomes as a charge density wave
- Documented results and findings in published research paper
- Created first draft and co-edited final publication with advisor
- Presenting research results in Aspen 2020 winter conference

Ongoing Activities

- Collaborated with Raman Spectroscopy expert Dr. Stephen McGill from National High Magnetic Field laboratory
- Currently studying Magnetic Field of Charge Density Wave in $Cu_xBi_2Te_2Se$

Charge density Wave in Single Crystal of Bi_2Se_3, project

Completed unique tasks below in addition to similar tasks listed above

- Designed material growth conditions
- Trained junior student to grow a single Bi_2Se_3 crystal
- Reached out to and collaborated with Professor Arneil Ryes from National High Magnetic Field laboratory
- Performed Nuclear Magnetic Resonance measurements (NMR) on single crystal Bi_2Se_3 under supervision of NMR expert (Dr. Arneil Reyes)
- Participated in performing Electron Diffraction measurement
- Achieved and recognized novel Metal to Insulator Transition in Transport, Electron Diffraction and NMR measurements

Superconductivity and Charge density wave study on Nb-Bi_2Se_3, project

Completed unique tasks below in addition to similar tasks listed for first project

- Co-performed Nuclear Magnetic Resonance measurements (NMR) on single crystal $Nb_{0.05}Bi_2Se_3$ under the supervision of NMR expert
- Participated performing Electron Diffraction measurement
- Reached out and collaborated with Dr. Arneil Ryes and Dr. Ryan Baumbach from National High Magnetic Field laboratory
- Recognized co-existence of Metal to Insulator and Superconducting Transition from Transport, Electron Diffraction and Magnetization measurement
- Reviewed literature to identify novel outcome as a charge density wave and superconductivity
- Will present the research results as a talk-presentation on American Physical Society March Meeting 2020

Studying of Pb substitutional Topological Insulator $Pb_xBi_{2-x}Te_2Se$, project

Completed unique tasks below in addition to similar tasks listed for first project

- Proposed new innovative research resulting in the creation a new previously unstudied material after difficulties in reaching reach ideal Topological Insulator state, from finding research that demonstrated substituting Sn for Bi in Bi_2Te_2Se reached bulk insulation
- Performed Electron Diffraction under the subversion of Electron Diffraction expert Dr. Marvin A Schofield
- Presented the research results in my Prelim exam

National High Magnetic Field Laboratory — Tallassee, FL
Summer Research Intern — June-Aug 2019

- Performed Nuclear Magnetic Resonance measurements (including NMR field sweep with temperature, T_1 and T_2 on the directions of parallel to ab plane and perpendicular to ab plane and also angle dependent field sweep measurements) on single crystal Bi_2Se_3
- Communicated results obtained from following specific procedures to supervisor verbally and in email on a daily basis
- Created a MS Power-Point lecture summarizing project to be presented in March of 2020 at the International American Physics Society (APS) conference
- Finalizing publication for submission in 2020 tentative title: *Charge Density Wave on Single Crystal of* Bi_2Se_3

National High Magnetic Field Laboratory — Tallassee, FL
Collaboration work — March 2019

- Trained and practiced co-performing Nuclear Magnetic Resonance measurements on superconductor $Nb_{0.05}Bi_2Se_3$
- Studied novel spin-rotational symmetry broken below T_c for superconductor $Nb_{0.05}Bi_2Se_3$ by performing Angle dependent NMR Spectrum and T_1 measurements
- Communicated results on a continuous basis using obtained data to simulate different situations and provide immediate skill development feedback while learning how to perform NMR measurements
- Analyzed NMR data for T_1, Knight shift and NMR spectrum with temperature dependence
- Will perform a second measurement to further confirm this novel result

National High Magnetic Field Laboratory — Tallassee, FL
Summer Seminar Student — May 2018

- Studied advanced High Magnetic Field Measurement principles and practiced with top experts
- Making connections with research experts and other postdoctoral and doctoral students from intuitions throughout the world
- Received Certification for participation

National High Magnetic Field Laboratory — Tallassee, FL
Participated in colleague's research project — June 2017

- Participated in transport study for Cu intercalated Bi_2Se_3 superconductor under 17T magnet
- Helped make 4-probe resistivity contacts and set up measurements

Liaoning Normal University — Dalian, China
Dr. Mengke Li's Lab — August 2011-2013

Experiments

- Grew ZnO nanowire using Hydrothermal Precipitation method

- Fabricated new thermoelectric material of ZnO nanowire based multi-walled carbon nanotubes (MWNTs)/polyvinylidene fluoride (PVDF)
- Analyzed ZnO nanowire structure using Scanning Electron Microscope measurements
- Performed Seebeck coefficient measurement

Training

- Trained junior student step by step with hands-on procedures to grow ZnO nanowires
- Monitored the junior student to grow the ZnO nanowire on her own and evaluated the learning outcomes

Outcome

- Wrote M.S. thesis based on this research study

PUBLICATIONS

Publications in print:

- **Y. Li,** N. P. Smith, W. Rexhausen, M. A. Schofield and P. Guptasarma, Possible Lattice and Charge Order in $Cu_xBi_2Te_2Se$ 2020 J. Phys. Mater. 3 015008 (link: https://iopscience.iop.org/article/10.1088/2515-7639/ab5bfe) This paper was recently recommended to be included in their focus issue on topological matter by Stephan Roche, Editor-in-Chief of JPhys Materials
- **Y. Li[1],** C. A. Parsons[1], S. Ramakrishna[2], M. A. Schofield[1], A. P. Reyes[2] and P. Guptasarma[1], Charge Density Wave Order in the Topological Insulator Bi2Se3 (link: http://arxiv.org/abs/2002.12546)
- Y. Wang[1], M. Li[1], T. Zhang[2], **Y. Li[1]**, R. Yang[1], H. Fu[1], J. Sun[1], N. Xu[1], J. Wang[1], Fabrication and properties of ZnO nanowire based MWNTs/PVDF composite thermoelectric materials, Scientia Sinica Chimica, Volume 44, Issue 10: 1609-1617(2014)

Publications under progress:

- **Y. Li[1],** C. A. Parsons[1], W. Nelson[2], R. E. Baumbach[2], M. A. Schofield[1] and P. Guptasarma[1], Charge Density Wave Order in Nb intercalated Bi2Se3 Superconductor (preprint available)

Recent collaboration Proposal:

Oak Ridge National Laboratory Neutron Sciences # IPTS-25263.1
Charge density wave in $Nb_xBi_2Se_3$

CONFERENCE PRESENTATIONS

APS March Meeting Denver 2020

Talk Presentation (online available): Density Wave Order in Superconducting Nb-Bi_2Se_3
Authors: **Y. Li[1],** C. A. Parsons[1], S. Ramakrishna[2], W. Nelson[2], R. E. Baumbach[2], A. P. Reyes[2] and P. Guptasarma[1]

Aspen Winter Conference Aspen 2020

Poster Presentation: Possible Lattice and Charge Order in $Cu_xBi_2Te_2Se$
Authors: **Y. Li,** N. P. Smith, W. Rexhausen, M. A. Schofield and P. Guptasarma
Selected as supported attendee by organizer: Claudia Felser (Max Planck), Philip Moll (Ecole Polytechnique Lausanne), Brad Ramshaw (Cornell), and Adiel Stern (Weizmann Institute)

APS March Meeting Boston 2019

- Talk Presentation: Effects of Cu intercalation in Single Crystals of $Cu_xBi_2Te_2Se$
  Authors: **Y. Li,** C. A. Parsons**,** N. P. Smith and P. Guptasarma
- Co-author Talk Presentation: Structure-Property relationships and superconductivity in Single Crystals of $Nb_xBi_2Ch_3$, (*Ch* = S, Se, Te)
  Authors: C. A. Parsons, **Y. Li**, P. Guptasarma

HORNORS AND REWARDS

★Braslau Travel Grant for APS March Meeting	2020
Chancellor's Graduate Student Award	2013-2020
Graduate Student Travel Awards	2019-2020
★Lichtman Family Award for excellent research experimentalist	2019
Research Excellence Award	2016-2020
UWM Foundation's Graduate Student Fund	2014
National Scholarship for Graduate Students (China)	2012
Annual Excellence Scholarship of Bohai University	2007-2009
Chinese National Encouragement Scholarship for Excellent students (China)	2007-2008
Excellent Students of Bohai University	2007-2008

CERTIFICATIONS

National Colleges and Universities Student Language Basics Skill Competition 3rd place(China)	2008
Winner of National Grade Appraisal Hard-Pen Calligraphy Works Competition (China)	2008
National Computer Rank Examination C language level-2 certification (China)	2007
Teaching certification (China)	2010
Certificate of Completion Mag Lab User Summer School	2018

TEACHING EXPERIENCES

University of Wisconsin-Milwaukee Milwaukee, WI
Teaching Assistant (TA) Positions 2013-2020

Instructor 2016-2020
PHYSICS 121 General Physics Laboratory I (Non-Calculus Treatment)

TA

PHYSICS 107 Physics in Everyday Life	2019
PHYSICS 110 Physics for the Health Professions	2018
PHYSICS 120 General Physics I (Non-Calculus Treatment)	2013-2015
PHYSICS 209 Physics I (Calculus Treatment)	2018
PHYSICS 210 Physics II (Calculus Treatment)	2017
PHYSICS 309 Physics III: Modern Physics	2019

In courses above performed various tasks such as:

- Led multiple sections with 20 students in each section
- Reviewed the lecture contents before discussing HW/quiz problems
- Provided one to one instruction during office hours
- Created reviews to help students prepare for exams
- Used chalkboard, printed-out papers, WebAssign software and online videos to help students with concepts understanding and HW/exams related problem solving
- Assisted instructor with students' online questions and maintained course website
- Assisting the course instructor with grading for homework
- Organized online teaching for Physics 121

Private High School Educational Agency (Dalian China) Dalian, China
Teacher (part-time job) 2010-2012

- Taught physics to students preparing for college exam and application process
- Provided one to one instruction
- Guided students how to solve physics problems independently

TECHNICAL SKILLS

Nuclear Magnetic Resonance (solid state NMR) Transmission Electron Diffraction
Magnetic Properties Measurement System Raman Spectroscopy
X-ray Diffraction NMR Analysis
Rietveld refinement by General Structure Analysis System Crystal Growth
4-proble Transport Measurement/Physical Properties Measurement System
Research Design and Project Management that is timely and adheres to budget guidelines

SOFT SKILLS

Creative Thinking	Communication	Work Passion
Mentoring	Organization	Logical Reasoning
Dependability	Patience	Self-Motivation

VOLUNTEER

Shorewood elementary school 2014
Tutor for International students

Discovery World 2017
Commentator for Science behind daily used instruments

Milwaukee Art Museum 2017
Docent

The Salvation Army 2019
Kitchen helper and Christmas caroler

Compassion international 2020

Sponsoring a child from Togo